High-Dimensional Optimal Path Planning and Multi-Timescale Lagrangian Data Assimilation in Stochastic Dynamical Ocean Environments

by

Manan Doshi

B.Tech Mechanical Engineering, IIT Bombay, 2018
S.M. Computational Science and Engineering, MIT, 2021

Submitted to the Department of Mechanical Engineering
in partial fulfillment of the requirements for the degree of

DOCTOR OF PHILOSOPHY IN MECHANICAL ENGINEERING AND
COMPUTATIONAL SCIENCE AND ENGINEERING

at the

MASSACHUSETTS INSTITUTE OF TECHNOLOGY

May 2024

Authored by:	Manan Doshi Department of Mechanical Engineering April 08, 2024
Certified by:	Pierre F.J. Lermusiaux Professor, Department of Mechanical Engineering, Thesis Supervisor
Accepted by:	Nicolas Hadjiconstantinou Professor, Department of Mechanical Engineering Chairman, Department Committee on Graduate Theses
Accepted by:	Youssef Marzouk Professor, Department of Aeronautics and Astronautics Co-Director, Center for Computational Science & Engineering

High-Dimensional Optimal Path Planning and Multi-Timescale Lagrangian Data Assimilation in Stochastic Dynamical Ocean Environments

by

Manan Doshi

Submitted to the Department of Mechanical Engineering
on April 08, 2024 in partial fulfillment of the requirements for the degree of

DOCTOR OF PHILOSOPHY IN MECHANICAL ENGINEERING AND
COMPUTATIONAL SCIENCE AND ENGINEERING

ABSTRACT

In the ocean domain, opportunities for a paradigm shift in the science of autonomy involve fundamental theory, rigorous methods, and efficient computations for autonomous systems that collect information, learn, collaborate and make decisions under uncertainty, all in optimal integrated fashion and over long duration, persistently adapting to and sustainably utilizing the ocean environment. The ocean is a prime example of multiscale nonlinear multidisciplinary and strongly coupled dynamics where measurements of one variable can be used to infer other fields through their joint dynamic probability density functions. Integrating ocean dynamics with autonomy enables the principled exploration, sustainable utilization, and strong conservation of our oceans. The object of this thesis is to develop theory, algorithms, and computational systems for the high dimensional optimal path planning of autonomous vehicles in the physical space augmented with other dynamical fields, and for the Bayesian nonlinear assimilation of the observations gathered by these vehicles along their trajectory. The resulting high dimensional optimal path planning and generalized Lagrangian Bayesian data assimilation enable the sustained and optimal operation of autonomous vehicles over a long time duration in realistic uncertain ocean settings. With this vision, the vehicles autonomously make decisions to optimally achieve their mission targets in the augmented space of physical and collectible fields, e.g., reach the destination in minimum time while using the minimum energy, harvest the maximum wave-solar-wind energy, or farm the maximum amount of kelp. To this end, we focus on three specific theoretical and methodological goals: (i) Develop exact differential equations and accurate algorithms to efficiently predict and compute the reachable sets and optimal controls for complex high-dimensional objectives in dynamical fields and showcase these controls in realistic ocean scenarios; (ii) Develop Bayesian theory and schemes to predict Lagrangian field probability densities and rigorously assimilate Lagrangian data collected by moving vehicles or drifters, leveraging the different sensitivity and timescales of the underlying Lagrangian and Eulerian systems; and (iii) Integrate the optimal planning and assimilation to enable learning from the information gathered on-board the vehicles, from Bayesian updates of the optimal controls to the acquisition of knowledge using Bayesian learning. We showcase the theory and methods in a range of ocean applications.

In the first part, we review the theory and schemes to predict joint energy-time, harvesting-time, and energy-harvesting-time reachability fronts and optimal paths using state augmentation. We validate our energy-time algorithms in analytical and representative dynamical fields. We then derive theory to predict reachability fronts across multiple times simultaneously and obtain a closed loop control law allowing vehicles to accomplish their mission even after straying from their initial plan due to forecast errors. The theory and schemes are developed for both backward and forward reachable tubes with time-varying target and start sets. The resulting value functions elegantly capture not only the reachable tubes but also time-to-reach and time-to-leave maps as well as start time versus duration maps. We validate results with analytical solutions and demonstrate wider applications for optimal control in dynamic environments.

In the second part, we develop and implement fundamental schemes for multi-timescale Bayesian data assimilation for coupled dynamical systems, with a focus on Lagrangian-Eulerian systems. We obtain a Gaussian Mixture Model (GMM) - Dynamically Orthogonal (DO) based hybrid filter for Lagrangian and Eulerian stochastic fields and observations. We first showcase the schemes for a coupled system where we analytically validate the performance of the filter. We subsequently demonstrate results by applying the filter for a general coupled chaotic system and for a joint Lagrangian-Eulerian system with a more complex quasi-geostrophic flow.

In the third part, we integrate the schemes developed for the first two parts. We propose coupled methods that allow ocean vehicles to robustly and optimally complete their mission while continuously learning from the new information being collected, updating the Lagrangian and Eulerian fields, their joint probabilities, and the robust optimal control of their future trajectories. We showcase preliminary results using the proposed method.

We conclude by demonstrating several planning and Lagrangian algorithms in data-assimilative ocean simulations and real-time ocean experiments with real data and forecasts. This includes the characterization of residence times and connectivity in the Red Sea, the transport of plastics in the coastal ocean showcasing results for Massachusetts Bay, the subduction pathways of surface waters to intermediate depths in the Alboran Sea, and the Bayesian Eulerian-Lagrangian data assimilation of drifter data in the Balearic Sea.

Thesis supervisor: Pierre F.J. Lermusiaux
Title: Professor, Department of Mechanical Engineering

Acknowledgments

This thesis would not have been possible without the support of all the extraordinary people around me who have helped me along the journey of my PhD.

I thank my thesis advisor, Prof. Pierre Lermusiaux, who has been an extraordinary mentor and has helped shape me both as a researcher and a person. The amount of hard work Pierre puts in for MSEAS is extremely inspiring. His guidance has helped me for everything from becoming a better researcher, writer and presenter.

I would also like to thank my committee – Prof. John Leonard, Prof. Youssef Marzouk, and Prof Claire Tomlin – for the invaluable feedback during the committee meetings. Your input has helped shape this thesis. I admire all of your work immensely and it was a privilege to have guidance from you. Grateful for your support and belief in my work.

I owe many thanks to the administrative staff: Lisa, Kate, Saana, Una and Leslie for being so helpful for supportive.

I am also very grateful to collaborators I have worked with. Manmeet, this is our joint work. I wouldn't be working on this topic if it were not for you. Last part of PhD was the most difficult for me because working with you made things so easy. Nothing will ever beat the high of figuring out the energy optimal equation after hours of brainstorming together. Marius, working with you has been an amazing learning experience. Brainstorming sessions were extremely satisfying and I am always amazed by how proactive you are with various projects and how you take initiative to move them forward.

I am also extremely thankful to all of MSEAS. Pat and Chris – you are the engine of this lab. Thank you for your help with a million things. Real-time sea experiments was a difficult but immensely rewarding experience because I got to work with you and got to observe and learn from the pros in action. Akis and Manmeet, your friendship means a lot to me. I couldn't have made it this far without all of our late nights working together and all the emotional support meetings. Akis, learning how to sail from you has been the highlight of my life at MIT! Chinmay – Your guidance through the years was invaluable. I have had nobody to discuss cricket with since you left! Abhinav – You have been an amazing friend and mentor. You have always been available to help no matter what and I appreciate that a lot. Wael – You are an amazing person and a mentor – not just to me but to everybody around you. TAing with you has been an awesome experience (and super easy – you did everything!). When the going gets tough, you have always helped calm me down. Corbin, Aaron and Tony – Your presence made 5-428 an entertaining place! Time disappeared whenever we started discussing anything from coding languages to politics. I would also like to thank the new guard of MSEAS. Aditya, Ellen, Anantha – Solving crosswords with you guys kept me sane as I finished my thesis! Thanks for introducing me to FPL so I could beat

you guys in my first attempt! Alonso, thanks for being a great friend! Ruizhe, Sanaa, Clara, Mike, Jacob, Zach, Aditya Ghodgaonkar, Marcoul, Bastien, Ben Koenig, Yoland – It's been great working with you.

To my friends in insti – Aakriti, Damani, Keni, Sanat, Vete, Yashaswini – you guys are my second family and have made me what I am today. Guru, Khujao – You guys know me better than myself. I was right to be scared during graduation – life has been hard without having you guys in the same room/next door to me. Conversations with you guys are still the highlight of my day.

Finally, I would like to thank my family who have moulded me into who I am. Mom, Dad, Bhai, Bhabi, Rian, my grandparents, my cousins – Being away from all of you for so long has been very difficult. Your constant belief, love, support has kept me afloat. Vishwa – I don't think words can do justice to how much gratitude I have for your presence in my life. Together we are one functional human!

Setu, we always *got* each other. I miss you – you'd have liked this sort of thing.

Contents

---

[1]This chapter is based on [41].
[2]This chapter is based on [39].

---

[3]This chapter is based on [38].

---

[4]This section is based on [40].

[5]This section is based on [125].

[6]This section is based on [147].

List of Figures

4.1   Schematics illustrating various steps of the algorithm. (a) A Gaussian mixture model (GMM) is fitted to joint ensembles of the Eulerian and Lagrangian system. Note that there are multiple Lagrangian ensemble members for every given Eulerian ensemble member. As a result, the joint ensemble members, represented by the black dots in the background, occur in vertical lines. The fitted GMM consists of three mixture components whose mean and standard deviations are represented by the ellipses and whose weights are represented by the transparency of the ellipses. The contour plot in the background represents the total value of the probability density function (pdf). The black line plots at the edges of the plot correspond to the marginal distributions with contributions from each of the specific mixtures given by the corresponding color-coded line plots. The vertical brown lines correspond to arbitrarily chosen Eulerian ensembles of interest that we will use to illustrate the next steps of the algorithm. The horizontal pink line corresponds to the Lagrangian observation that will be assimilated at this step. (b) The posterior GMM computed using the Bayes' law with prior GMM, the observation model, and the Lagrangian observation. The various components of the plot are identical to the plot for the Prior GMM. We see that the probability mass further away from the observation 'line' significantly drops, as expected. (c) We then plot the prior and posterior marginals (the black line plots at the top of the previous two plots) together and update the weights of the Eulerian ensemble members we were observing using the ratio of these marginal values. The thickness of the brown lines corresponding to these Eulerian ensemble members reflect their new weight. The ensemble member $x_{\mathcal{E}} = -1.0$ has a higher posterior value than prior value and as a result has a higher weight. Conversely, $x_{\mathcal{E}} = 1.0$ has a lower weight. We not that we do not resample the Eulerian values and just reweight them in a way that the weighted ensemble members correspond to samples from the posterior marginal. (d) Here, the prior and posterior conditionals pdfs of the Lagrangian ensemble members corresponding to each of the three Eulerian ensemble members are plotted.

List of Tables

Chapter 1

Introduction

The growth of autonomous vehicles has been staggering in the last few decades. Self driving cars on land, autonomous gliders in the air and remotely operated underwater vehicles in the ocean have all seen a surge of interest in the engineering and research community in the past years [6, 55, 61, 122, 185].

Central to the effective operation of all autonomous vehicles is efficient and accurate motion control which falls under the purview of path planning[111]. Path planning, in the most general sense, corresponds to a set of rules to be provided to an autonomous robot for navigating from one configuration to another in some optimal fashion [134]. The metric for optimality, moreover, is problem dependent and depends on the user specified objective of interest. With the rise in the capabilities of these autonomous vehicles, the complexities on their mission also increases. There is thus a need of methods that can plan paths for these vehicles in a way that meets these complex optimality criteria.

As humans, we often combine what we learn over time, and then make informed decisions and complete desired and new tasks. Since these autonomous vehicles need to operate with little or no human input, they require intelligent predictive capabilities so as to forecast their best courses of action, optimally sense their surroundings and adapt to the new information collected. The learning over time, or backward and forward inference, is critical for long-term

autonomy, especially in complex nonlinear settings that are ubiquitous in the ocean domain.

The problem of robust, optimal path planning algorithms can be broken down into two parts: (a) Finding optimal control for complex objectives in dynamic, stochastic environments, and (b) Learning from the measurements to update the optimal control strategy and the ocean model.

In the first part of the thesis, we will focus on the first objective. In chapter 2 we summarize our collaborative contributions published in [37, 41], where we present a high-dimensional Hamilton-Jacobi reachability approach for optimal path planning with complex in stochastic environments and demonstrate the validity of this method in controlled settings where an analytical optimal solution is available. We also demonstrate the scalability of these methods by computing these optimal paths with realistic ocean forecasts. In chapter 3, we present our contributions published in [39]. With our collaborators, we obtained and applied new governing equations for reachability analysis over multiple start and terminal times all at once, and for systems operating in time-varying environments with dynamic obstacles and any other relevant dynamic fields.

While the first part of the thesis focuses on path planning in a deterministic setting, the next part of the thesis focuses on the learning in a stochastic environment. Accurately predicting complex and planetary scale dynamical systems requires the integration of numerical models with observed data through Data Assimilation (DA) methods. Our focus within this domain is on Lagrangian Data Assimilation (LaDA), a critical area given the increasing reliance on Lagrangian instruments like floats and drifters in oceanographic research. Chapter 4 introduces a novel multi-timescale filtering algorithm for assimilating data from these instruments, which traverse the ocean currents and provide valuable data from a highly chaotic system. The proposed filter takes into account the challenges posed by (i) the highly nonlinear nature of Lagrangian dynamics, which contrasts with the relatively stable (but still chaotic) Eulerian state variables, and (ii) the computationally expensive high dimensional stochastic Eulerian dynamical system, which contrasts the relatively cheap computational

cost of the stochastic Lagrangian system. The proposed multi-timescale filter is derived for general coupled systems with a special focus on the Eulerian-Lagrangian system.

In the third part, in chapter 5, we integrate the schemes developed for the first two objectives and propose coupled methods that allow ocean vehicles to robustly and optimally complete their mission while continuously learning from the new information being collected, updating the Lagrangian and Eulerian fields, their joint probabilities, and the robust optimal control of their future trajectories.

Finally, in chapter 6, we demonstrate the novel utilization of several of our planning and Lagrangian algorithms in data-assimilative ocean simulations and real-time ocean experiments with real data and forecasts issued by our MIT MSEAS group. These results were obtained using inputs from varied members of the MSEAS group, several of whom wrote significant portions of this chapter.

Chapter 7 summarizes the main conclusions of these thesis and proposed various future research direction.

Chapter 2

Energy-Time Optimal Path Planning in Dynamic Flows[1]

The contributions summarized in this chapter on joint energy-time optimal path planning were completed as part of the SM thesis of Doshi [37] and were further elaborated upon in [41]. We refer the reader to these references for more comprehensive descriptions and examples.

2.1 Introduction

The rapid expansion of autonomous vehicles such as self-driving cars, drones, and underwater vehicles has marked a significant advancement in the last decade, driven by the crucial role of efficient and accurate motion control within the realm of path planning [6, 55]. Path planning involves the development of optimal navigational strategies for these vehicles to move from one point to another, considering factors like travel time, energy consumption, safety, and data quality [134, 190]. The push for these vehicles to operate autonomously in challenging conditions over longer durations has particularly emphasized the need for energy optimization.

---

[1]This chapter is based on [41].

Given the dynamic nature of environments such as the ocean, where currents and waves significantly influence navigational paths, it's essential to incorporate the effects of such external flow fields into path planning [176, 184]. This paper addresses the complexities involved in predicting these flows and their impacts on vehicle paths, presenting fundamental differential equations that govern the joint optimization of energy and time in dynamic flows, and proposing effective numerical solutions for these equations, thereby offering a methodology for predicting optimal paths based on multi-objective optimization [132].

2.2   Problem Statement

Energy-time optimal path planning presents a multi-objective optimization challenge, aiming to minimize both travel time and energy consumption, which are typically conflicting objectives. This problem falls under the realm of non-trivial multi-objective optimization, where no single solution can optimally satisfy all objectives, leading to a set of Pareto optimal solutions. Each Pareto optimal solution is such that no objective can be improved without compromising another, forming a Pareto front. This research focuses on deriving the entire Pareto front using exact differential equations, taking into account the vehicle's dynamics, including its position and energy state over time, under the influence of a known deterministic background flow.

The vehicle's motion is modeled as a point particle, with its dynamics dictated by both its thrust and the advection from the background flow, governed by ordinary differential equations (ODEs). The energy consumption, primarily for thrust, is considered to vary with the vehicle's speed, encapsulated in a power function, which, for the sake of simplicity, is assumed here to follow a quadratic drag model. The optimization problem seeks to identify Pareto optimal solutions that minimize the final time and maximize the remaining energy, subject to the vehicle's initial conditions, its dynamics, and the energy constraints outlined by the first law of thermodynamics.

The notation for the problem parameters are given in Table 2.1.

$\boldsymbol{x}, e, t$	Physical-space, energy & time coordinates	$\boldsymbol{X_p}(t)$	Vehicle position at time t
$\boldsymbol{x}_s$	Start point	$E_p(t)$	Vehicle energy at time t
$\boldsymbol{x}_f$	Target point	$F(t)$	Vehicle nominal speed at time t
e_s	Initial vehicle energy at start point	F_{max}	Maximum vehicle nominal speed
e_f	Final vehicle energy at target point	$\hat{\boldsymbol{h}}(t)$	Vehicle heading at time t
t_s	Start time	$\boldsymbol{V}(\boldsymbol{x}, t)$	Spatio-temporal velocity field
t_f	Final time	$\dot{W}(F)$	Energy loss rate as a function of
k, n	Parameters of the power-energy law		vehicle speed

Table 2.1: Summary of main problem parameters.

The dynamics of the system are given by equation 2.1.

$$\frac{\mathrm{d}\boldsymbol{X_p}}{\mathrm{d}t} = \boldsymbol{V}\left(\boldsymbol{X_p}(t), t\right) + F(t)\,\hat{\boldsymbol{h}}(t), \tag{2.1a}$$

$$\frac{\mathrm{d}E_p}{\mathrm{d}t} = -\,\dot{W}(F(t)). \tag{2.1b}$$

The constraints of the problem are given by equations 2.2 and the problem statement is given by equations 2.3.

$$\boldsymbol{X_p}(0) = \boldsymbol{x}_s \tag{2.2a}$$

$$E_p(0) = e_s \tag{2.2b}$$

$$\boldsymbol{X_p}(t_f) = \boldsymbol{x}_f \tag{2.2c}$$

$$E_p(t) > 0 \ \ \forall t \in [t_s, t_f]. \tag{2.2d}$$

$$\begin{aligned} \underset{F(t),\ \hat{\boldsymbol{h}}(t)}{\text{minimize}} \quad & [t_f, -e_f] \\ \text{subject to} \quad & \text{Eqs. (2.2a-d)} \\ & \text{Eqs. (2.1a-b)} \end{aligned} \tag{2.3}$$

2.3 Theory

The core of time optimal path planning revolves around the concept of a vehicle's *reachable set*, $\mathcal{R}(\boldsymbol{x}_s, t)$, which encompasses all potential states accessible from an initial state $\boldsymbol{x}_s$ through valid control sequences, with the *reachability front* $\partial\mathcal{R}(\boldsymbol{x}_s, t)$ marking the spatial extremities achievable at any given time [7]. The level set method, particularly as detailed in works by Lolla et al. [133, 134], is pivotal in computing and evolving this front, representing it as the zero level surface of an implicit function $\phi(\boldsymbol{x}, t)$, thereby allowing the determination of time optimal paths by tracking the front's progression to the target and retracing the optimal trajectory.

The derivation of the differential equations governing the evolution of the reachability front in the energy-time space begins with the vehicle's dynamics in both physical and energy spaces, leading to the definition of an augmented state space $\Omega^a \subseteq \mathbb{R}^{d+1}$, which includes both spatial and energy states of the vehicle. Through a specified control policy, involving heading and speed functions, the vehicle's trajectory within this augmented space is determined by an Ordinary Differential Equation (ODE) system.

$$\frac{\mathrm{d}\boldsymbol{X}_{\boldsymbol{p}}^a(t)}{\mathrm{d}t} = \boldsymbol{U}^a(\boldsymbol{X}_{\boldsymbol{p}}^a(t), t) + \boldsymbol{V}^a\left(\boldsymbol{X}_{\boldsymbol{p}}^a(t), t\right), \tag{2.4}$$

where

$$\boldsymbol{X}_{\boldsymbol{p}}^a = \begin{bmatrix} \boldsymbol{X}_{\boldsymbol{p}} \\ E_p \end{bmatrix}, \tag{2.5a}$$

$$\boldsymbol{U}^a(\boldsymbol{X}_{\boldsymbol{p}}^a(t), t) = \begin{bmatrix} F(\boldsymbol{X}_{\boldsymbol{p}}^a, t)\,\hat{\boldsymbol{h}}(\boldsymbol{X}_{\boldsymbol{p}}^a, t) \\ -\dot{W}(F(\boldsymbol{X}_{\boldsymbol{p}}^a, t)) \end{bmatrix}, \tag{2.5b}$$

$$\boldsymbol{V}^a\left(\boldsymbol{X}_{\boldsymbol{p}}^a(t), t\right) = \begin{bmatrix} \boldsymbol{V}\left(\boldsymbol{X}_{\boldsymbol{p}}, t\right) \\ 0 \end{bmatrix}. \tag{2.5c}$$

The primary objective is to establish a Partial Differential Equation (PDE) that governs the evolution of the augmented reachable set and its boundary, the reachability front, within Ω^a. This PDE characterizes the ensemble of points in the augmented space that are accessible from the initial position and energy state at any given time, thus framing the foundation for analyzing vehicle dynamics in a comprehensive energy-time framework. This PDE for evolving the implicit function (and thus the reachability front) is given in equation 2.6. The schematic in Figure 2.1 illustrates this reachability front in the augmented space. Readers are referred to [41] for details on derivation of the below equation

$$\frac{\partial \phi(\boldsymbol{x^a}, t)}{\partial t} + \max_{\hat{\boldsymbol{h}}, F} \underbrace{\left\{ \boldsymbol{U^a}(\boldsymbol{x^a}, t) \cdot \frac{\partial \phi}{\partial \boldsymbol{x^a}} \right\}}_{\text{Maximization term}} + \boldsymbol{V^a}(\boldsymbol{x^a}, t) \cdot \frac{\partial \phi}{\partial \boldsymbol{x^a}} = 0$$

$$\implies \frac{\partial \phi(\boldsymbol{x^a}, t)}{\partial t} + \max_{\hat{\boldsymbol{h}}, F} \left\{ F \, \hat{\boldsymbol{h}}^T \cdot \frac{\partial \phi}{\partial \boldsymbol{x}} - \dot{W}(F) \cdot \frac{\partial \phi}{\partial e} \right\} + \boldsymbol{V} \cdot \frac{\partial \phi}{\partial \boldsymbol{x}} = 0 \tag{2.6}$$

$$\phi(\boldsymbol{x^a}, t = 0) = \phi_0(\boldsymbol{x^a})$$

While this equation holds for a general energy use function $\dot{W}(F)$, we are also specifically interested in the case where the energy use follows a power law $\dot{W}(F) = k \cdot F^n$. Here, k and n are constants and we assume $n \geq 2$. For such a power law, we obtain the optimal vehicle speed to be

$$F^*(\boldsymbol{x}, e, t) = \begin{cases} F_{max} & \text{if } \frac{\partial \phi}{\partial e} \leq 0 \\ \min \left(F_{max}, \left(\frac{\left\| \frac{\partial \phi}{\partial \boldsymbol{x}} \right\|}{k \cdot n \frac{\partial \phi}{\partial e}} \right)^{\frac{1}{n-1}} \right) & \text{if } \frac{\partial \phi}{\partial e} > 0 \, . \end{cases} \tag{2.7}$$
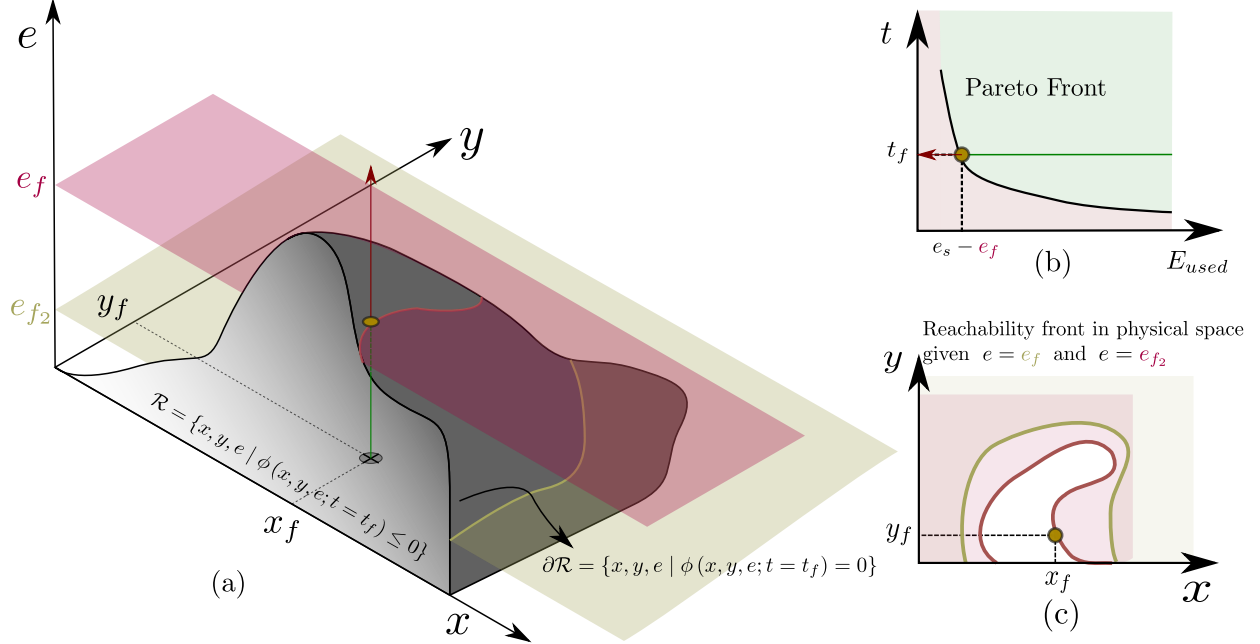
Figure 2.1: Augmented reachability front and Pareto front schematics. (a) Evolution of the reachability front in the augmented state space. (b) Pareto front which can be computed by tracking the intersection of the level set with the energy line at the destination. (c) Contours of the reachability front at different energy levels projected onto the physical space. For these schematics, we assumed a three-dimensional (3D) augmented space thus a two-dimensional (2D) physical space.

and the corresponding law for evolving the reachability front is given by

$$\frac{\partial \phi(\boldsymbol{x^a}, t)}{\partial t} + F^*(\boldsymbol{x}, e, t) \left\| \frac{\partial \phi}{\partial \boldsymbol{x}} \right\| + \boldsymbol{V}(\boldsymbol{x}, t)^T \cdot \frac{\partial \phi}{\partial \boldsymbol{x}} + \left[- k \cdot [F^*(\boldsymbol{x}, e, t)]^n \right] \cdot \frac{\partial \phi}{\partial e} = 0,$$

$$\phi(\boldsymbol{x^a}, t = 0) = \phi_0(\boldsymbol{x^a}) .$$

(2.8)

2.4 Applications

We demonstrate our proposed method by applying it to various testcases in the aforementioned published research[37, 41].

Here, we briefly describe the application of our approach on a complex, time-dependent simulated double-gyre ocean flow field (often used to model near-surface ocean circulation

28

in mid-latitude regions, such as an idealized version of the Gulf Stream). Governed by non-dimensional Partial Differential Equations (PDEs) reflecting fluid dynamics, including Coriolis effects, wind stress, and Reynolds number considerations, the model is solved numerically using a modular finite volume framework. A specific scenario is investigated where a vehicle navigates from the northwest to the southeast of the domain, contending with dynamic flow fields and energy constraints. The testcase highlights the significant impact of the gyre-induced flow field on the propagation of the vehicle's reachability front, particularly evident in the circular advection patterns observed in the early time frames. The testcase underscores the relationship between ocean dynamics and the optimal path, emphasizing the gyre's role in influencing the vehicle's trajectory and energy consumption. Figure 2.2 plots snapshots of the background flow. Figure 2.3 demonstrates the evolution of the reachability
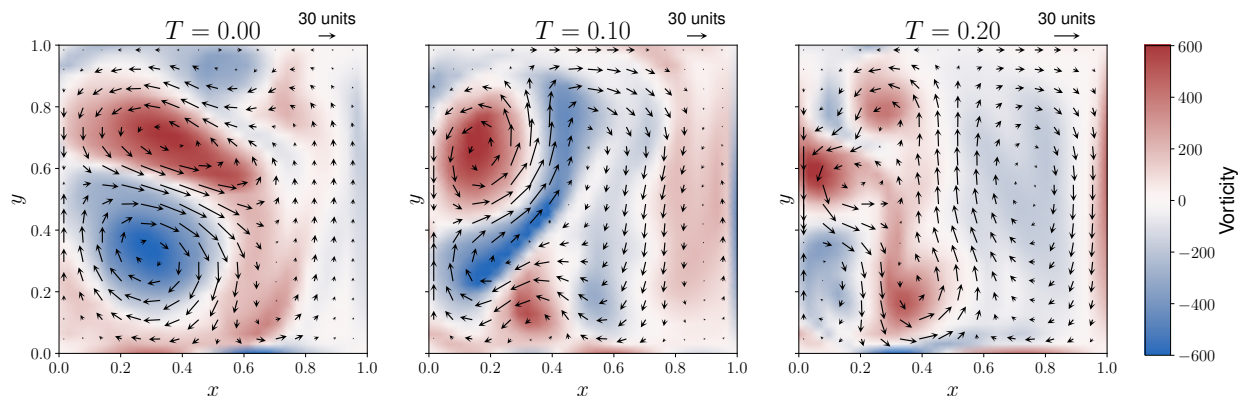
Figure 2.2: Snapshots of the quasi-geostrophic double gyre flow field at three non-dimensional times, with non-dimensional flow currents reaching 50 units. The fields of ocean currents are represented by velocity vectors, with the non-dimensional vorticity field colored in the background.

front with different colors corresponding to different energy levels. Figure 2.4 plots out the optimal path for various energy constraints and the pareto curve corresponding to the case

2.5 Conclusion

This work introduces a new theoretical foundation and computational schemes for the joint optimization of energy and time in the path planning of autonomous vehicles navigating through strong and dynamic flow fields. By augmenting physical space with an energy dimension and integrating exact Partial Differential Equations (PDEs), the study establishes a methodology for determining the energy-time Pareto front, from which optimal paths and controls can be derived without resorting to heuristics. The approach utilizes the level set method for forward reachability analysis and implicit schemes for backward trajectory computation, ensuring computational efficiency and accuracy. The methodology's applicability is demonstrated through a numerical example in a double-gyre flow representative of mid-latitude ocean circulations. The results highlight the method's precision and efficiency in capturing the optimal solutions influenced by dynamic flow conditions. Future extensions include applications to time-varying objectives, motion constraints, uncertain flow fields, and real-time adaptive path planning, underscoring the method's broad potential for diverse environmental and operational scenarios.
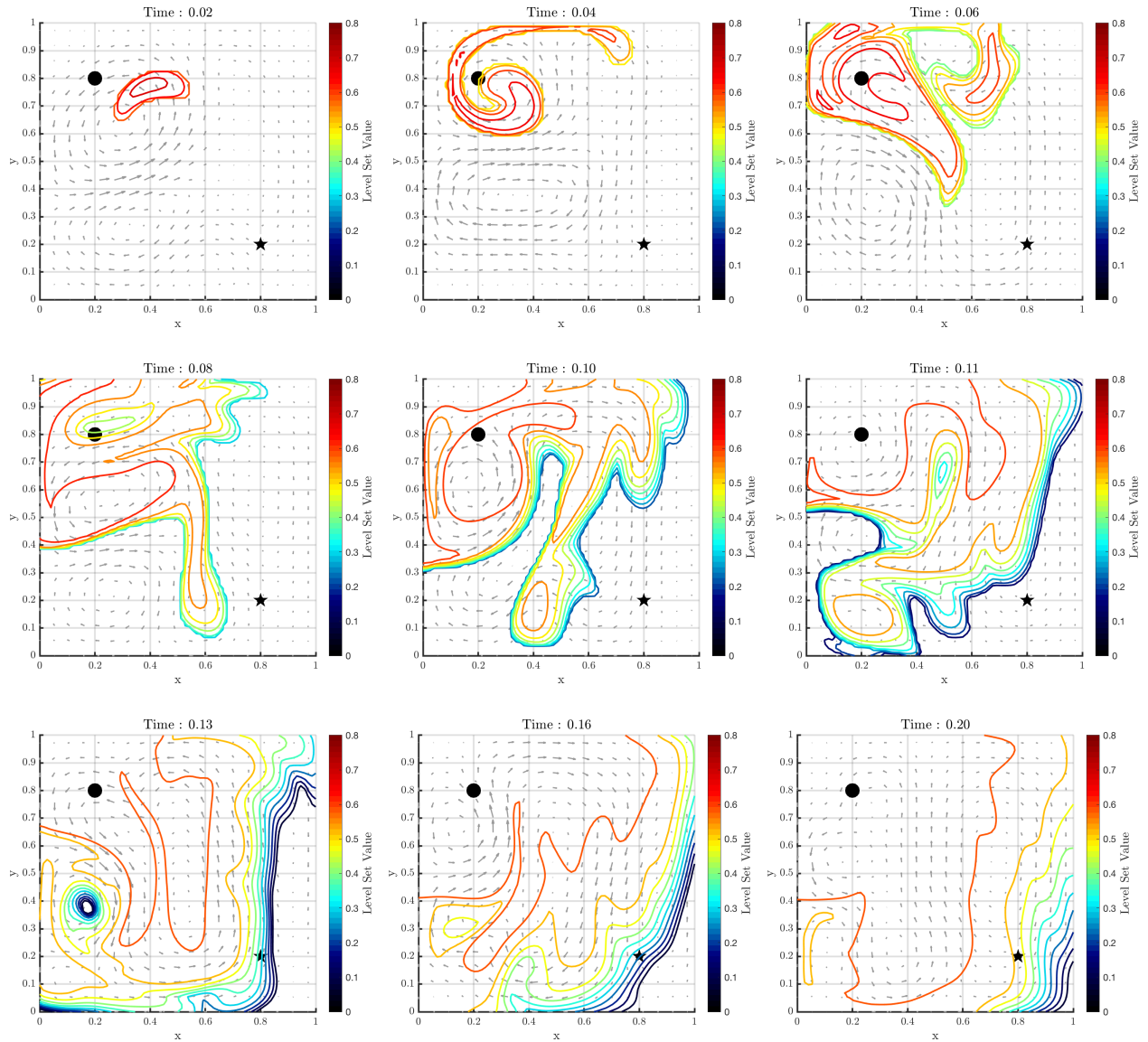
Figure 2.3: Dynamic quasi-geostrophic double gyre flow: Forward solve. Snapshots of the evolution of the augmented reachability front. Plotted are the contours of the front at different energy levels projected onto the physical domain and overlaid on the dynamic field of simulated ocean velocity vectors. The reachability front is here a surface in a 3D space (x, y, e), and the contours plotted are slices of this front at different energy values (as schematized in Figure 2.1(c)). The start time for the vehicle is $T = 0$, with the start point (circle) and target endpoint (star) as shown.
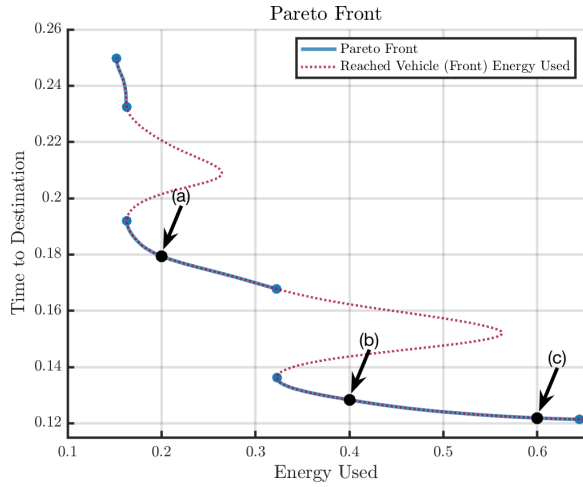
(a) Pareto front for the multi-objective path planning. Three Pareto optimal solutions are marked. Their optimal speed functions and paths are shown in the other Panels.
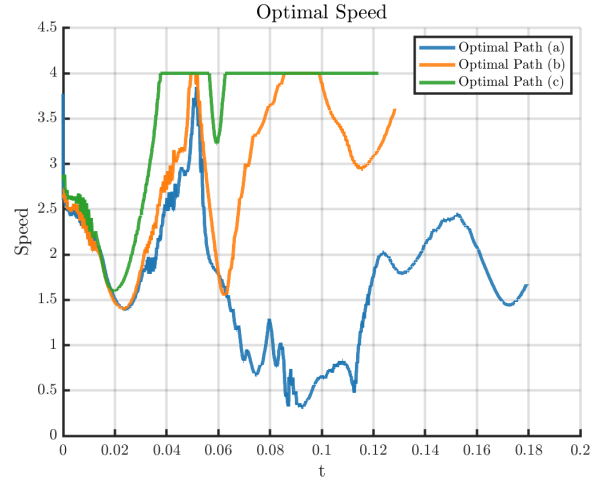
(b) Optimal speed functions for the three marked Pareto optimal solutions.
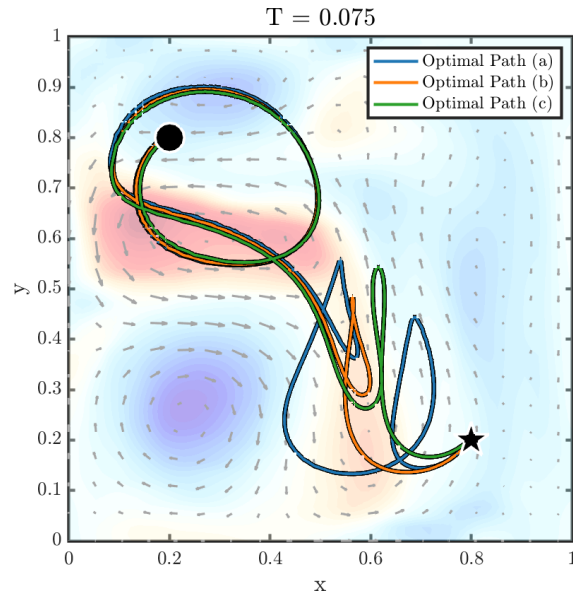
(c) Optimal paths for the three marked Pareto optimal solutions.

Figure 2.4: Dynamic quasi-geostrophic double gyre flow: Final Pareto optimal solutions to the energy-time optimal path planning.

Chapter 3

Hamilton-Jacobi Multi-Time Reachability[1]

For the analysis of dynamical systems, it is fundamental to determine all states that can be reached at any given time. This chapter is concerned with this question and results have been published in [39]. Specifically, we obtain and apply new governing equations for reachability analysis over multiple start and terminal times all at once, and for systems operating in time-varying environments with dynamic obstacles and any other relevant dynamic fields. The theory and schemes are developed for both backward and forward reachable tubes with time-varying target and start sets. The resulting value functions elegantly capture not only the reachable tubes but also time-to-reach and time-to-leave maps as well as start time vs. duration plots and other useful secondary quantities for optimal control. We discuss the numerical schemes and computational efficiency. We first verify our results in an environment with a moving target and obstacle where reachability tubes can be analytically computed. We then consider the Dubin's car problem extended with a moving target and obstacle. Finally, we showcase our multi-time reachability in a non-hydrostatic bottom gravity current system. Results highlight the novel capabilities of exact multi-time reachability in dynamic

---

[1]This chapter is based on [39].

environments.

3.1   Introduction

Reachability analysis quantifies the states that can be reached by an actuated dynamical system. With optimal control, Hamilton-Jacobi (HJ) reachability analysis formalized this concept with differential equations, leading to recent successes [7, 23]. Classical HJ reachability is mainly concerned with the computation of reachable sets, forward and backward in time, often for robotics and autonomy applications. It provides analyses of the performance and safety of dynamical systems [7], including formal safety guarantees by determining regions of a system's state space that results in catastrophic failure (ex. hitting an obstacle) [22]. With some modifications, it handles moving obstacles and targets in both steady and time-varying systems [16, 17, 54, 103]. HJ reachability is a versatile method for path planning, even in complex environments such as strong and dynamic ocean currents [133, 134, 136]. It then provides the exact solution and is more efficient than other schemes, e.g., graph methods [144]. Reachability planning has been extended to uncertain environments [191] and risk optimality [192]. Finally, HJ reachability has been used in aircraft auto-landing, model predictive control (MPC) of unmanned aerial vehicles (UAVs) and underwater vehicles (AUVs), and multiplayer reach-avoid games [5, 7, 8, 35, 78, 193].

In this paper, the aim is to drastically extend reachability analysis. Some of the key questions that motivate our work include: i) How can we extend classical reachability theory to multiple start and terminal times?; ii) What is the corresponding value function that provides all level sets at once and what is its governing HJ reachability equation?; iii) Could we compute reachable tubes for all possible times without having to resort to repeated solves of classic reachability PDEs?; iv) What are other quantities that such multi-time forward and backward analysis could compute?; and v) What are the corresponding computational costs?

To address the above questions, we derive a new approach for analyzing the reachability of time-varying dynamical systems that we refer to as *multi-time reachability*. We formulate the optimal control problem using a new running cost term, and obtain new governing equations for reachability analysis over multiple start and terminal times all at once, and for systems operating in time-varying environments with dynamic obstacles and any other dynamic fields relevant to their control. Unlike the prior results on moving targets and obstacles, we present a theory that incorporates these effects in the system dynamics without introducing extra dimensions [103] and fields [54]. We apply our results to three applications and demonstrate that the new governing equations not only more efficiently compute backward and forward reachable tubes, but also generate new secondary quantities that encode valuable reachability information such as duration maps.

In what follows, Section 3.2 outlines the problem statement and introduce key notation. Section 3.3 develops the theory and equations for multi-time reachability. Numerical methods are briefly discussed in 3.4. In Section 3.5, applications and numerical results for new multi-reachability problems are presented, followed by the conclusions in Section 3.6.

3.2   Problem Formulation

Our primary goal is to accurately and efficiently compute reachable tubes for general time-varying dynamical systems. There are essentially two main cases. In the first, we consider a time-varying target set and predict what is known as the backward reachable tube. In the second, we consider a time-varying start set and compute the forward reachable tube. For each case, we derive the governing equations and also solve the added complexity of time-varying obstacles that must be avoided in the dynamic environment.

Next, we formalize the above concepts. We define the properties of the dynamical systems. We then describe the start, target, and obstacle sets, as well as the backward and forward reachable tubes. Finally, we combine all these components and define the types of

problems we solve.

3.2.1 System Dynamics

In this work, we consider dynamical systems defined by an ordinary differential equation (ODE) of the form

$$\dot{\boldsymbol{\xi}}(s) = \boldsymbol{f}(\boldsymbol{\xi}(s), \boldsymbol{u}(s), s), \quad s \in [0, T], \tag{3.1}$$

with given initial or terminal conditions, where $\boldsymbol{\xi} \in \mathbb{R}^{n_x}$ is the system state governed by the ODE, s the temporal variable in an interval $[0, T]$, and $\boldsymbol{u}(\cdot)$ the control from a set $\mathbb{U}$ of measurable functions of $s \in [0, T]$ with values in $\mathcal{U}$:

$$\mathbb{U} = \{\boldsymbol{\phi} : [0, T] \to \mathcal{U} \mid \boldsymbol{\phi}(\cdot) \text{ is measurable}\}. \tag{3.2}$$

The dynamical systems (3.1) govern state variables explicitly affected by the controls (e.g. autonomy variables) but the dynamics $\boldsymbol{f}$ in general includes all other relevant forcing such as the dynamic environment with dynamic obstacles and other dynamic fields that affect the autonomy, e.g. [14, 122]. The control space $\mathcal{U}$ is often a closed bounded set in $\mathbb{R}^{n_u}$, where n_u is the number of control inputs. The system dynamics $\boldsymbol{f} : \mathbb{R}^{n_x} \times \mathcal{U} \times \mathbb{R} \to \mathbb{R}^{n_x}$ are further assumed to be continuous, bounded and Lipschitz continuous in $\boldsymbol{\xi}$ uniformly in $\boldsymbol{u}$ [7]. Then, there exists a unique solution to Equation (3.1) for any control sequence $\boldsymbol{u}(\cdot)$ [7, 104]. For the initial value problem, this solution is the trajectory of the system from an initial state $\boldsymbol{x}$ at time $t \in [0, T]$ forced by the control sequence $\boldsymbol{u}(\cdot)$ and denoted here by $\boldsymbol{\xi}_{t,\boldsymbol{x}}^{\boldsymbol{u}(\cdot)}(s)$.

3.2.2 Start, Target, and Obstacle Sets

We focus on systems either launched from some dynamic start set or being required to reach a dynamic target set, with the constraint of avoiding the dynamic obstacle set, i.e. any dynamic disjoint obstacles that may be present. We now formalize some of the properties of these sets.

For each $t \in [0, T]$, we denote the time-varying start, target, and obstacle sets as $\mathcal{S}_t$, $\mathcal{T}_t$ and $\mathcal{O}_t$ respectively, where all sets are closed subsets of $\mathbb{R}^{n_x}$. Following closely [54], these sets, in turn, yield corresponding space-time sets $\mathbb{S}$, $\mathbb{O}$, and $\mathbb{T}$, which are all closed subsets of $\mathbb{R}^{n_x} \times [0, T]$:

$$\mathbb{S} := \bigcup_{t \in [0,T]} \mathcal{S}_t \times \{t\}, \quad \mathbb{T} := \bigcup_{t \in [0,T]} \mathcal{T}_t \times \{t\},$$

$$\mathbb{O} := \bigcup_{t \in [0,T]} \mathcal{O}_t \times \{t\}. \tag{3.3}$$

The start, target, and obstacle sets are further assumed to evolve "smoothly" in time. Specifically, a set $\mathcal{M}_t$ is said to evolve smoothly in time if there exists a Lipschitz continuous function $\boldsymbol{g}_{\mathcal{M}}(\boldsymbol{\xi}) : \mathbb{R}^n \to \mathbb{R}^n$ such that for the system

$$\dot{\boldsymbol{\xi}} = \boldsymbol{g}_{\mathcal{M}}(\boldsymbol{\xi}), \tag{3.4}$$

all trajectories that start in $\mathcal{M}_t$ at some time t stay in the set $\mathcal{M}_{\bar{t}}$ at all subsequent times $\bar{t} \in [t, T]$. That is,

$$\boldsymbol{\xi}_{t,\boldsymbol{x}}(\bar{t}) \in \mathcal{M}_{\bar{t}} \qquad \forall t \in [0, T],\ \forall \boldsymbol{x} \in \mathcal{M}_t,\ \forall \bar{t} \in [t, T]. \tag{3.5}$$

Practically, this implies that the dynamic start, target, and obstacle sets cannot teleport or disappear in the state space.

3.2.3 Reachability Sets and Tubes

In reachability analysis, backward and forward reachable sets or tubes are commonly needed [7]. The maximal sets and tubes encompass all the states to which the system can be driven to when going forward or backward through time, avoiding dynamic obstacles. These maximal sets and tubes can be defined as follows [7, 22, 23]:

Backward Reachable Set (BRS)

Given a specified final time $t_f \in [0, T]$, the BRS at time $t \le t_f$ is the set of all states at time t that can reach a target set $\mathcal{T}_{t_f}$ *exactly* at the final time t_f:

$$\mathcal{R}(t, t_f, \mathcal{T}_{t_f}, \mathbb{O}) = \{\hat{\boldsymbol{x}} \mid \exists \boldsymbol{u} \in \mathbb{U}, \ \boldsymbol{x} = \hat{\boldsymbol{x}},$$

$$\boldsymbol{\xi}_{t, \boldsymbol{x}}^{\boldsymbol{u}(\cdot)}(t_f) \in \mathcal{T}_{t_f} \wedge \forall s \in [t, t_f], \ \boldsymbol{\xi}_{t, \boldsymbol{x}}^{\boldsymbol{u}(\cdot)}(s) \notin \mathcal{O}_s\}. \tag{3.6}$$

Backward Reachable Tube (BRT)

BRTs extend BRSs. Given a specified final time $t_f \in [0, T]$, the BRT at time $t < t_f$ is the set of all states that can reach a time-varying target $\mathbb{T} \subset \mathbb{R}^{n_x} \times [0, T]$ at any time $\bar{t} \in [t, t_f]$:

$$\bar{\mathcal{R}}(t, t_f, \mathbb{T}, \mathbb{O}) = \{\hat{\boldsymbol{x}} \mid \exists \boldsymbol{u} \in \mathbb{U}, \ \exists \bar{t} \in [t, t_f], \ \boldsymbol{x} = \hat{\boldsymbol{x}},$$

$$\boldsymbol{\xi}_{t, \boldsymbol{x}}^{\boldsymbol{u}(\cdot)}(\bar{t}) \in \mathcal{T}_{\bar{t}} \wedge \forall s \in [t, t_f], \ \boldsymbol{\xi}_{t, \boldsymbol{x}}^{\boldsymbol{u}(\cdot)}(s) \notin \mathcal{O}_s\}. \tag{3.7}$$

Forward Reachable Set (FRS)

Given a specified start time $t_s \in [0, T]$, the FRS at time $t \ge t_s$ is the set of all states that can be reached at time t when starting from a state within the set $\mathcal{S}_{t_s}$ at time t_s:

$$\mathcal{F}(t, t_s, \mathcal{S}_{t_s}, \mathbb{O}) = \{\hat{\boldsymbol{x}} \mid \exists \boldsymbol{u} \in \mathbb{U}, \ \exists \boldsymbol{x} \in \mathcal{S}_{t_s},$$

$$\boldsymbol{\xi}_{t_s, \boldsymbol{x}}^{\boldsymbol{u}(\cdot)}(t) = \hat{\boldsymbol{x}} \wedge \forall s \in [t_s, t], \ \boldsymbol{\xi}_{t_s, \boldsymbol{x}}^{\boldsymbol{u}(\cdot)}(s) \notin \mathcal{O}_s\} \tag{3.8}$$

Forward Reachable Tube (FRT)

FRTs extend FRSs. Given a specified start time $t_s \in [0, T]$, the FRT at time $t > t_s$ is the set of all states that can be reached when launched from a state from a time-varying start

set $\mathbb{S} \subset \mathbb{R}^{n_x} \times [0, T]$ at any time $\bar{t} \in [t_s, t]$:

$$\bar{\mathcal{F}}(t, t_s, \mathbb{S}, \mathbb{O}) = \{\hat{\boldsymbol{x}} \mid \exists \boldsymbol{u} \in \mathbb{U}, \ \exists \bar{t} \in [t_s, t], \ \exists \boldsymbol{x} \in \mathcal{S}_{\bar{t}},$$
$$\boldsymbol{\xi}_{\bar{t}, \boldsymbol{x}}^{\boldsymbol{u}(\cdot)}(t) = \hat{\boldsymbol{x}} \wedge \forall s \in [\bar{t}, t], \ \boldsymbol{\xi}_{\bar{t}, \boldsymbol{x}}^{\boldsymbol{u}(\cdot)}(s) \notin \mathcal{O}_s\} \tag{3.9}$$

3.2.4 Problem Statement

Given a dynamical system of the form (3.1) operating in a dynamic environment with obstacles and possibly affected by other dynamic fields, our goal is to obtain equations that govern the backward and forward reachability tubes, as well as schemes that solve these equations efficiently:

Backward Reachability

Given a final time $t_f \in [0, T]$, a time $t < t_f$, and time-varying target and obstacle sets that define space-time sets $\mathbb{T}$ and $\mathbb{O}$, Eq. (3.3), we seek to derive and solve the equations for the BRTs, $\bar{\mathcal{R}}(t, t_f, \mathbb{T}, \mathbb{O})$, Eq. (3.7).

Forward Reachability

Given a start time $t_s \in [0, T]$, a time $t > t_s$, and time-varying start and obstacle sets that define space-time sets $\mathbb{S}$ and $\mathbb{O}$, Eq. (3.3), we seek to derive and solve the equations for the FRTs, $\bar{\mathcal{F}}(t, t_s, \mathbb{S}, \mathbb{O})$, Eq. (3.9).

Once the BRTs and/or FRTs are computed $\forall(t, t_f)$ and/or $\forall(t_s, t)$, they can be used to compute various other quantities of interest. Such quantities include: time-to-reach maps, i.e. maps of the minimum travel time to the target given the present state and time; start time vs. duration plots, i.e. function that maps the travel time to the target to the time at which the trajectory starts given a start state; and time-to-leave maps, i.e. maps of the latest time at which one can depart from the start state and reach the target point at a given time. The computation of these secondary quantities is discussed in Section 3.3.3

3.3 Multi-Time Reachability for Dynamic Sets

We now develop the theory and obtain the governing equations for HJ multi-time reachability for systems operating in dynamic environments. We start with multi-time reachability in the backward context, i.e. predict backward reachable tubes for time-varying target sets. We use continuous-time, optimal control and show how the resulting value function elegantly captures not only the backward reachable tubes but also time-to-reach maps. We then extend the results to the forward counterpart, i.e. predict forward reachable tubes for time-varying start sets. Finally, we present remarks and discuss secondary quantities such as time-to-reach and time-to-leave maps as well as start time vs. duration plots.

3.3.1 Backward Multi-Time Reachability

Augmented Dynamics

To account for the dynamic target and obstacle sets, we define a new augmented dynamical system as follows:

$$
\dot{\boldsymbol{\xi}} = f_a(\boldsymbol{\xi}, \boldsymbol{u}, s) = \begin{cases} g_{\mathcal{O}}(\boldsymbol{\xi}, s), & \boldsymbol{\xi} \in \mathcal{O}_s \\ g_{\mathcal{T}}(\boldsymbol{\xi}, s), & \boldsymbol{\xi} \in \mathcal{T}_s \text{ and } \boldsymbol{\xi} \notin \mathcal{O}_s \\ f(\boldsymbol{\xi}, \boldsymbol{u}, s), & \text{otherwise} \end{cases} \tag{3.10}
$$

where $g_{\mathcal{O}}(\boldsymbol{\xi}, s)$ and $g_{\mathcal{T}}(\boldsymbol{\xi}, s)$ are functions that keep trajectories within their respective sets as defined by Eq. (3.4). With this augmentation, we provide valuable properties to the system. First, once a state enters an obstacle set, it will remain in that set for all subsequent times irrespective of the controls applied. Second, the same holds for states that enter the target set. These properties will be shown to be key in our optimal control setting.

Optimal Control

For our optimal control problem, we first define the terminal cost at time T,

$$l_{term}(\boldsymbol{\xi}) = \begin{cases} \infty, & \boldsymbol{\xi} \in \mathcal{O}_T \\ d(\boldsymbol{\xi}, \mathcal{T}_T), & \text{otherwise} \end{cases}. \tag{3.11}$$

Eq. (3.11) defines the terminal cost of a state in the obstacle set to be infinitely high (in Section 3.4 we address how this property can be numerically handled). For all other states, the cost is defined as the distance of the state ($\boldsymbol{\xi}$) from the target set at the terminal time ($\mathcal{T}_T$) under some distance metric d which depends on the system at hand. Being a distance metric, we require $d(\boldsymbol{\xi}, \mathcal{T}_T) \geq 0 \; \forall (\boldsymbol{\xi}, \mathcal{T}_T)$ and $d(\boldsymbol{\xi}, \mathcal{T}_T) = 0$ if and only if $\boldsymbol{\xi} \in \mathcal{T}_T$.

The running cost is defined as a constant negative value at the target set and zero everywhere else

$$l(\boldsymbol{\xi}, s) = \begin{cases} -\alpha, & \boldsymbol{\xi} \in \mathcal{T}_s \text{ and } \boldsymbol{\xi} \notin \mathcal{O}_s \\ 0, & \text{otherwise} \end{cases}, \tag{3.12}$$

where α is an arbitrary positive constant which we set to 1. The solution is exact irrespective of the value of α. Values of α can however be used to minimize numerical errors due to discontinuities that arise out of this loss function (not shown).

Using the augmented dynamics (3.10), terminal cost (3.11), and running cost (3.12), the total cost function incurred when using controls $\boldsymbol{u}(\cdot)$ and initial state $\boldsymbol{x}$ at initial time t is

$$J(\boldsymbol{x}, \boldsymbol{u}(\cdot), t) = l_{term}(\boldsymbol{\xi}_{t,\boldsymbol{x}}^{\boldsymbol{u}(\cdot)}(T)) + \int_t^T l(\boldsymbol{\xi}_{t,\boldsymbol{x}}^{\boldsymbol{u}(\cdot)}(s), s) ds \tag{3.13}$$

To obtain an intuition for the meaning of the total cost, we substitute the functions for

the case when the trajectory $\boldsymbol{\xi}_{t,\boldsymbol{x}}^{\boldsymbol{u}(\cdot)}(s)$ never enters the obstacle set,

$$J(\boldsymbol{x}, \boldsymbol{u}(\cdot), t) = \underbrace{d(\boldsymbol{\xi}_{t,\boldsymbol{x}}^{\boldsymbol{u}(\cdot)}(T), \mathcal{T}_T)}_{\substack{\text{Terminal distance} \\ \text{from target set}}} - \alpha \underbrace{\int_t^T \mathbb{I}_{\mathcal{T}_s}\left(\boldsymbol{\xi}_{t,\boldsymbol{x}}^{\boldsymbol{u}(\cdot)}(s)\right) ds}_{\text{Time spent in target set}} \tag{3.14}$$

where the identity function $\mathbb{I}_{\mathcal{T}_s}(\boldsymbol{\xi}) = 1$ when $\boldsymbol{\xi} \in \mathcal{T}_s$ and is 0 otherwise. We note that if the trajectory ever enters the obstacle set, it will stay in the obstacle set at the terminal time under the augmented dynamics and will incur an infinitely high total cost. Additionally, the value function under the optimal control for trajectories that avoids the obstacles is,

$$J^*(\boldsymbol{x}, t) = \min_{\boldsymbol{u}(\cdot) \in \mathbb{U}} \left[d(\boldsymbol{\xi}_{t,\boldsymbol{x}}^{\boldsymbol{u}(\cdot)}(T), \mathcal{T}_T) - \alpha \int_t^T \mathbb{I}_{\mathcal{T}_s}\left(\boldsymbol{\xi}_{t,\boldsymbol{x}}^{\boldsymbol{u}(\cdot)}(s)\right) ds \right] \tag{3.15}$$

To explain this minimization physically, we consider two cases. In the first, we assume there exists some control that drives the system from initial state $\boldsymbol{x}$ (or set) at time t into the target set at a time $\bar{t} \in [t, T]$ while avoiding the obstacles. In the opposive second, we assume no control can drive the system to the target set while avoiding the obstacles.

Case 1 Let $\boldsymbol{u}^*(\cdot)$ be the set of controls that drives the system from state $\boldsymbol{x}$ at time t (under the augmented dynamics) to the target set at the earliest possible time $t^* = \min(\bar{t})$ while avoiding the dynamic obstacle set $\mathbb{O}$. We reiterate that for the augmented system (3.10), if the target set is reached at some $t^* < T$, the system will stay in the set at all future times and hence $\boldsymbol{\xi}_{t,\boldsymbol{x}}^{\boldsymbol{u}(\cdot)}(T) \in \mathcal{T}_T$. It follows then that the cost for such a set of controls is:

$$J(\boldsymbol{x}, \boldsymbol{u}^*(\cdot), t) = \underbrace{d(\boldsymbol{\xi}_{t,\boldsymbol{x}}^{\boldsymbol{u}(\cdot)}(T), \mathcal{T}_T)}_{0} - \alpha \underbrace{\int_t^T \mathbb{I}_{\mathcal{T}_s}\left(\boldsymbol{\xi}_{t,\boldsymbol{x}}^{\boldsymbol{u}(\cdot)}(s)\right) ds}_{T-t^*}$$

$$= -\alpha(T - t^*).$$

We now provide the lower bound of the value function (3.15) under the optimal control

$$
J^*(\boldsymbol{x}, t) = \min_{\boldsymbol{u}(\cdot) \in \mathbb{U}} \left[d(\boldsymbol{\xi}_{t,\boldsymbol{x}}^{\boldsymbol{u}(\cdot)}(T), \mathcal{T}_T) - \right.
$$

$$
\left. \alpha \int_t^T \mathbb{I} \left\{ \boldsymbol{\xi}_{t,\boldsymbol{x}}^{\boldsymbol{u}(\cdot)}(s) \in \mathcal{T}_s \right\} ds \right] \tag{3.16}
$$

$$
\geq \min_{\boldsymbol{u}(\cdot) \in \mathbb{U}} \left[d(\boldsymbol{\xi}_{t,\boldsymbol{x}}^{\boldsymbol{u}(\cdot)}(T), \mathcal{T}_T) \right]
$$

$$
+ \min_{\boldsymbol{u}(\cdot) \in \mathbb{U}} \left[-\alpha \int_t^T \mathbb{I} \left\{ \boldsymbol{\xi}_{t,\boldsymbol{x}}^{\boldsymbol{u}(\cdot)}(s) \in \mathcal{T}_s \right\} ds \right] \tag{3.17}
$$

$$
J^*(\boldsymbol{x}, t) \geq -\alpha(T - t^*). \tag{3.18}
$$

This lower bound is achieved under the control $\boldsymbol{u}^*$. Therefore, when the vehicle can reach the destination, the optimal control under the given loss function generates a time optimal trajectory to the target state. The value function is given by $J^*(\boldsymbol{x}, t) = -\alpha(T - t^*)$ where t^* is the minimum time at which a trajectory starting at $(\boldsymbol{\xi}, t)$ can reach the target state.

Case 2 When there exists no control $\boldsymbol{u}(\cdot)$ that can drive the system from $(\boldsymbol{x}, t)$ to the target set while avoiding the obstacles, the term $\mathbb{I}_{\mathcal{T}_s} \left(\boldsymbol{\xi}_{t,\boldsymbol{x}}^{\boldsymbol{u}(\cdot)}(s) \right)$ in the value function (3.15) is always 0 by construction. It follows then that:

$$
J^*(\boldsymbol{x}, t) = \min_{\boldsymbol{u}(\cdot) \in \mathbb{U}} \left[l_{term}(\boldsymbol{\xi}_{t,\boldsymbol{x}}^{\boldsymbol{u}(\cdot)}(T)) \right] \tag{3.19}
$$

That is, when a trajectory with initial conditions $(\boldsymbol{x}, t)$ cannot reach the target set, the minimization of the cost function will lead the system as close to the target set as possible while avoiding the obstacle (since hitting the obstacle will drive the terminal cost infinitely high).

To summarize, the value function corresponding to the optimal control problem is given

as

$$J^*(\boldsymbol{x}, t) = \begin{cases} -\alpha(T - \min(\bar{t})), & \text{if } \exists \boldsymbol{u}(\cdot) \text{ s.t.} \\ & \qquad \boldsymbol{\xi}_{t,\boldsymbol{x}}^{\boldsymbol{u}(\cdot)}(\bar{t}) \in \mathcal{T}_{\bar{t}} \\ \infty, & \text{if } \nexists \boldsymbol{u}(\cdot) \text{ s.t.} \\ & \qquad \boldsymbol{\xi}_{t,\boldsymbol{x}}^{\boldsymbol{u}(\cdot)}(\bar{t}) \notin \mathcal{O}_{\bar{t}} \\ & \qquad \forall \bar{t} \in [t, T] \\ \min_{\boldsymbol{u}} d(\boldsymbol{\xi}_{t,\boldsymbol{x}}^{\boldsymbol{u}(\cdot)}(T), \mathcal{T}_T), & \text{Otherwise.} \end{cases} \tag{3.20}$$

In other words, at any state $\boldsymbol{x}$ at a time $t \in [0, T]$, the value of $J^*(\boldsymbol{x}, t)$, if negative, physically implies that a state starting at $\boldsymbol{x}$ at time t can reach the target set before the terminal time T. Moreover, the earliest time that it can reach the destination is given by $T + \frac{J^*(\boldsymbol{x},t)}{\alpha}$. If the value of $J^*(\boldsymbol{x}, t)$ is positive, it implies that a state starting at $\boldsymbol{x}$ at time t cannot reach the target set in the time interval $[t, T]$, and the value physically corresponds to how close such a state could possibly get to the target set at the terminal time T. Finally, for states for which $J^*(\boldsymbol{x}, t)$ is infinite, we have that for a system starting at $\boldsymbol{x}$ at time t, the obstacle will inevitably be hit.

The Hamilton-Jacobi-Bellman Equation

The value function can be efficiently computed using dynamic programming. For continuous-time optimal control, it is the viscosity solution of the Hamilton-Jacobi-Bellman (HJB) partial differential equation (PDE) [12, 48, 91]

$$\frac{\partial J^*(\boldsymbol{x}, t)}{\partial t} + \min_{\boldsymbol{u}} \left[l(\boldsymbol{x}, t) + \nabla_{\boldsymbol{x}} J^* \cdot f_a(\boldsymbol{x}, \boldsymbol{u}, t) \right] = 0$$

$$J^*(\boldsymbol{x}, T) = l_{term}(\boldsymbol{x}), \tag{3.21}$$

where l_{term} and l are the terminal and running costs, respectively. For our problem, these costs are defined in Eqs. (3.11) and (3.12). Inserting them and the augmented dynamical system (3.10) in Eq. (3.21), we obtain the final HJB PDE:

$$\frac{\partial J^*(\boldsymbol{x},t)}{\partial t} = \begin{cases} -\left[-\alpha + \nabla_{\boldsymbol{x}}J^* \cdot g_{\mathcal{T}}(\boldsymbol{x},t)\right], & \boldsymbol{x}(t) \in \mathcal{T}_t \cap (\mathcal{O}_t)^c \\ -\left[\nabla_{\boldsymbol{x}}J^* \cdot g_{\mathcal{O}}(\boldsymbol{x},t)\right], & \boldsymbol{x}(t) \in \mathcal{O}_t \\ -\min_{\boldsymbol{u}}\left[\nabla_{\boldsymbol{x}}J^* \cdot f(\boldsymbol{x},\boldsymbol{u},t)\right], & \text{otherwise} \end{cases}$$

$$J^*(\boldsymbol{x},T) = \begin{cases} \infty, & \boldsymbol{x} \in \mathcal{O}_T \\ d(\boldsymbol{x},\mathcal{T}_T), & \text{otherwise} \end{cases}. \tag{3.22}$$

Eq. (3.22) is a terminal-value problem which is solved backward in time to obtain the value of $J^*(\boldsymbol{x},t)$ for all states in the state space and all times $t \in [0,T]$.

Equation for Backward Reachable Tubes

Using the value function J^* governed by the HJB PDE (3.22), we now obtain the equation for the BRTs defined by Eq. (3.7) as well as an efficient scheme for their computation. Consider a fixed time $t_f \in [0,T]$ and a time $t < t_f$. From Eq. (3.20), it follows that for any state $\boldsymbol{x}$ satisfying $J^*(\boldsymbol{x},t) \le -\alpha(T - t_f)$, a control function $\boldsymbol{u}(\cdot)$ exists that will drive the system from state $\boldsymbol{x}$ at time t to the target set at some time $\bar{t} \in [t, t_f]$. This results in an efficient scheme to compute the BRT:

$$\bar{\mathcal{R}}(t, t_f, \mathbb{T}, \mathbb{O}) = \{\boldsymbol{x} \mid J^*(\boldsymbol{x},t) \le -\alpha(T - t_f)\}. \tag{3.23}$$

For a specified final time t_f, the BRT at any time $t < t_f$ can simply be extracted by considering the appropriate sub-level set of the value function at that time. This is because an agent in this set would reach the target while avoiding the obstacle at $t < t_f$ under the optimal control and stay in the target because of the augmented dynamics 3.10 accumulating

45

the negative cost at the destination.

Equation for Time-to-Reach Maps

The value function stores important information regarding the optimal time a system can reach the target set. This can be used to compute time-to-reach or duration maps $\mathcal{D}$ from Eq. (3.21) or (3.22):

$$\mathcal{D}(\boldsymbol{x}, t) = T + \frac{J^*(\boldsymbol{x}, t)}{\alpha} - t, \qquad \forall (\boldsymbol{x}, t) \text{ s.t., } J^*(\boldsymbol{x}, t) < 0.$$

For a state $\boldsymbol{x}$ at time t satisfying $J^*(\boldsymbol{x}, t) \leq 0$, Eq. (3.20) implies that such a state can reach the target set and the earliest possible time this will happen will be at $T + \frac{J^*(\boldsymbol{x},t)}{\alpha}$. It follows then that for all $(\boldsymbol{x}, t)$ with $J^*(\boldsymbol{x}, t) \leq 0$, $\mathcal{D}(\boldsymbol{x}, t)$ corresponds to the minimum duration for a trajectory starting at state $\boldsymbol{x}$ at time t to reach the target set.

Closed-loop optimal controller

As discussed in Section 3.3.1, an optimal controller that minimizes the cost function will: (a) avoid dynamic obstacles; (b) reach the target in minimum time if it can; and (c), reach as close to the target as possible if it cannot reach it. The optimal controller can also compute the minimum duration to the target set from the current state. Thus, solving for $J^*(\boldsymbol{x}, t)$ using Eq. (3.22) provides a powerful closed-loop control policy:

$$\pi(\boldsymbol{x}, t) = \underset{\boldsymbol{u}}{\arg\min} \left[\nabla_{\boldsymbol{x}} J^*(\boldsymbol{x}, t) \cdot f(\boldsymbol{x}, \boldsymbol{u}, t) \right] \ \forall \boldsymbol{x} \notin (\mathcal{O}_t \cup \mathcal{T}_t) \ ,$$

as demonstrated with reliable navigation in complex time-varying ocean currents with forecast errors [205].

3.3.2 Forward Multi-Time Reachability

Section 3.3.1 addressed backward multi-time reachability. That is, we considered how to efficiently compute backward reachable tubes (and time-to-reach maps) in a dynamic environment with time-varying target and obstacle sets. In this section, we examine the forward counterpart, and derive how to compute forward reachable tubes in dynamic domains containing now time-varying start sets.

The forward problem can be addressed analogously to the derivation in Section 3.3.1, but now analyzing the system evolution *backwards* in time. First, an augmented dynamic system akin to Eq. (3.10) can be defined as follows:

$$
\dot{\boldsymbol{\xi}} = \tilde{f}_a(\boldsymbol{\xi}, \boldsymbol{u}, s) = \begin{cases} g_{\mathcal{O}}(\boldsymbol{\xi}, s), & \boldsymbol{\xi} \in \mathcal{O}_s \\ g_{\mathcal{S}}(\boldsymbol{\xi}, s), & \boldsymbol{\xi} \in \mathcal{S}_s \text{ and } \boldsymbol{\xi} \notin \mathcal{O}_s \\ f(\boldsymbol{\xi}, \boldsymbol{u}, s), & \text{otherwise} \end{cases} \tag{3.24}
$$

where now the start set is used instead of the target set. This system's evolution backwards in time can be studied by mapping time to a new "reverse-time" variable, $\tau(t) = T - t$, resulting in a mapped augmented dynamical system:

$$
\frac{d\boldsymbol{\xi}}{d\tau} = -\tilde{f}_a(\boldsymbol{\xi}, \boldsymbol{u}, T - \tau). \tag{3.25}
$$

Analogous to backward multi-time reachability, we can formulate an optimal control for the system (3.25) while using the start set in place of the target set. Specifically, we define a terminal cost, now at time $\tau = T$, of the form:

$$
\tilde{l}_{term}(\boldsymbol{\xi}) = \begin{cases} \infty, & \boldsymbol{\xi} \in \mathcal{O}_0 \\ d(\boldsymbol{\xi}, \mathcal{S}_0), & \text{otherwise} \end{cases}. \tag{3.26}
$$

To remain consistent with the set indexing convention introduced in Section 3.2.2, the sets

in Eq. (3.26) are evaluated at time $t = 0$ (corresponds to the "terminal" reverse-time $\tau = T$). Moreover, a running cost can be similarly defined:

$$\tilde{l}(\boldsymbol{\xi}, \tau) = \begin{cases} -\alpha, & \boldsymbol{\xi} \in \mathcal{S}_{(T-\tau)} \text{ and } \boldsymbol{\xi} \notin \mathcal{O}_{(T-\tau)} \\ 0, & \text{otherwise} \end{cases}, \tag{3.27}$$

The value function for this optimal control problem can again be computed by forming a HJB PDE using now the dynamical system (3.24), terminal cost (3.26), and running cost (3.27). Mapping the resulting HJB PDE back to the original time variable t so as to not have to explicitly work in reverse-time τ, the HJB PDE can be shown to be given as:

$$\frac{\partial \tilde{J}^*(\boldsymbol{x}, t)}{\partial t} + \max_{\boldsymbol{u}} \left[-\tilde{l}(\boldsymbol{x}, t) + \nabla_{\boldsymbol{x}} \tilde{J}^* \cdot \tilde{f}_a(\boldsymbol{x}, \boldsymbol{u}, t) \right] = 0$$

$$\tilde{J}^*(\boldsymbol{x}, 0) = \tilde{l}_{term}(\boldsymbol{x}), \tag{3.28}$$

which, upon inserting the augmented dynamics (3.24), and the costs (3.26) and (3.27), yields:

$$\frac{\partial \tilde{J}^*(\boldsymbol{x}, t)}{\partial t} = \begin{cases} -\left[\alpha + \nabla_{\boldsymbol{x}} J^* \cdot g_{\mathcal{S}}(\boldsymbol{x}, t) \right], & \boldsymbol{x}(t) \in \mathcal{S}_t \cap (\mathcal{O}_t)^c \\ -\left[\nabla_{\boldsymbol{x}} J^* \cdot g_{\mathcal{O}}(\boldsymbol{x}, t) \right], & \boldsymbol{x}(t) \in \mathcal{O}_t \\ -\max_{\boldsymbol{u}} \left[\nabla_{\boldsymbol{x}} J^* \cdot f(\boldsymbol{x}, \boldsymbol{u}, t) \right], & \text{Otherwise} \end{cases}$$

$$\tilde{J}^*(\boldsymbol{x}, 0) = \begin{cases} \infty, & \boldsymbol{x} \in \mathcal{O}_0 \\ d(\boldsymbol{x}, \mathcal{S}_0), & \text{otherwise} \end{cases}. \tag{3.29}$$

In duality to the backward multi-reach setting where a terminal-value problem was obtained, in this case the value function $\tilde{J}^*(\boldsymbol{x}, t)$ is given as the solution to an initial value problem. Furthermore, analogous to the backward setting, the value function can be used to extract

the FRT,

$$\bar{\mathcal{F}}(t, t_s, \mathbb{S}, \mathbb{O}) = \{\boldsymbol{x} \mid \tilde{J}^*(\boldsymbol{x}, t) \leq -\alpha \cdot t_s\}, \tag{3.30}$$

and the time-to-leave maps,

$$\tilde{\mathcal{D}}(\boldsymbol{x}, t) = -\frac{\tilde{J}^*(\boldsymbol{x}, t)}{\alpha}, \qquad \forall (\boldsymbol{x}, t) \text{ s.t., } \tilde{J}^*(\boldsymbol{x}, t) < 0. \tag{3.31}$$

In comparison to backward reachability, the optimal controller obtained by working in reverse-time allows computing the start set as quickly as possible in a reverse-time setting. This is not as commonly useful since the universe runs forward in time, thus usually requiring an open-loop controller to execute the corresponding trajectories.

3.3.3 Remarks and Discussion

With the evolution equations derived for multi-time reachability, we now present several properties and differences when compared to classic reachability.

Ability to compute BRTs / FRTs with arbitrary start and end times

We note that we require a single solve of the PDE 3.22 / 3.29 to compute all possible BRTs / FRTs for a given dynamical system, target/start set, and obstacle set using Eq. (3.23) / (3.30). With classic reachability, one would instead a solve of a HJB PDE for every terminal time t_f, or start time t_s. While this benefit is inconsequential when dealing with a time-invariant system (since the backward and forward reachability tubes depend only on the time duration, $t_f - t$ and $t - t_s$, respectively), this property is very useful for analyzing dynamic systems. Many multi-time autonomy problems today indeed involve dynamic environments governed by PDEs (e.g., UAVs or AUVs affected by currents or winds), dynamic target / start sets, and / or dynamic obstacle sets [135]. Multi-time reachability thus has strong appeal.

While finishing this work, [128] posted a related framework that also adds a running cost to the HJB equation. Presently however, we derive and apply the exact governing equations for BRTs / FRTs and associated quantities, for the first time for systems operating in time-varying environments with dynamic obstacles and affected by other dynamic fields.

Field of Level Sets

In classical reachability, only the data on the zero level set of the value function is typically used, as this decomposes the space into the reachable and non-reachable regions which is usually what is of interest In multi-time reachability, a PDE of essentially identical complexity is solved, yet every value on the field provides useful physical reachability information. Specifically, in the backward reachability setting, the physical meaning of other level sets of the value function is given by Eq. (3.20). In this case, we reiterate, level sets with a negative value provide minimum times at which a target set can be reached from a given state, level sets with a positive value correspond to the closest distance to the target that can be reached for states that cannot reach the target, and finally an infinite value for J^* are states where it is unavoidable that an obstacle will be hit. The case of forward reachability has a similar physical interpretation for its different level sets.

Secondary quantities

While the value function obtained by classical backward reachability determines if one can reach the destination by time t_f given a starting time and position, the value function obtained using multi-time backward reachability determines *when* one can reach the target set $(\mathcal{D}(\boldsymbol{x}, t))$. When evaluated at a given position $\boldsymbol{x}$, one can infer the map between the starting time of the trajectory to the duration it takes to reach the target. Similarly, the forward value function determines *when* to start a journey to be able to reach an arbitrary point from the starting set $(\tilde{\mathcal{D}}(\boldsymbol{x}, t))$. This information can be extremely valuable for time varying systems where the time to reach the destination can vary drastically with the time

at which the trajectory starts. We refer to the resulting plots as duration vs. arrival time, and start time vs. duration.

Optimal Controller

The closed loop controller under the value function for multi-time reachability (Sect. 3.3.1) has varied desirable properties including obstacle avoidance, time optimality if the target is reachable, and distance to target minimized if not. This drastically augments classical reachability that only minimizes the terminal signed distance from the target set at time T and does not provide time optimality when the state is not on the zero level set.

3.4   Computation and Numerical Schemes

In Section 3.3, the PDEs (3.21)-(3.22) for the value function of backward reachability and PDEs (3.28)-(3.29) for the value function of forward reachability are HJB PDEs. These PDEs, including the existence, uniqueness, and properties of their viscosity solutions, have been extensively studied in recent years due to their broad applicability [48, 162, 186].

Several options exist for numerically computing a viscosity solution to a given HJB PDE, ranging from Finite Volume methods to high-order discontinuous Galerkin methods [75, 134, 135, 137, 148]. Presently, we used the method of lines, with high-order finite difference methods for the temporal and spatial discretization, on structured, uniform, rectangular meshes [13, 41]. Our software was built on top of an open-source HJ equation solver, hj_reachability [183], built on JAX [18]. To numerically compute the viscosity solution, the Local Lax-Friedrichs scheme was used [15, 41, 186].

Since the above scheme is fully explicit, the computational cost is $\mathcal{O}(N_x N_t)$ where N_x and N_t are the total number of spatial gridpoints and of timesteps, respectively. The explicit scheme allows direct parallelization of the computation across gridpoints. The cost of our method is thus exactly of the same order as that of classical reachability while providing

much richer information about the system.

Finally, we discuss two numerical implementation details: (1) Handling the infinite condition in the terminal cost for when a state terminates in an obstacle set, i.e. Eqs. (3.11) and (3.26), is straightforward. Since the numerical solve is inherently restricted to a closed and bounded state space, we simply set the terminal cost value when in an obstacle set to an arbitrary constant greater than the largest possible signed distance value in the domain at terminal time. When processing the final numerically computed value function, we simply mask off all values that equal this arbitrary constant as there are no controls that allow the system to avoid the obstacle. (2) The constant α in Eq. (3.12) can be chosen to decrease round off errors associated to the numerical solve. By setting α to the order of the characteristic time of the problem, the contours of interest will be $\mathcal{O}(1)$.

3.5 Numerical Results

We illustrate our theory and schemes on three numerical cases. In the first, we verify our method by applying it to a system with analytical reachability tubes. In the second and third cases, we consider more complex systems and demonstrate the various capabilities of our approach.

3.5.1 Analytical Moving Target and Obstacle

Problem Setup

This case uses the example of [54, Sec 5.1]. The 2D dynamical system consists of a vehicle moving with a constant speed in any heading, $\dot{\boldsymbol{x}} = u_{veh}\hat{\boldsymbol{h}}$, where the state $\boldsymbol{x} = [x, y]$ is the vehicle position, $\hat{\boldsymbol{h}}$ the unit heading, and $u_{veh} = 0.5$ the constant speed of the vehicle. The dynamic target set is a square of side length 0.4 units centered at $[0, 0.75]$ at $t = 0$ travelling with velocity of $[0, -1.5]$ units. The obstacle is a square of side length 0.2 initially centered at $[0, 0]$ and traveling with velocity of $[0, -1]$ units. Our goal is to compute backward

reachability tubes and compare them to the analytical solution we obtained geometrically using [54, Sec 5.1.1]. The augmented dynamics is here straightforward: we modify the system dynamics such that when the agent is in the target (/obstacle) it moves exactly with the known velocity of the target (/obstacle).

Results

Fig. 3.1 shows the analytical, overlaid on the numerical, backward reachability tubes using our multi-time reachability. The analytical and numerical tubes (left half of the domain) are effectively identical. When compared to the results in [54] that compute the BRTs for $t_f = 0.5$, our approach accurately computes tubes for all terminal times t_f and in a single PDE simulation.

3.5.2 Dynamic Dubin's Car

Problem Setup

We now consider a more complex $3D$ dynamical system often referred to as the Dubin's car. The state space of the car is given by its position and orientation: $\boldsymbol{x} = [x, y, \theta]$. The only control is that of the steering rate $\dot{\theta} = u_\alpha$. The dynamics is given by

$$\begin{bmatrix} \dot{x} & \dot{y} & \dot{\theta} \end{bmatrix}^T = \begin{bmatrix} v\cos\theta & v\sin\theta & u_\alpha \end{bmatrix}^T,$$

where $v = 1$ is the velocity of the car. We additionally constrain the steering rate to satisfy $|u_\alpha| < \frac{\pi}{3}$ units.

We add a moving target and moving obstacle with velocities $[0.4, 0]$ and $[0.2, 0]$, respectively. The positions of the target and obstacle at various times are shown in Fig. 3.2 (the target is blue and obstacle orange). Our goal is to compute backward reachable tubes as well as time-to-reach maps.
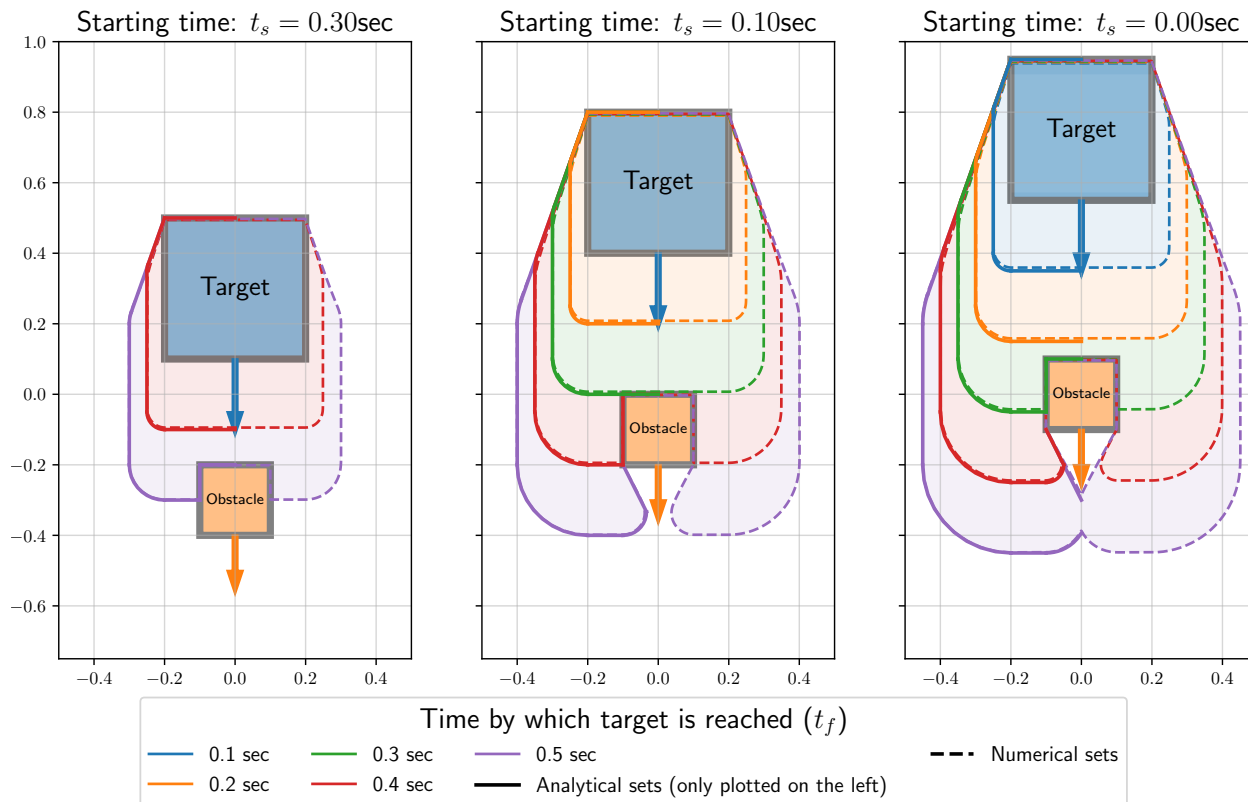
Figure 3.1: Backward reachability tubes for various start and end times. Analytically computed tubes are superimposed in the left half on top of numerically computed tubes (dashed line).

Results

Since the state space is $3D$, the value function now lives in a $3D$ space. To get an intuition of what kind of information can be gained from the value function, we consider the duration map at a slice $\mathcal{D}(x, y, \theta = 8.95^o, t)$ (Fig. 3.2). At a given (x, y) and time t, the duration map returns the amount of time needed to reach the target when starting at that position and time, and being initially aligned at the given angle (i.e. $\theta = 8.95^o$). As expected, states to the left of the target can reach the target set more easily given their initial orientation (states to the right need to turn around to reach the target set). In addition, note the triangular region which forms on the left of the obstacle, corresponding to regions where the car cannot avoid the obstacle.
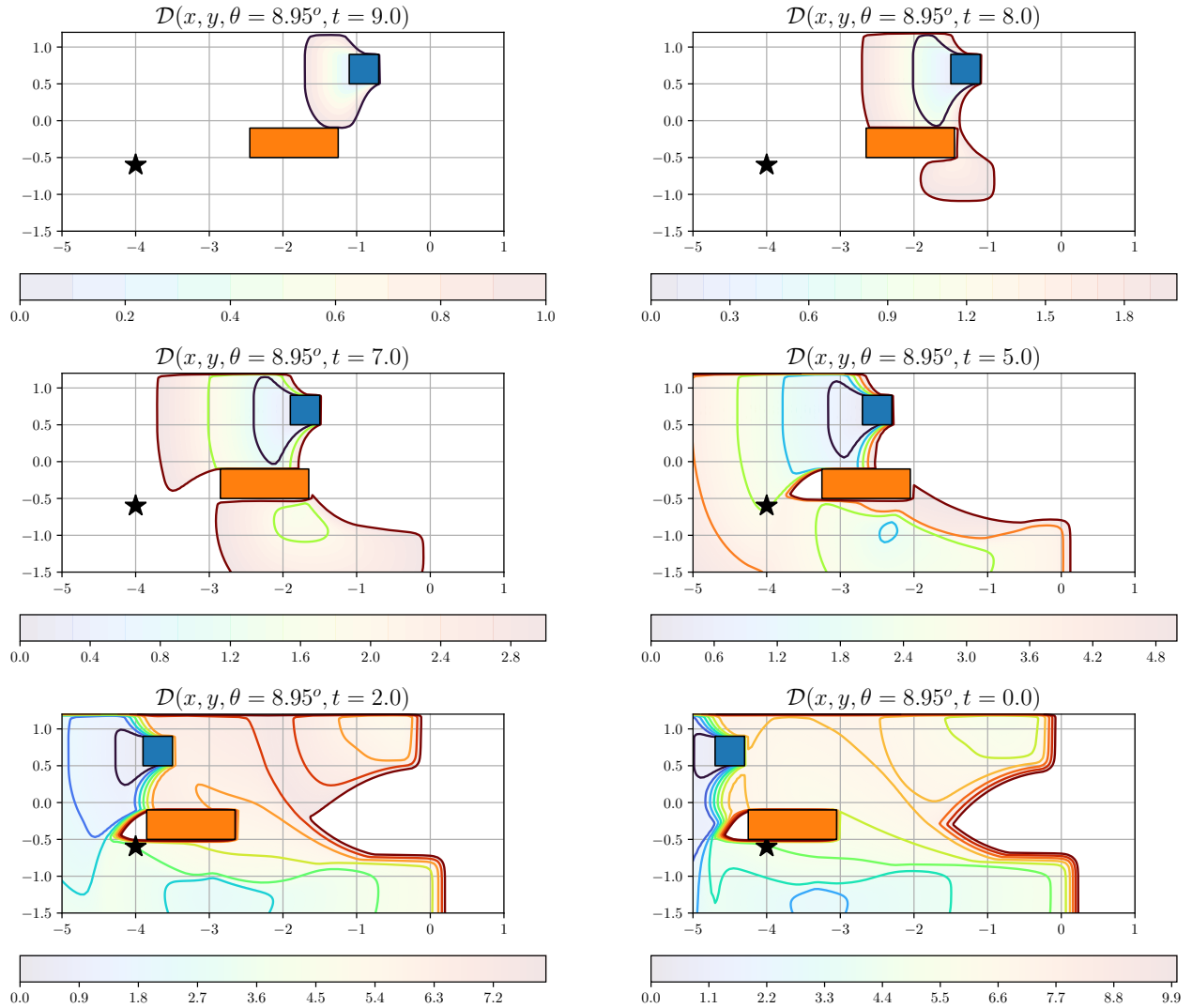
Figure 3.2: Slice of the duration map at $\theta = 8.95^o$. This map physically represents the time needed to reach the target set based on the initial position of the car. The point marked with the star denotes an arbitrary start point that is used in subsequent analysis (Fig. 3.5).

Fig. 3.2 highlights a key feature of the power of multi-time reachability. Consider the following question: given a start point (x_s, y_s, θ_s) (marked with a star), what is the minimum duration to the target as a function of the start time (t_s)? This information is readily available using the duration map, $\mathcal{D}(x_s, y_s, \theta_s, t_s)$, as seen in Fig. 3.3. As different contours of the duration map reach the start point, we see vastly different gradients of the value function – implying changing optimal control strategies based on when the car starts.

Suppose we pose another question: Given a start position (x_s, y_s) what is the optimal
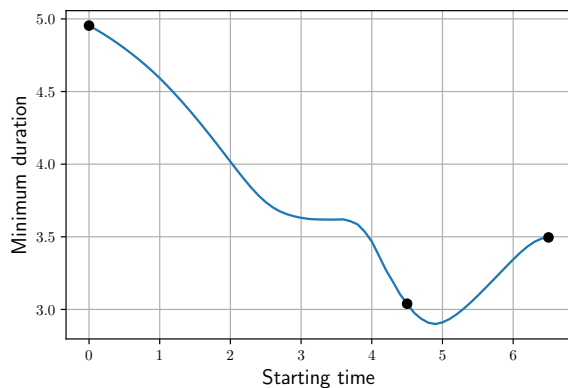
Figure 3.3: Duration of the journey to the target set as a function of the starting time. Since this is a time varying system, the duration is not constant. Due to the moving obstacle, the duration first decreases and increases. Times of interest are marked with a black dot.

starting angle at different starting times to minimize the duration to the target set? We can use the following expression to compute the duration under optimal θ as a function of the starting time t_s: $d(t_s) = \min_\theta \mathcal{D}(x_s, y_s, \theta, t_s)$. The corresponding optimal θ is given by $\arg\min_\theta \mathcal{D}(x_s, y_s, \theta, t_s)$. Fig. 3.4 shows, for a start position $(x_s, y_s) = (-3, -0.7)$, this minimum duration and optimal θ as a function of start time. These plots, trivially generated using the multi-time reachability value function, contain information that is invaluable in deciding when and how to start the journey from a given start point.
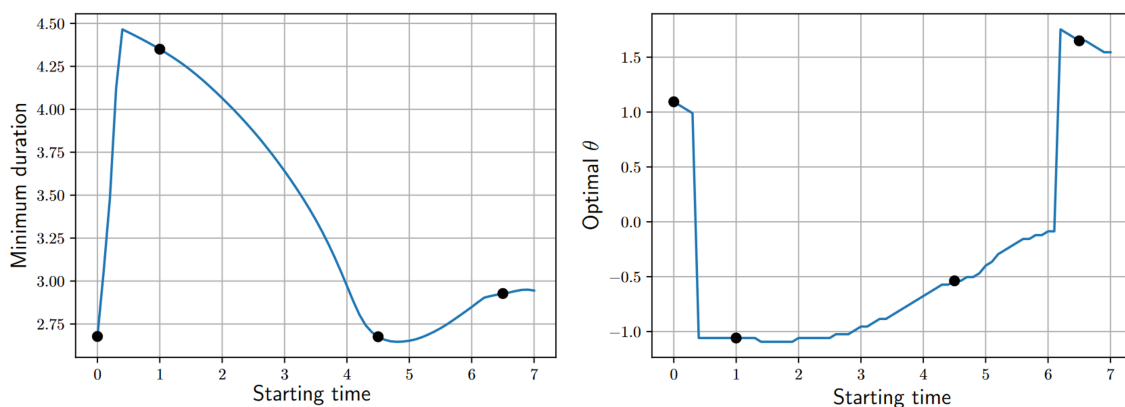
Figure 3.4: (Left) Minimum duration to reach the target set, given the starting position $(x_s, y_s) = (-3, -0.7)$, as a function of starting time (t_s). (Right) Initial angle θ_s under which this minimum duration can be achieved for each corresponding starting time. Points of interest are marked with black dots.

Different regimes of the optimal solution can be noted, as the car decides to start with

drastically different angles based on the starting time. To see why this is occurs, we plot the trajectories (Fig. 3.5) of all the points of interest marked with black dots in Figs. 3.3 and 3.4. The plot on the left traces out optimal trajectories when starting at the star (for various
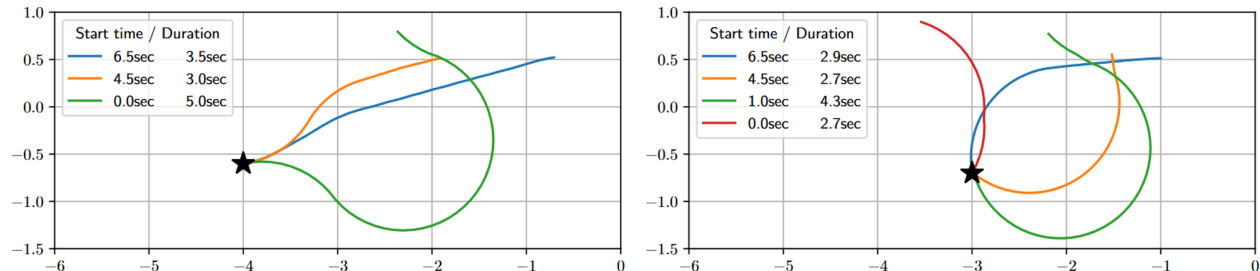
Figure 3.5: Trajectories for various start points, start times and start angles. (Left) Trajectories starting at fixed start point but with the optimal angle to reach the destination as early as possible. (Right) Trajectories start at a constrained position and angle. Both set of trajectories start at a user defined time and end at different times before the final time horizon T

start times marked in Fig. 3.3) while constraining the initial heading the vehicle must start with. We find that the duration initially falls with start time as cutting across the front of the obstacle is difficult for the agent given this constrained initial angle. The plot on the right corresponds to the trajectories starting at optimal θ at various times (Fig. 3.4). We see that early on, the optimal agent cuts across the front of the obstacle and heads straight for the target. If it starts later, it has to go out of its way to drive around the front of the obstacle. However, if it waits long enough, the agent can reach the target by traversing behind the obstacle.

This case shows how we compute optimal trajectories for a variety of starting positions, angles, and start/terminal times. We further note that these can all be efficiently computed using information from a *single* multi-time reachability PDE solve – something not possible with other approaches.

3.5.3 AUV in a Bottom Gravity Current Flow Field

Problem Setup

Finally, we showcase results when a time-varying dynamic environment affects the system and optimal control. We consider an AUV in $2D$ with state variables $\boldsymbol{x} = (x, z)$ where x and z are position and depth of the vehicle. We denote the dynamics by

$$\dot{\boldsymbol{x}} = \left[F_x \cos(u_\theta) + V_x(\boldsymbol{x}, t) \quad F_y \sin(u_\theta) + V_y(\boldsymbol{x}, t) \right]^T,$$

where u_θ is the sole control and $\boldsymbol{V} = [V_x, V_y]$ is the dynamic background ocean flow field that advects the AUV around. The background flow is that of a non-hydrostatic bottom gravity current simulated using our Finite Volume ocean modeling software [197]. This flow involves heavy salt water flowing down an incline and creating eddies due to Kevin-Helmholtz instabilities, as visualized in Fig. 3.6 [129].
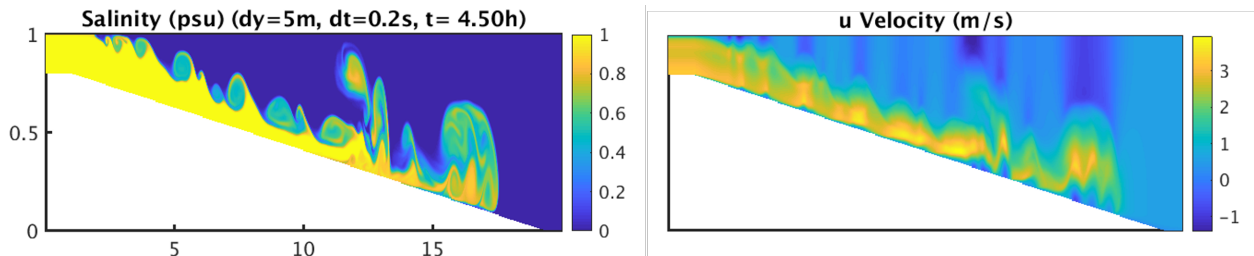
Figure 3.6: Salinity field (left) and x-component of the velocity field in m/s (right) for the bottom gravity flow. The units of x and y are in km.

Results

We consider a domain of interest at the bottom of the incline. As expected, we see that the duration map is uniform at the time before the current reaches the bottom, whereas it is non-uniform and time-varying at the time frame when the current and its billows and waves arrive (Fig. 3.7).
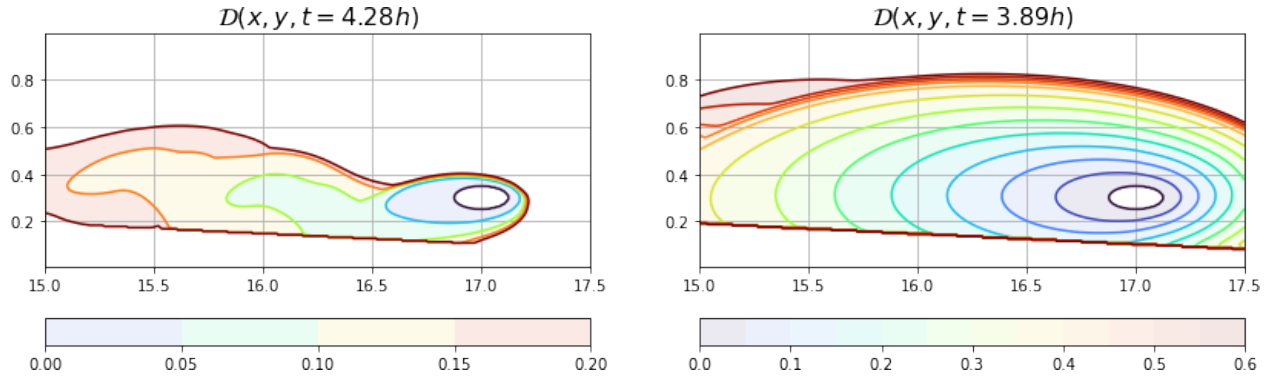
Figure 3.7: Duration maps under the bottom gravity flow after (left) and before (right) the current enters the domain. The units of x and y are in km, and the unit for time is hours.

Applications of multi-time reachability to dynamic ocean environments can be found in [205].

3.6   Conclusions

We obtained the governing equations for reachability over multiple start and terminal times all at once, for systems operating in time-varying environments with dynamic obstacles and any other relevant dynamic fields. We verified results analytically for a moving target and obstacle problem, then applied multi-time reachability to an extended dynamic Dubin's car, and finally showcased the method in a bottom gravity current system. Results highlight the novel capabilities of exact multi-time reachability in dynamic environments. Future work include stochastic effects, adaptive control, data assimilation, learning, and multi-time flow maps [98].

Chapter 4

Split GMM Schemes for Coupled Multi-timescale Dynamical Systems: Application to Lagrangian Data Assimilation[1]

4.1 Introduction

Data assimilation (DA) refers to a set of numerical methods that integrate numerical models and observed data to obtain improved estimates of the underlying state variables. DA is especially crucial, and thus ubiquitous, in geosciences for accurately predicting complex and dynamic Earth systems [21].

In geophysical applications, a common configuration involves coupled systems operating across multiple timescales. In such configurations, the primary system typically pertains to fluid dynamics, encompassing variables like flow velocities, temperature, salinity, and density, while the secondary system models dependent variables such as pollutant densities

---
[1]This chapter is based on [38].

or nutrient fields, whose dynamics are intrinsically linked to the state of the primary system. The objective in such a setup is to achieve simultaneous state estimation for both primary and secondary state variables, leveraging observations from either or both systems.

One specific example of such a coupled system is Lagrangian data assimilation (LaDA), where the secondary system is the dynamics of Lagrangian drifters in the ocean. With the widespread use of Lagrangian instruments, such as floats and drifters [139, 140], the field of LaDA has gained a lot of attention over the last three decades.

Early approaches for LaDA primarily focused on estimating Eulerian measurements from Lagrangian data for assimilation using established methods of Eulerian data assimilation [74, 82, 149, 213]. The main disadvantages of this method is that (a) it ignores that the underlying measurements are related to each other and come from a single trajectory and (b) extra assumptions are made when estimating the Eulerian fields from the Lagrangian data.

As a result, a new, more robust, class of methods where the Eulerian and Lagrangian dynamics and state spaces are augmented were developed [79, 105, 178]. Here, assimilation in the augmented state space is performed using Kalman-like methods. These methods were an improvement over the earlier methods, and converged when the assimilation time interval was at the order of the Lagrangian autocorrelation timescale [32]. While they were a significant improvement, these methods suffered from filter divergence issues [105] especially when the assimilated trajectories passed through saddle points and when the assimilation interval was increased beyond the Lagrangian autocorrelation timescale.

The key underlying reason for this divergence is the highly chaotic and nonlinear nature of the passive Lagrangian advection equation. There are two primary methods for representing the movement of passive tracers within a fluid: the Lagrangian and Eulerian approaches. The Lagrangian method focuses on tracking individual tracer particles over time, whereas the Eulerian approach calculates the spatial flow map, which maps tracer positions between two points in time. Despite both methods capturing equivalent information, the representation

of trajectories through Lagrangian positions rather than a spatial field leads to significant differences. Specifically, a minor change in the initial position of a Lagrangian drifter can result in a substantial alteration in its subsequent path and state. This effect manifests as steep spatial gradients in the Eulerian flow map. Consequently, a filter operating in the Lagrangian state space must effectively manage greater non-linearity and deviation from a normal distribution, while an Eulerian space filter needs to accommodate the increased complexity arising from field-based representation. This is important to note because we don't expect the velocity fields to be as nonlinear and as non-Gaussian as the tracer positions despite also undergoing advection itself (using a dynamical equation analogous to that of the flow map [98]) because of this Eulerian representation. Indeed, dynamical studies of tracer advection [52, 69, 100] show the existence of hyperbolic points in even simple flows. When trajectories pass close to these points, the exponential stretching nature of the localized dynamics gives rise to a highly non-Gaussian pdf for the Lagrangian dynamics. Because of this, Kalman-like methods which assume locally linear dynamics and Gaussian pdfs tend to fail. While Eulerian dynamics are also nonlinear, the fact that even simple flows can give rise to extremely chaotic Lagrangian systems results in the typical methods being used for nonlinear Eulerian assimilation fail for Lagrangian data assimilation.

This gave rise to a new set of methods which used alternatives to Kalman-like filters of assimilation of the Lagrangian state. Apte et al. [4] used Markov chain Monte Carlo (MCMC) methods – which are known to be very effective in low dimensional non-Gaussian settings – for assimilation of the Lagrangian state. However, they become computationally intractable when computing joint Lagrangian-Eulerian posteriors due to the high-dimensional Eulerian state space. Salman [177] proposed a hybrid scheme where the marginal Eulerian state space was assimilated using a particle filter (PF) and the conditional pdf in the Lagrangian state space was computed on a grid by solving the Fokker-Planck equation. Solving the Fokker-Planck is expensive [146] and the high dimensionality of the Eulerian state space makes the PF approach susceptible to probability collapse. Slivinski et al. [188] proposed another

hybrid approach where the Eulerian system is assimilated with a Kalman-like filter and the Lagrangian system is assimilated with a PF like system.

We propose a novel filtering algorithm that is based on a GMM filter [10] in a reduced state space [131, 189]. The primary advantage of the GMM-DO filter is that it allows us to (a) capture the non-Gaussian pdfs and (b) work with the high-dimensional Eulerian system that is commonly low-rank for adaptive subspace [114]. It is worth noting that the two approximate extremes of the GMM filter, with one component and with as many components as ensemble members, reduce to a square-root ensemble Kalman filter (EnKF) [123, 195] and a PF respectively. Our proposed algorithm also uses a split scheme where the Eulerian assimilation is performed using a PF-like reweighting approach whereas the Lagrangian assimilation is performed by resampling at every step. This approach, like the other hybrid methods mentioned, is similar in idea to that of the Rao-Blackwellized particle filters (RBPF) [155] with some key differences which we will elaborate on in Section 4.4.3.

Our proposed method uses the fact that the Lagrangian autocorrelation timescale is much lower and the Lagrangian dynamics much more chaotic than the Eulerian counterpart to implicitly allow for a different resampling frequency for the two systems. Since the Eulerian system is much more computationally expensive than the associated Lagrangian system, resampling the Eulerian variables with a higher assimilation timescale gives us significant computational savings. This third improvement our framework gives us is the ability to use a higher number of Lagrangian ensemble members than the higher-dimensional Eulerian counterpart to allow for a more robust description of the non-Gaussian features without substantially increasing the underlying computational cost.

While this paper focuses on LaDA, it is important to note that our proposed methods are generally applicable to one-way coupled dynamical systems, especially those with differences in timescales, nonlinearity, computational costs, assimilation frequencies, or ensemble size requirements. Such systems can generally be modeled as one-way coupled, wherein the secondary system is influenced by the primary system, but the influence of the secondary

system on the primary is negligible. Examples specific to geosciences include coupled systems where the primary system solves for the ocean state (velocities, salinity, density, etc., as before and the secondary system governs biological fields in the ocean [175], fields of plastic pollutants or other debris [125], etc.

The rest of the paper is organized as follows. Section 4.2 gives the mathematical background for the methods used in our framework. Section 4.3 defines the rigorous problem statement we are trying to solve. Section 4.4 describes our proposed filtering method in detail. We present our numerical results in section 4.5 and provide concluding remarks and avenues for future improvement in section 4.6.

4.2 Review of Relevant Work

In this section, we will go through some relevant filtering methods and the mathematical framework for them. Our proposed methodology will build upon this work.

The sequential approach to data assimilation in filtering problems can be formalized as follows: Given a state space represented by $\boldsymbol{x}$, with dynamics defined by $\dot{\boldsymbol{x}} = f(\boldsymbol{x}; \omega)$ where f is the dynamical model and ω a stochastic event, and an observation model expressed as $\boldsymbol{y}_i \sim \mathcal{N}\left(\mathcal{H}_i(\boldsymbol{x}_i); \Sigma_i\right)$ where $\mathcal{H}_i$ is the observation operator and Σ_i the covariance for the observations, the objective is to iteratively compute the conditional state estimate $\boldsymbol{x}_{i+1}$ given $\boldsymbol{x}_i$ and all prior observations $\boldsymbol{y}_{1 \cdots i+1}$. This formulation encapsulates the core of sequential data assimilation, where each state update integrates new observational data to refine the state estimate progressively.

The Kalman filter [87] comprises a set of analytical equations specifically designed for filtering scenarios where the system dynamics are linear and the state variables follow Gaussian distributions. To extend the Kalman filter's applicability to non-linear systems, various adaptations have been developed. These adaptations typically involve representing the underlying distribution with an ensemble of state estimates and linearizing the non-linear

dynamics [59]. These adaptations, such as the ensemble [49], extended [172], and unscented [203] Kalman filters are particularly effective for systems with quasi-linear dynamics and in high-dimensional state spaces. They enable the formulation of update equations that approximate the Kalman filter's performance even when its foundational assumptions are not strictly met.

The particle filter [36, 201], in contrast, conceptualizes the distribution of the state space as a collection of weighted Dirac delta functions located at the positions of each ensemble member. Utilizing principles of importance sampling theory, the filter recalculates the weights of these ensemble members at each assimilation step. This approach is markedly effective in scenarios where the system exhibits highly non-linear dynamics and the state space distributions are notably non-Gaussian. The Particle filter's strength lies particularly in low-dimensional state spaces, where its discrete representation of the distribution can capture complex, non-linear relationships more effectively than methods assuming Gaussianity.

A more recent development, the GMM-DO filter, considers dynamical systems where (a) the state space is high dimensional, but assumed well approximated by a dynamic reduced space, i.e., a low-rank space that is dynamic, such that it can be well represented as

$$\boldsymbol{x}(t, \omega) = \bar{\boldsymbol{x}}(t) + \sum_{m=1}^{r} \tilde{\boldsymbol{x}}_m(t) \Phi_m(t; \omega) \tag{4.1}$$

and (b) the stochastic variables in the reduced state space $(\Phi_m(t; \omega))$ can be well approximated by a pdf given by a GMM. At every assimilation step, a GMM distribution is fit to the prior ensemble of coefficients $\Phi_m^{(r)}(t)$ using the expectaion-maximization (EM) algorithm

$$\Phi_m^{(f)}(t; \omega) \sim GMM^{(f)}(\boldsymbol{\pi}^{(f)}, \boldsymbol{\mu}^{(f)}, \boldsymbol{\Sigma}^{(f)}) \tag{4.2}$$

The posterior distribution is then analytically computed under the observations

$$\Phi_m^{(a)}(t; \omega) \sim GMM^{(a)}(\boldsymbol{\pi}^{(a)}, \boldsymbol{\mu}^{(a)}, \boldsymbol{\Sigma}^{(a)}) \tag{4.3}$$

The equations to compute these can be derived by following the Bayes' law and are detailed in Sondergaard and Lermusiaux [189].

The GMM-DO filter is especially useful for Lagrangian systems because it can handle both non-Gaussian pdfs, due to chaotic Lagrangian dynamics, and high dimensional, low rank state spaces due to gridded representation of the Eulerian data. As a result, we build upon the GMM-DO filter and introduce modifications to allow different resampling frequencies for the Lagrangian and Eulerian dynamics. In the following sections, we delve into a rigorous mathematical description of the problem statement and detail our proposed method.

4.3 Problem Statement

Consider a one-way coupled stochastic dynamical system

$$\dot{\boldsymbol{x}}_{\boldsymbol{\mathcal{E}}} = \boldsymbol{f}_{\boldsymbol{\mathcal{E}}}(\boldsymbol{x}_{\boldsymbol{\mathcal{E}}}, t; \omega) \qquad\qquad \text{Primary system} \qquad\qquad (4.4a)$$

$$\dot{\boldsymbol{x}}_{\boldsymbol{\ell}} = \boldsymbol{f}_{\boldsymbol{\ell}}(\boldsymbol{x}_{\boldsymbol{\ell}}, \boldsymbol{x}_{\boldsymbol{\ell}}, t; \omega) \qquad\qquad \text{Coupled system} \qquad\qquad (4.4b)$$

These stochastic differential equations (SDEs) are accompanied by their corresponding initial and boundary conditions. As a consequence of the one-way coupling, the trajectories/solutions of the primary system $\boldsymbol{x}_{\boldsymbol{\mathcal{E}}}(t)$ are independent of the trajectories/solutions of the coupled system $\boldsymbol{x}_{\boldsymbol{\ell}}(t)$. Consider the observation operator

$$\boldsymbol{y}_{\boldsymbol{\ell}}(t_k) \sim \mathcal{N}\left(\mathcal{H}\left(\boldsymbol{x}_{\boldsymbol{\mathcal{E}}}(t_k), \boldsymbol{x}_{\boldsymbol{\ell}}(t_k)\right); \Sigma_{\text{obs}}\right) \qquad\qquad (4.5)$$

where t_k are the observation times. We assume $\mathcal{H}$ to be a linear operator in the combined Lagrangian and Eulerian spaces, capable of handling measurements that are either purely Eulerian, purely Lagrangian, or a combination of both being observed simultaneously. Since the focus of the paper in on LaDA, we specifically focus on examples where the observations are purely Lagrangian. We also note that, practically, we often obtain observations taken at

multiple different times at once. In such cases, the observations are assimilated sequentially, each at its respective time.

We wish to obtain a filtering scheme to estimate the joint probability distribution of state given past observations

$$\rho\left(\boldsymbol{x}_{\boldsymbol{\mathcal{E}}}(t), \boldsymbol{x}_{\boldsymbol{\ell}}(t) \middle| \{\boldsymbol{y}_{\boldsymbol{\ell}}(t_k) \quad \forall t_k \leq t\}\right) \tag{4.6}$$

Specifically, we consider the case of Lagrangian data assimilation, where the primary system corresponds to the Eulerian state and the coupled system corresponds to the Lagrangian state. In this context, $\boldsymbol{x}_{\boldsymbol{\mathcal{E}}}$ represents the Eulerian state variable describing the fluid flow. This includes spatiotemporal fields for the flow velocity, temperature, density, humidity or salinity, and other relevant state variables governed by the Eulerian dynamical model, denoted by $\boldsymbol{f}_{\boldsymbol{\mathcal{E}}}$. This model $\boldsymbol{f}_{\boldsymbol{\mathcal{E}}}$ can take various forms, including the Navier-Stokes equations for classic fluid dynamics, or the primitive equations with temperature, salinity, humidity, and other variables for classic ocean or atmospheric applications. In some cases, other approximations such as shallow water equations might be employed, tailored to the particular requirements of the system being studied.

The Lagrangian state variables, denoted by $\boldsymbol{x}_{\boldsymbol{\ell}}$, represent positions and measurements of drifters advected by the fluid flow. The Lagrangian model, $\boldsymbol{f}_{\boldsymbol{\ell}}$, describes this advection. In its simplest form, $\boldsymbol{f}_{\boldsymbol{\ell}}$ may embody a passive drifter trajectory flow equation, asserting that the drifter's velocity equals that of the fluid at its location, supplemented by a Brownian noise term to accommodate subgrid velocity scales not captured by the Eulerian fluid model. Additional modeling options include windage terms, considerations for inertia, and tidal effects.

The system under consideration (Eqs 4.4) exhibits several notable properties:

1. The computation of $\boldsymbol{f}_{\boldsymbol{\mathcal{E}}}$ is computationally expensive, making frequent assimilation and restarts impractical at a high assimilation frequency.

2. $\boldsymbol{f}_{\boldsymbol{\ell}}$ is a highly chaotic dynamical system, necessitating frequent assimilation and resam-

pling to prevent rapid filter divergence.

3. Due to the grid-based description of the Eulerian system, $x_{\mathcal{E}}$ is of extremely high dimensionality. However, strong spatial correlations contribute to a reduced effective rank.

4. The true space occupied by $x_{\mathcal{E}}$ is physically constrained, for instance, in fluid simulations involving non-divergent flow. Designing resampling-based assimilation schemes that guarantee resampled points adhere to physical constraints is challenging. Consequently, frequent resampling of $x_{\mathcal{E}}$ may lead to the filter producing a non-physical pdf.

5. Importantly, the solution for $x_{\mathcal{E}}$ remains independent of x_{ℓ}, indicating a one-way coupling.

The goal of this work is to develop a Bayesian assimilation scheme for one-way coupled systems that leverages these properties.

4.4 Bayesian DA for One-way Coupled Dynamical Systems

Our filtering algorithm is designed to exploit the distinctive characteristics of Eulerian(slow) and Lagrangian(fast) frameworks, as outlined in Section 4.3. Our objective is to establish a comprehensive filtering approach that: (1) accommodates the highly non-Gaussian pdfs inherent in the chaotic fast system and manages the expansive state space of the slow system; and (2) implements a more frequent resampling and a larger ensemble for the more chaotic fast dynamics, in contrast to a less frequent resampling and smaller ensemble for the computationally demanding state variables of the slow system.

To address the varying timescales of these variables, we propose segregating the joint

posterior distribution of the coupled system, as delineated in Equation 4.4:

$$\underbrace{\rho(\boldsymbol{x_\varepsilon}(t_k), \boldsymbol{x_\ell}(t_k) | \boldsymbol{y_{\ell 1 \cdots k}})}_{\substack{\text{Joint} \\ \text{Posterior}}} = \qquad (4.7)$$

$$\underbrace{\rho(\boldsymbol{x_\ell}(t_k) | \boldsymbol{x_\varepsilon}(t_k), \boldsymbol{y_{\ell 1 \cdots k}})}_{\substack{\text{Conditional} \\ \text{Posterior}}} \underbrace{\rho(\boldsymbol{x_\varepsilon}(t_k) | \boldsymbol{y_{\ell 1 \cdots k}})}_{\substack{\text{Marginal} \\ \text{Posterior}}}$$

This decomposition enables us to differentiate between the fast and slow states' attributes, recognizing the high dimensionality and statistical richness of the distribution of the slow states, and the lower dimensionality yet greater statistical richness of the distribution of the fast states. This framework facilitates the propagation of both states, respecting their chaotic dynamics and computational demands.

The marginal posterior $\rho(\boldsymbol{x_\varepsilon}(t_k) | \boldsymbol{y_{\ell 1 \cdots k}})$ is represented through samples and weights, utilizing particle filtering and importance sampling techniques:

$$\boldsymbol{x_{\varepsilon(i)}}(t_k) \sim \rho(\boldsymbol{x_\varepsilon}(t_k)) \qquad (4.8)$$

$$w_{(i)}(t_k) = \frac{\rho(\boldsymbol{x_{\varepsilon(i)}}(t_k) | \boldsymbol{y_{\ell 1 \cdots k}})}{\rho(\boldsymbol{x_{\varepsilon(i)}}(t_k))} \qquad (4.9)$$

Conversely, we can represent the conditional posterior of the fast system, $\rho(\boldsymbol{x_\ell}(t_k) | \boldsymbol{x_\varepsilon}(t_k), \boldsymbol{y_{\ell 1 \cdots k}})$, by samples

$$\boldsymbol{x_{\ell(i,j)}}(t_k) \sim \rho(\boldsymbol{x_\ell}(t_k) | \boldsymbol{x_{\varepsilon(i)}}(t_k), \boldsymbol{y_{\ell 1 \cdots k}}) \qquad (4.10)$$

This allows us to have multiple ensemble members of the fast system for every given ensemble member of the slow system, thus enabling us to capture the more chaotic dynamics of the fast system.

Given this split of the posterior, we can perform the forecast step, which involves com-

70

puting

$$\underbrace{\rho(\boldsymbol{x_{\mathcal{E}}}(t_{k+1}), \boldsymbol{x_{\ell}}(t_{k+1})|\boldsymbol{y_{\ell}}_{1\dots k})}_{\substack{\text{Joint} \\ \text{Forecast}}} = \qquad\qquad (4.11)$$

$$\underbrace{\rho(\boldsymbol{x_{\ell}}(t_{k+1})|\boldsymbol{x_{\mathcal{E}}}(t_{k+1}), \boldsymbol{y_{\ell}}_{1\dots k})}_{\substack{\text{Conditional} \\ \text{Forecast}}} \underbrace{\rho(\boldsymbol{x_{\mathcal{E}}}(t_{k+1})|\boldsymbol{y_{\ell}}_{1\dots k})}_{\substack{\text{Marginal} \\ \text{Forecast}}}$$

As before, we can represent the marginal forecast using the particle filtering approach by solving for ensemble members $\boldsymbol{x_{\mathcal{E}(i)}}(t_{k+1})$ by propagating the members in equation 4.8 through the slow dynamics and maintaining the weights described in Equation 4.9. The key idea is that since the slow samples are sampled from the prior, they can be pre-computed and don't need to be resampled/forecasted every time there is an assimilation step. The only quantity that changes is the associated weight.

The forecast of the fast system on the other hand involves propagating the *resampled* ensemble members from equation 4.10 through the fast model with the associated pre-computed ensemble members of the slow system. Since the members are sampled based on a distribution that is conditioned on the observations, this resampling step has to be done at every assimilation step.

Building on this conceptual foundation, we now present the filtering algorithm in detail.

4.4.1 Algorithm

Initialization

Initialization involves drawing ensembles that respect the initial conditions. We first draw the ensembles for the flow variables $\boldsymbol{x_{\mathcal{E}(i)}}(t_0)$, where $i = 1 \dots N_{\mathcal{E}}$, from the initial marginal pdf $\rho_{\epsilon,0}(\boldsymbol{x_{\mathcal{E}}})$. We then draw an ensemble of Lagrangian variables $\boldsymbol{x_{\ell(i,j)}}(t_0)$, where $j = 1 \dots N_{\ell}$, for every Eulerian ensemble member $\boldsymbol{x_{\mathcal{E}(i)}}(t_0)$ from the conditional distribution $\rho_{\ell|\epsilon,0}(\boldsymbol{x_{\ell}}|\boldsymbol{x_{\mathcal{E}}} = \boldsymbol{x_{\mathcal{E}(i)}}(t_0))$. This gives us a total of $N_{\mathcal{E}} \times N_{\ell}$ Lagrangian state variables.

Finally, we define weights corresponding to every Eulerian ensemble member $w_i = \frac{1}{N_{\mathcal{E}}}$, where $i = 1 \ldots N_{\mathcal{E}}$.

Data Assimilation Loop

We now describe the data assimilation loop. The first observation has the index $k = 1$ and is due to arrive at t_k. We start with the current time $t_c = t_{k-1} = t_0$

Eulerian Forecast: The first step is to use a stochastic numerical solver to obtain the forecast $\boldsymbol{x}_{\mathcal{E}(i)}(t)$, $\forall t \in [t_c, T]$, for the newly sampled Eulerian ensembles $\boldsymbol{x}_{\mathcal{E}(i)}(t_c)$. A good choice for T is time till which we can solve the system in the wallclock time $t_k - t_c$ until the next observation arrives. A good choice for a numeric stochastic solver for the typically high dimensional Eulerian system is the dynamically orthogonal (DO) solver [180, 181] which allows one to solve the dynamics in a reduced space, as given by equation 4.1. If one were to use a full rank method like the Monte-Carlo approach instead, it would be recommended to perform a KL decomposition [182] to obtain a reduced state space representation if the Eulerian state space is high dimensional.

Lagrangian Forecast: The next step is to use the stochastic numerical solver to obtain the forecast $\boldsymbol{x}_{\ell(i,j)}(t)$, $\forall t \in [t_c, t_k]$. That is, we will be forecasting the Lagrangian system until the next Lagrangian observation for *all available* Lagrangian ensemble members $\boldsymbol{x}_{\ell(i,j)}(t_c)$.

Obtaining joint prior at t_k: We now assemble the joint ensembles

$$\begin{bmatrix} \boldsymbol{x}_{\mathcal{E},(i)}(t_k) \\ \boldsymbol{x}_{\ell,(i,j)}(t_k) \end{bmatrix} \forall i = 1 \ldots N_{\mathcal{E}}, j = 1 \ldots N_{\ell}$$

. If using a DO representation, one would use the coefficients $\Phi_{(i)}$ instead of the full rank representation $\boldsymbol{x}_{\mathcal{E}i,}$. We will now fit a Gaussian Mixture Model to this set of ensembles using the (weighted) EM algorithm (with the BIC criterion) to get an approximate distribution of

our joint prior. Let this distribution be $\text{GMM}^{\text{f}}_{\text{t}_\text{k}}(\boldsymbol{x}_{\boldsymbol{\mathcal{E}}}, \boldsymbol{x}_{\boldsymbol{\ell}}) = \text{GMM}_{\text{t}_\text{k}}(\boldsymbol{x}_{\boldsymbol{\mathcal{E}}}, \boldsymbol{x}_{\boldsymbol{\ell}}; \boldsymbol{\pi}^{\text{f}}, \boldsymbol{\mu}^{\text{f}}, \Sigma^{\text{f}})$. The weighted EM algorithm is described in Appendix A.1. Figure 4.1a illustrates this step for a simplified system with one Eulerian and one Lagrangian dimension each. We note that for every Eulerian ensemble member, there are multiple Lagrangian ensemble members (denoted by the semi-transparent points on the plot). The fitted GMM consists of three components represented by the three ellipses. The contour plot represents the pdf values in the joint state space and the plots to the edge are the marginal pdfs of both the Eulerian and Lagrangian state spaces.

Computing the posterior: Due to conjugacy properties of GMMs under linear Gaussian observation models, we can compute the analytical posterior GMM for the joint model using the Bayes law [189]. Let this distribution be

$$\rho^a_{\ell,\epsilon|\boldsymbol{y}_{\boldsymbol{\ell}}(t_k)}(\boldsymbol{x}_{\boldsymbol{\mathcal{E}}}, \boldsymbol{x}_{\boldsymbol{\ell}})) = \text{GMM}^{\text{a}}_{\text{t}_\text{k}}(\boldsymbol{x}_{\boldsymbol{\mathcal{E}}}, \boldsymbol{x}_{\boldsymbol{\ell}}) \tag{4.12}$$

$$= \text{GMM}_{\text{t}_\text{k}}(\boldsymbol{x}_{\boldsymbol{\mathcal{E}}}, \boldsymbol{x}_{\boldsymbol{\ell}}; \boldsymbol{\pi}^{\text{a}}, \boldsymbol{\mu}^{\text{a}}, \Sigma^{\text{a}}). \tag{4.13}$$

Figure 4.1b illustrates this posterior for the simplified system with the associated posterior marginals.

Re-weighting Eulerian ensemble: We will now use the posterior and the prior distributions to obtain the new weights of the particles. We first compute the marginal GMMs in just the Eulerian space (Details in Appendix A.3): $\text{GMM}^{\text{f}}_{\mathcal{E}}$ and $\text{GMM}^{\text{a}}_{\mathcal{E}}$. That is, we integrate out the Lagrangian variables. We define the new weights as follows

$$w_i \leftarrow w_i \frac{\text{GMM}^{\text{a}}_{\mathcal{E}}(\boldsymbol{x}_{\boldsymbol{\mathcal{E}},(i)})}{\text{GMM}^{\text{f}}_{\mathcal{E}}(\boldsymbol{x}_{\boldsymbol{\mathcal{E}},(i)})} \,, \quad \forall i = 1 \ldots N_{\mathcal{E}} \tag{4.14}$$

The new weighted ensembles of Eulerian simulations now represent the posterior distribution and are conditioned on the observations at t_{i_ℓ}. This step is further illustrated in Figure 4.1c.

The ratio of the posterior to the prior is the update factor in the weights. We specifically follow three Eulerian ensemble members given by $\boldsymbol{x}_{\mathcal{E}} = \{-1, 0, 1\}$ indicated by the brown dotted vertical lines in the various plots. The updated thickness of the lines in Figure 4.1c represents the updated weights. The members more likely to show up in the posterior distribution than the prior are weighted higher and the ones less likely to show up are weighted lower. This step is essentially an importance sampling step with the sampling distribution being the prior marginal GMM and the target distribution being the posterior marginal GMM. Statistics of the Eulerian sample computed using these weights represent statistics of the posterior computed with a effective sample size (ESS) given by

$$\text{ESS} = \frac{(\Sigma_i w_i)^2}{\Sigma_i w_i^2} \tag{4.15}$$

If the posterior pdf is close to the prior pdf, the prior ensemble will be a good representation of the true distribution and the ESS will be close to the number of Eulerian ensemble members. On the other hand, if the pdfs are significantly different, the ESS will be much lower. The concept of ESS is commonly used in PFs to make decisions on resampling [20]. A high value of ESS is a signal that resampling the Eulerian ensemble isn't necessary at this timestep and for the next timestep, we can use the same reweighted ensemble that we have solved for. A very low value of ESS is a signal that the quality of this ensemble is poor and it should be discarded and a resampled ensemble should be used for the next timestep.

(Optional) Resampling the Eulerian ensemble: Based on the value of the ESS, one can decide to either (a) not resample the Eulerian variables at all (b) discard the reweighted ensemble and resample both the Eulerian and Lagrangian state variables or (c) keep the reweighted ensemble and additionally resample the Eulerian and Lagrangian state variables and use both set of ensembles together for assimilation at future timesteps.

Resampling is done by drawing from the posterior Eulerian marginal computed from the

joint posterior (Eq. 4.12)

$$\boldsymbol{x}_{\boldsymbol{\mathcal{E}},(\boldsymbol{i})}(t_k) \sim \text{GMM}^{\text{a}}_{\epsilon,\text{t}_\text{k}}(\boldsymbol{x}_{\boldsymbol{\mathcal{E}}}) \tag{4.16}$$

Resampling the Lagrangian ensemble: Irrespective of whether we decide to just reweight, resample or use a combination for Eulerian ensembles in the previous step, we will always resample the Lagrangian ensemble. We first analytically compute the conditional posterior distributions $\text{GMM}^{\text{a}}_{\ell|\mathcal{E}}$ (Details in Appendix A.2). That is, the posterior Lagrangian distribution given the Eulerian state. For every Eulerian member i, we resample the corresponding Lagrangian states from this posterior conditional GMM.

$$\boldsymbol{x}_{\boldsymbol{\ell},(\boldsymbol{i},\boldsymbol{j})}{}^{a}(t_{i_\ell}) \sim \text{GMM}^{\text{a}}_{\ell|\mathcal{E}}(\boldsymbol{x}_{\boldsymbol{\ell}}; \boldsymbol{x}_{\boldsymbol{\mathcal{E}}} = \boldsymbol{x}_{\boldsymbol{\mathcal{E}},\boldsymbol{i}}) \tag{4.17}$$

This is illustrated in Figure 4.1d for the three Eulerian ensembles mentioned before. The prior and posterior densities plotted are the slices of the joint pdf at the three Eulerian ensemble values respectively. The blue scatterpoints at the bottom are the various Lagrangian prior ensemble members for the given Eulerian ensemble, $\boldsymbol{x}_{\boldsymbol{\ell}(i,j)}{}^{f}$, and the orange points are the resampled Lagrangian points, $\boldsymbol{x}_{\boldsymbol{\ell}(i,j)}{}^{a}$.

Looping: Finally we loop. We set $t_c = t_k$ and $k \leftarrow k+1$. The key things to keep in mind as we loop are (i) We would compute a new Eulerian forecast only if we resampled newer Eulerian ensemble members in this assimilation step. Otherwise, previously reweighted Eulerian simulations still hold and we can skip the Eulerian forecast altogether. (ii) We will be forecasting *all* active (not discarded) Lagrangian ensembles at *every* Lagrangian assimilation step. If we choose to keep multiple ensemble members active during this assimilation step, we will compute the Lagrangian forecast for *all* of them. (iii) When computing the joint prior, we can have multiple weighted ensemble sets at the time of interest. We will use all of them to fit the prior. (iv) The computation of the posterior remains unchanged (v)

When reweighting the Eulerian ensembles, the multiplicative step ensures that the weights are consistent over multiple reweighting steps.

The overall method is summarized in algorithm box 1

Algorithm 1: Method summary

Input: Numerical stochastic solvers for $f_{\mathcal{E}}(\cdot)$ and $f_\ell(\cdot)$. Initial and boundary conditions for the dynamical systems at t_0. Observation operator $\mathcal{H}(\cdot, \cdot)$ as defined in equations (4.4) and (4.5)

Data: Observations $\boldsymbol{y}_\ell(t_k)$ for observation times $t_1 \ldots t_N$

Result: Filtered joint state distribution functions $\boldsymbol{x}_{\mathcal{E}}(t_k), \boldsymbol{x}_\ell(t_k) | \boldsymbol{y}_\ell(t_1) \ldots \boldsymbol{y}_\ell(t_k)$

Initialization:

    Obtain ensembles of the Eulerian state from the marginal IC for $\boldsymbol{x}_{\mathcal{E}}$:

    $\boldsymbol{x}_{\mathcal{E}(i)}(t_0) \quad i = 1 \ldots N_{\mathcal{E}}$;

    Initialize the weights corresponding to the Eulerian states $w_i = \frac{1}{N_{\mathcal{E}}}$ Obtain ensembles of the Lagrangian state from the conditional IC for $\boldsymbol{x}_\ell | \boldsymbol{x}_{\mathcal{E}(i)}$:

    $\boldsymbol{x}_{\ell(i,j)}(t_0) \quad j = 1 \ldots N_\ell$;

for $k = 1$ *to* N **do**

    For newly sampled Eulerian ensembles, generate a forecast state estimate for the base dynamical system $\boldsymbol{x}_{\mathcal{E}(i)}(t_{k'}) \quad \forall k' = k \ldots N, i = 1 \ldots N_{\mathcal{E}}$;

    Generate a forecast state estimate $\boldsymbol{x}_{\ell(i,j)}(t_k)$ using the Lagrangian model for *all* existing Lagrangian ensemble members;

    Fit a GMM with parameters π_f, μ_f, Σ_f using EM to the set of joint weightd ensembles $\boldsymbol{x}_{\mathcal{E}(i)}, \boldsymbol{x}_{\ell(i,j)}$ with weights w_i;

    Compute the posterior GMM(π_a, μ_a, Σ_a) using Bayes' law;

    Compute the marginal distributions for $\boldsymbol{x}_{\mathcal{E}}(t_k)$. Update weights with ratio of likelihoods given in equation 4.14 for all members $\boldsymbol{x}_{\mathcal{E}(i)}(t_k)$.;

    Use the updated weights to compute the ESS for each sets of ensembles launched using Equation 4.15;

    (Optional) Using the ESS values, discard certain sets of ensembles if their ESS is below a predecided threshold.;

    (Optional) Using the total ESS from currently active sets of Eulerian ensembles, resample a new set of Eulerian ensembles with unitary weights from the marginal posterior GMM to ensure that the total ESS is above a given threshold.;

    Compute the conditional distribution and resample the Lagrangian ensemble members from these conditionals $\boldsymbol{x}_{\ell(i,j)}(t_k) \sim \boldsymbol{x}_\ell(t_k) | \left(\boldsymbol{x}_{\mathcal{E}}(t_k) = \boldsymbol{x}_{\mathcal{E}(i)}(t_k) \right)$.;

4.4.2 Proof of Consistency

We want to prove that re-weighting the Eulerian ensemble and resampling the Lagrangian conditional ensembles gives us an accurate distribution for the posterior according to Bayes' law.

To prove this, we show that the weighted expected value of an arbitrary function of the posterior ensembles is equal to the expected value of the function under the true posterior.

Let $h(\boldsymbol{x_\mathcal{E}}, \boldsymbol{x_\ell})$ be the arbitrary function in question. We wish to compute the expected value of this function under the posterior

$$\mathbb{E}_{\rho^a}\left(h(\boldsymbol{x_\mathcal{E}}, \boldsymbol{x_\ell})\right)$$

$$= \int h(\boldsymbol{x_\mathcal{E}}, \boldsymbol{x_\ell})\rho^a(\boldsymbol{x_\mathcal{E}}, \boldsymbol{x_\ell})\mathrm{d}\boldsymbol{x_\mathcal{E}}\mathrm{d}\boldsymbol{x_\ell}$$

$$= \int h(\boldsymbol{x_\mathcal{E}}, \boldsymbol{x_\ell})\rho^a(\boldsymbol{x_\ell}|\boldsymbol{x_\mathcal{E}})\rho^a(\boldsymbol{x_\mathcal{E}})\mathrm{d}\boldsymbol{x_\mathcal{E}}\mathrm{d}\boldsymbol{x_\ell}$$

$$= \int \underbrace{\frac{\rho^a(\boldsymbol{x_\mathcal{E}})}{\rho^f(\boldsymbol{x_\mathcal{E}})}}_{\text{Weights}} h(\boldsymbol{x_\mathcal{E}}, \boldsymbol{x_\ell}) \underbrace{\rho^a(\boldsymbol{x_\ell}|\boldsymbol{x_\mathcal{E}})\rho^f(\boldsymbol{x_\mathcal{E}})}_{\substack{\text{Weighted ensemble}\\\text{distribution}}} \mathrm{d}\boldsymbol{x_\mathcal{E}}\mathrm{d}\boldsymbol{x_\ell}$$

We note that the drawing from the distribution $\rho^a(\boldsymbol{x_\ell}|\boldsymbol{x_\mathcal{E}})\rho^f(\boldsymbol{x_\mathcal{E}})$ is equivalent to drawing the Eulerian state variable from the prior and drawing the Lagrangian state variable from the conditional posterior. This is exactly the distributions our ensembles live in. Since we do not resample the Eulerian variables, they are drawn from the prior distribution. The resampled Lagrangian variables on the other hand, are drawn from the conditional posterior.

$$\mathbb{E}_{\rho^a(\boldsymbol{x_\mathcal{E}}, \boldsymbol{x_\ell})}\left(h(\boldsymbol{x_\mathcal{E}}, \boldsymbol{x_\ell})\right) =$$

$$\mathbb{E}_{\rho^a(\boldsymbol{x_\ell}|\boldsymbol{x_\mathcal{E}})\rho^f(\boldsymbol{x_\mathcal{E}})}\left(w(\boldsymbol{x_\mathcal{E}})h(\boldsymbol{x_\mathcal{E}}, \boldsymbol{x_\ell})\right)$$

Our assimilation scheme is thus consistent with the true Bayesian posterior.

4.4.3   Comparison to Existing Methods

In this section, we comment on the key similarities and differences between our DA method for coupled systems and other related schemes. In comparison with RBPF-based filters [e.g. 143, 177], the similarity is the hybrid approach where one scheme is used for the marginal posterior of the primary system and another for the conditional posterior of the coupled system (conditioned on the primary system). The key difference is that a pure Particle filter approach is used in these methods for the primary system (as opposed to using GMMs to compute the weights) and the conditional posteriors are computed for each primary ensemble member separately (as opposed to computing a joint posterior all at once). Salman [177] solves the Fokker-Planck equation on a grid to compute these conditional posterior while Majda et al. [143] uses an uncertainty quantification scheme that represents the secondary states conditioned on the primary state as a Gaussian distribution and subsequently uses Kalman filtering to compute the conditional posterior.

A second set of filters that we compare to combine particle filtering ideas and Gaussian filtering ideas but aren't necessarily targeting coupled systems or state spaces. The Gaussian particle fitler(GPF) and the Gaussian sum particle filter (GSPF-1) described in Kotecha and Djuric [94] and Kotecha and Djuric [95] use a method very similar to what we propose in the marginalized probability space for the primary sytsem – where the underlying distributions are assumed to be Gaussian or GMM – but instead of computing the posteriors analytically, weights are computed for ensemble members based on the likelihoods. The key motivation for that approach is to use the weighted members to compute the posterior distribution without having to perform the covariance inversion step. The motivation for our approach, instead, is that we have precomputed the trajectories of these samples and re-weighting them allows us to very quickly get a representation of the distribution at future timesteps without having to solve the dynamical system again. The weighted ensemble Kalman filter [24, 164]

also uses a hybrid approach where the Ensemble Kalman filter is used to obtain a proposal distribution for the PF which is closer to the posterior and hence performs better.

Finally, Slivinski et al. [188] proposes a hybrid assimilation approach specifically for LaDA which uses an EnKF for the Eulerian system and a PF for the Lagrangian system. Like the RBPF-type filters above, assimilation is performed in the marginal and conditional spaces separately. However, since the EnKF results in the Eulerian ensemble members being transformed, the method is no longer consistent as the conditional Lagrangian ensembles no longer map to the same Eulerian ensemble members. Moreover, it is a strong approximate filter with strong performance, as described in Slivinski et al. [188], which can efficiently account for the highly chaotic nature of the Lagrangian dynamics. Another difference to our porposed approach is the fact that transforming the Eulerian ensemble members at every assimilation step means that Eulerian ensemble members need to be solved for with the same assimilation frequency as that of the more chaotic Lagrangian system.

4.5   Numerical Experiments

To demonstrate the application of this novel filtering scheme, we present three numerical experiments. First, we construct a simplified flow such that the dynamics of the flow and the corresponding lagrangian tracer can be represented by a linear system. We validate the performance of our method in this scenario to an exact analytical solution and compare performance with an Ensemble Kalman filtering approache. Second, we demonstrate our method on a multi-timescale Lorenz-95 system, illustrating the applicability of our approach for an arbitrary multi-timescale coupled system. Finally, we demonstrate our algorithm on a more realistic flow where we use the abovementioned DO algorithm to solve for the flow in a reduced space and infer this flow using Lagrangian tracer position measurements.

4.5.1 Validation Case: Linear System

For this first experiment, we assume that the background flow is spatially uniform and the direction of the flow is constantly rotating in time. We represent this flow with a vector $\begin{bmatrix} u \\ v \end{bmatrix}$ and the position of the tracer with another vector $\begin{bmatrix} x \\ y \end{bmatrix}$. The Eulerian and Lagrangian dynamics respectively are given by

$$\frac{\mathrm{d}}{\mathrm{d}t} \begin{bmatrix} u \\ v \end{bmatrix} = \begin{bmatrix} 0 & 1 \\ -1 & 0 \end{bmatrix} \begin{bmatrix} u \\ v \end{bmatrix} \tag{4.18}$$

$$\frac{\mathrm{d}}{\mathrm{d}t} \begin{bmatrix} x \\ y \end{bmatrix} = \begin{bmatrix} 1 & 0 \\ 0 & 1 \end{bmatrix} \begin{bmatrix} u \\ v \end{bmatrix} \tag{4.19}$$

The augmented system is simply

$$\frac{\mathrm{d}}{\mathrm{d}t} \begin{bmatrix} x \\ y \\ u \\ v \end{bmatrix} = \begin{bmatrix} 0 & 0 & 1 & 0 \\ 0 & 0 & 0 & 1 \\ 0 & 0 & 0 & 1 \\ 0 & 0 & -1 & 0 \end{bmatrix} \begin{bmatrix} x \\ y \\ u \\ v \end{bmatrix} \tag{4.20}$$

We set the stochastic prior as independent Gaussians for the four state variables $\begin{bmatrix} x & y & u & v \end{bmatrix}$ with means $\begin{bmatrix} 0.5 & 0.0, 1.0, 0.0 \end{bmatrix}$ and standard deviations $\begin{bmatrix} 2.0 & 2.0 & 1.0 & 1.0 \end{bmatrix}$.

The truth is given by the same system and observation model is given by

$$\boldsymbol{y}_\ell \sim \mathcal{N} \left(\begin{bmatrix} x \\ y \end{bmatrix} ; \begin{bmatrix} 0.1^2 & 0 \\ 0 & 0.1^2 \end{bmatrix} \right) \tag{4.21}$$

The true dynamics and the corresponding observations are given in Figure 4.2.

Given the linearity and the Gaussianity of the systems involved, we can solve for the

true posterior of the joint state analytically using the Kalman filter. To validate, we use our novel filtering method with the following parameters: (a) we set the number of mixtures in the model to 1 since all distributions are Gaussian and (b) we set it up so that the Eulerian ensembles are resampled at every observation timestep and combined with the pre-existing re-weighted Eulerian ensembles from previous timesteps. We compare this to a pure EnKF based approach where we resample the *same* number of Eulerian ensemble members (800) at every step but do not use the reweighting scheme. As a result, if the bottleneck of the system is the Eulerian solve, both approaches have the *same total cost*.

We look at the state estimate of both approaches right before the third observation arrives and compare the mean and variance of our state estimate to that obtained analytically using the Kalman Filter. To compare the two methods and check their consistency, we repeat this experiment a number (100) of times and look at the variance of the estimators of the state mean and variance. The results are plotted in Figure 4.3.

We see that both schemes are consistent and successfully obtain the mean and variance of the state at the given time. However, the variance of these estimators are much lower using the novel scheme due to a greater effective sample size obtained by reweighting and reusing the Eulerian simulations before the first and second assimilation step.

4.5.2   Multi-timescale Lorenz-95

The next dynamical system we look at a version of multiscale Lorenz 95 system[138], which is one-way coupled. The dynamics are given by

$$\frac{\mathrm{d}\boldsymbol{x}_i}{\mathrm{d}t} = \left(\boldsymbol{x}_{i+1} - \boldsymbol{x}_{i-2}\right)\boldsymbol{x}_{i-1} - \boldsymbol{x}_i + F \tag{4.22}$$

$$\frac{\mathrm{d}\boldsymbol{y}_{(i,j)}}{\mathrm{d}t} = -cb\boldsymbol{y}_{(i,j+1)}\left(\boldsymbol{y}_{(i,j+2)} - \boldsymbol{y}_{(i,j-1)}\right) - c\boldsymbol{y}_{(i,j)} + \frac{hc}{b}\boldsymbol{x}_i \tag{4.23}$$

with $b = 5, c = 5, h = 1$.

The 'synoptic' variables, given by $\boldsymbol{x}$, have a slower evolution over time and are supposed

to represent observations on a given Latitude circle. The 'convective' variables have a faster dynamics and vary over smaller timescales[19]. This is a coupled chaotic system where both the slow, and the fast system are chaotic. However, the faster system is *more* chaotic and has a smaller assimilation timescale. This is similar in principle to the case of Lagrangian data assimilation and is a good testcase for our approach. We consider a system with $N_i = 5$ synoptic variables with periodic boundary conditions and observations $\boldsymbol{y}_{(1,1\ldots4)}$. That is, we receive observations only corresponding to the fast system coupled to $\boldsymbol{x}_1$.

The dynamics and the observations corresponding to the true system, which are obtained by simulating with a halved timestep, are given in Figure 4.4. In our assimilation system, we implement an adaptive scheme where several samples of the slower system are resampled to maintain a constant ESS after each assimilation step. The ESS for each ensemble, initiated at different assimilation times, is summarized in Figure 4.5. Each colored region in the figure corresponds to a distinct set of ensemble members launched simultaneously. The height of these colored patches indicates the ESS of the respective ensemble at various assimilation times. Initially, due to a lack of knowledge about the state of the fast dynamics, the first assimilation step primarily updates the pdf of the fast dynamics, yielding minimal information about the slow system. Consequently, the posterior distribution of the slower state remains close to its prior distribution, necessitating only a few additional ensemble members to preserve the ESS of the slower system. As the assimilation process progresses, the inherent chaos in the slow system leads the algorithm to almost entirely resample the slow state at each assimilation step. This pattern continues until the assimilation framework aligns with the true state, at which point the belief about the slow state changes less significantly with each assimilation step. Subsequently, we can extend the usage of previous ensembles representing the slower states for longer periods.

Over time, however, since the truth drifts away from simulations as a result of simulation errors, the ESS of simulations drop with increasing time and eventually are discarded.

Figure 4.6 provides a visual representation of the results obtained from running our algo-

rithm. In this figure, we display the mean and standard deviation of each set of (weighted) ensemble forecasts for the slow state. The lines in the graph are color-coded to match the corresponding colored regions in Figure 4.5. During each assimilation step, the plotted line represents the mean forecast from that specific set of forecasts, with the shaded area around the line indicating a one standard deviation range from the mean. The initial Eulerian forecasts fairly innacurate when compared to the truth. As more observations are assimilated, the ESS of these early forecasts drops low enough to require resampling. After observation 9, however, we see that the newly launched Eulerian simulation does a good job at tracking the truth and consequently is actively contributing to our knowledge about the true state after observation 12 is assimilated.

In Figure 4.7, we present the trajectories of fast ensemble members corresponding to selected slow ensemble forecasts initiated at $t = 2.0s$ after the ninth observation. These plots illustrate the resampling process of fast ensemble members at each timestep, guided by the conditional posteriors. Blue violin plots depict the conditional distribution of fast variables at various observation times, conditioned on the specific slow ensemble member and both current and past observations. Conversely, orange violin plots represent these distributions conditioned solely on past observations, highlighting the evolution of conditional distributions of the fast state with each new observation. The green dot signifies the actual observation at each respective time. The color-coded annotation in the top right corner of the plots reflects the varying weights of specific slow ensemble members through the assimilation of different observations. This color coding reveals that members in closer agreement with the actual observations attain higher weights, thereby more accurately forecasting both the slow and fast state variables. We note that we are only plotting the timeseries of the first observation variable.

4.5.3 Quasigeostrophic Double Gyre

Finally, we show a more practical application where we assimilate Lagrangian data corresponding to a drifter being advected in a Quasigeostrophic double gyre flow, which is an idealized near-surface wind driven barotropic ocean circulation in the mid-latitude regions[134]. We numerically solve this flow with uncertain initial conditions using the aforementioned reduced order DO approach. We numerically solve a reduced order version of the dynamics given by Equation 4.24 with a modular finite volume (FV) solver[197].

$$
\begin{aligned}
\frac{\partial u}{\partial t} &= \frac{\partial p}{\partial x} + \frac{1}{\mathrm{Re}}\Delta u - \frac{\partial(u^2)}{\partial x} - \frac{\partial(uv)}{\partial y} + fv + a\tau_x \\
\frac{\partial v}{\partial t} &= \frac{\partial p}{\partial y} + \frac{1}{\mathrm{Re}}\Delta v - \frac{\partial(uv)}{\partial x} - \frac{\partial(v^2)}{\partial y} - fu + a\tau_y \\
0 &= \frac{\partial u}{\partial x} + \frac{\partial v}{\partial y} .
\end{aligned}
\tag{4.24}
$$

The DO approach allows us to effectively have a very high number of stochastic ensemble members that live in a reduced space. Here, we run our algorithm in a way that the Eulerian simulation is always re-weighted and never resampled. The true flow and corresponding trajectory is plotted in Figure 4.8. The Eulerian forecasts are summarized in Figure 4.9, where the time evolution of the DO coefficients are plotted. The black line corresponds to the true DO coefficients and the blue line and shaded region corresponds to the weighted means and standard deviations respectively. Every column represents a new assimilation step with updated weights leading to an updated forecast (and a lower ESS, mentioned on the X axis). Figure 4.10 represents the Lagrangian forecasts for specific Eulerian ensemble members. The green dot represents the observation assimilated at the given timestep and the blue points represent the resampled Lagrangian forecasts. Yellow points represents the prior distribution of the Lagrangian state. The background color represents the weight of the Eulerian member in question.

4.6 Conclusions and Future Work

In this study, we presented a novel filtering algorithm specifically tailored for the challenges posed by Lagrangian Data Assimilation (LaDA) in geophysical systems characterized by coupled dynamics across multiple timescales. Our approach leverages the Gaussian Mixture Model-Dynamically Orthogonal (GMM-DO) filter within a reduced state space, effectively capturing the non-Gaussian probability density functions (pdfs) inherent in the chaotic Lagrangian dynamics, while efficiently handling the high-dimensional Eulerian system.

Our proposed methodology represents a significant advancement in the assimilation of Lagrangian data, addressing the limitations of traditional Kalman-like methods that struggle with the nonlinear and non-Gaussian nature of such data. By employing a hybrid assimilation scheme, which combines a Particle Filter (PF)-like reweighting approach for Eulerian variables with a resampling strategy for Lagrangian variables with a higher number of ensemble members, we achieve a balance between accuracy and computational efficiency.

The numerical experiments conducted demonstrate the efficacy of our approach in accurately capturing the dynamics of coupled multi-timescale systems, leading to improved state estimates and predictions. The results underscore the potential of our filtering algorithm to enhance the forecasting capabilities in various geoscience applications, using data from coupled systems.

Future extensions to this work include implementing these to other multi-timescale coupled systems. For instance, a weather model coupled with a climate model would be a very good candidate for this filtering approach. Development of an associated smoother is also a natural next step which would allow assimilation of future data from a faster timescale to correct past fields from both fast and slow timescales.

	Descriptors
$(\cdot)_{\mathcal{E}}$	Primary (Eulerian) dynamical system
$(\cdot)_{\ell}$	Coupled (Lagrangian) dynamical system
$(\cdot)^{f}$	Forecast
$(\cdot)^{a}$	Analysis
$\overline{(\cdot)}$	Mean of a stochastic quantity

	Scalars
$_{(i)}$	Primary (Eulerian) Realization index
$_{(i,j)}$	Coupled (Lagrangian) Realization index
$\tilde{(\cdot)}_{m}$	m^{th} DO Mode
r	Rank of DO decomposition
$d_{\mathcal{E}}$	Dimension of primary(Eulerian) state vector
d_{ℓ}	Dimension of coupled (Lagrangian) state vector
k	Discrete observation time index
$N_{\mathcal{E}}$	Number of realizations of the primary (Eulerian) state space variable
N_{ℓ}	Number of realizations of the coupled (Lagrangian) state space variable for every given primary realization
ω	Stochastic process realization
t	Time variable

	Vectors
$\boldsymbol{x_{\mathcal{E}}}$	State space for primary (Eulerian) system
$\boldsymbol{x_{\ell}}$	State space for coupled (Lagrangian) system
$\boldsymbol{y_{\ell}}$	Observation vector
x	Spatial variable
Φ_{m}	m^{th} DO coefficient (random variable)

	Matrices, Operators and Functions
$\boldsymbol{f_{\mathcal{E}}}$	Primary (Eulerain) dynamical system
$\boldsymbol{f_{\ell}}$	Coupled (Lagrangian) dynamical system
$\mathcal{H}$	(Linear) observation operator
$\rho_{(\cdot)}(\cdot)$	Probability density function

Table 4.1: Summary of notation

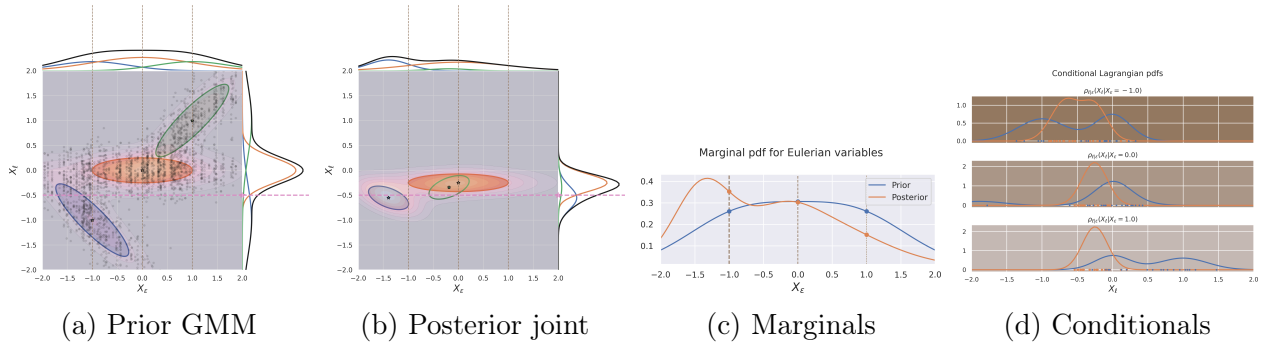(a) Prior GMM (b) Posterior joint (c) Marginals (d) Conditionals

Figure 4.1: Schematics illustrating various steps of the algorithm. (a) A GMM is fitted to joint ensembles of the Eulerian and Lagrangian system. Note that there are multiple Lagrangian ensemble members for every given Eulerian ensemble member. As a result, the joint ensemble members, represented by the black dots in the background, occur in vertical lines. The fitted GMM consists of three mixture components whose mean and standard deviations are represented by the ellipses and whose weights are represented by the transparency of the ellipses. The contour plot in the background represents the total value of the pdf. The black line plots at the edges of the plot correspond to the marginal distributions with contributions from each of the specific mixtures given by the corresponding color-coded line plots. The vertical brown lines correspond to arbitrarily chosen Eulerian ensembles of interest that we will use to illustrate the next steps of the algorithm. The horizontal pink line corresponds to the Lagrangian observation that will be assimilated at this step. (b) The posterior GMM computed using the Bayes' law with prior GMM, the observation model, and the Lagrangian observation. The various components of the plot are identical to the plot for the Prior GMM. We see that the probability mass further away from the observation 'line' significantly drops, as expected. (c) We then plot the prior and posterior marginals (the black line plots at the top of the previous two plots) together and update the weights of the Eulerian ensemble members we were observing using the ratio of these marginal values. The thickness of the brown lines corresponding to these Eulerian ensemble members reflect their new weight. The ensemble member $x_{\mathcal{E}} = -1.0$ has a higher posterior value than prior value and as a result has a higher weight. Conversely, $x_{\mathcal{E}} = 1.0$ has a lower weight. We not that we do not resample the Eulerian values and just reweight them in a way that the weighted ensemble members correspond to samples from the posterior marginal. (d) Here, the prior and posterior conditionals pdfs of the Lagrangian ensemble members corresponding to each of the three Eulerian ensemble members are plotted. The dots at the bottom correspond to the prior and posterior ensemble members. We note that the Lagrangian ensemble members are resampled based on the posterior at every step.
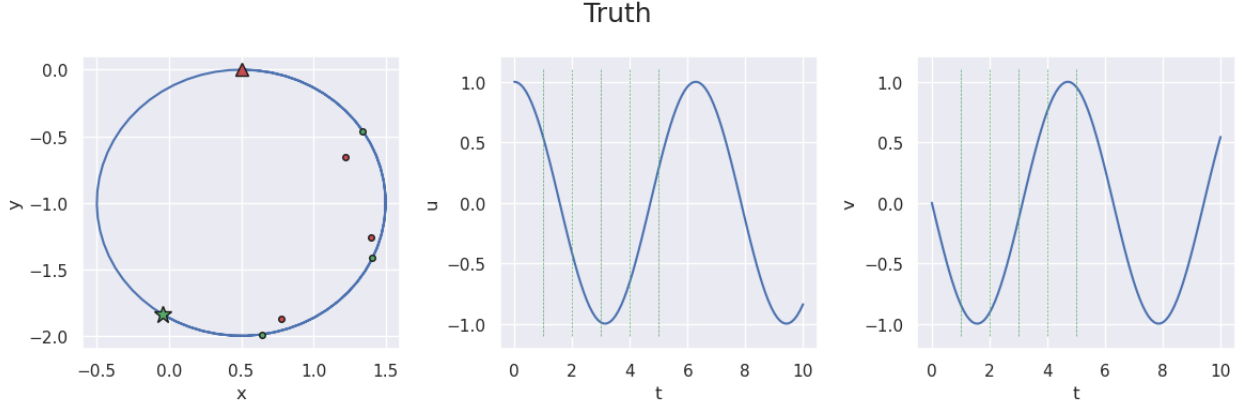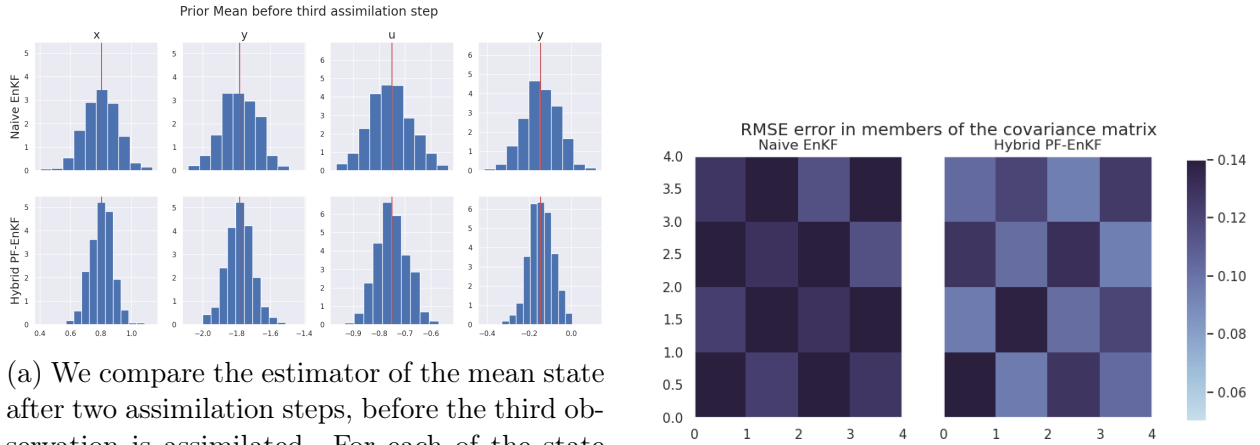
87

Figure 4.2: True dynamics for the validation test with associated observations. The first plot represents the trajectory of the drifter with the green and red points corresponding the true position of the drifter and the measurement received by the algorithm (with measurement error) respectively.

(a) We compare the estimator of the mean state after two assimilation steps, before the third observation is assimilated. For each of the state variables, the red line refers to the mean of the state pdf using the analytical Kalman Filter. The histogram refers to the distribution of the estimates of the state mean using EnKF and the hybridized method respectively over 800 experiment runs. It is clear that the variance of the estimator for state mean is lower when using the hybridized method.

(b) We compare the estimate of the covariance of the state obtained by EnKF and our hybridized approach. We plot the RMSE of the entries of the covariance matrix obtained by the two approaches over 800 runs. The hybridized approach does a better job at estimating the covariance matrix of the state after two assimilation steps

Figure 4.3: Comparison of estimators of Bayesian posterior using EnKF and our proposed hybrid scheme
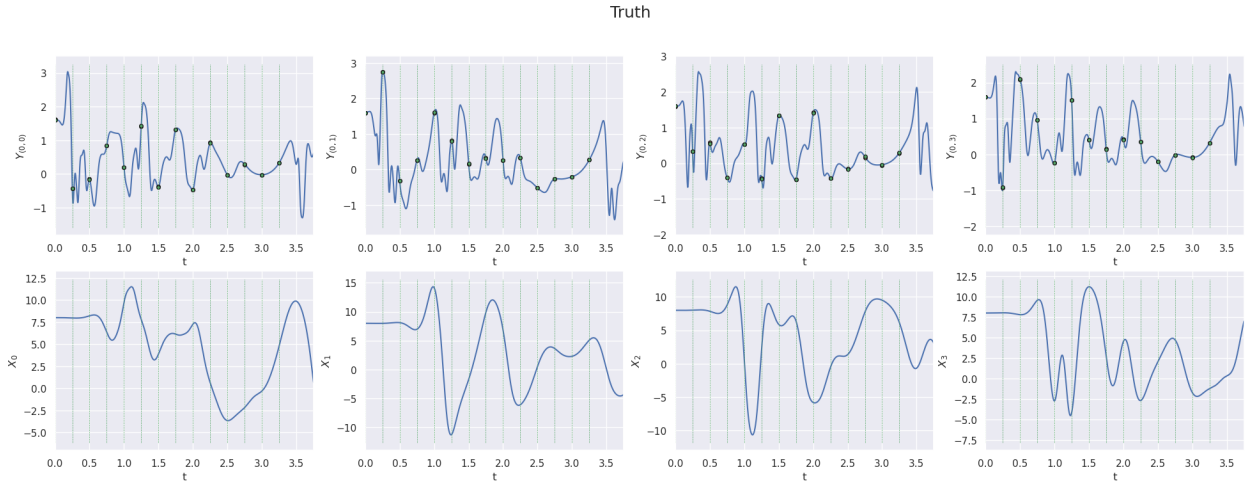
Figure 4.4: True dynamics and observations for the coupled multiscale lorenz system
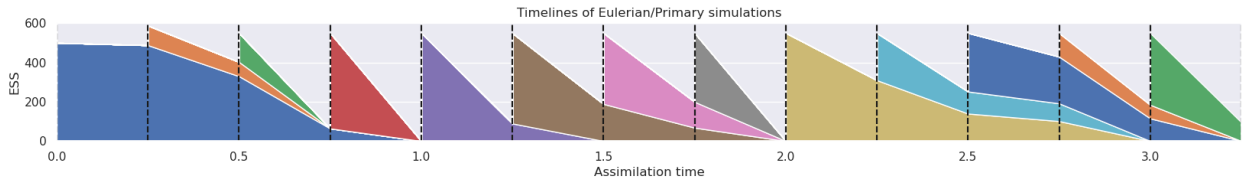
Figure 4.5: Effective sample size (ESS) of various ensembles initiated at different assimilation times
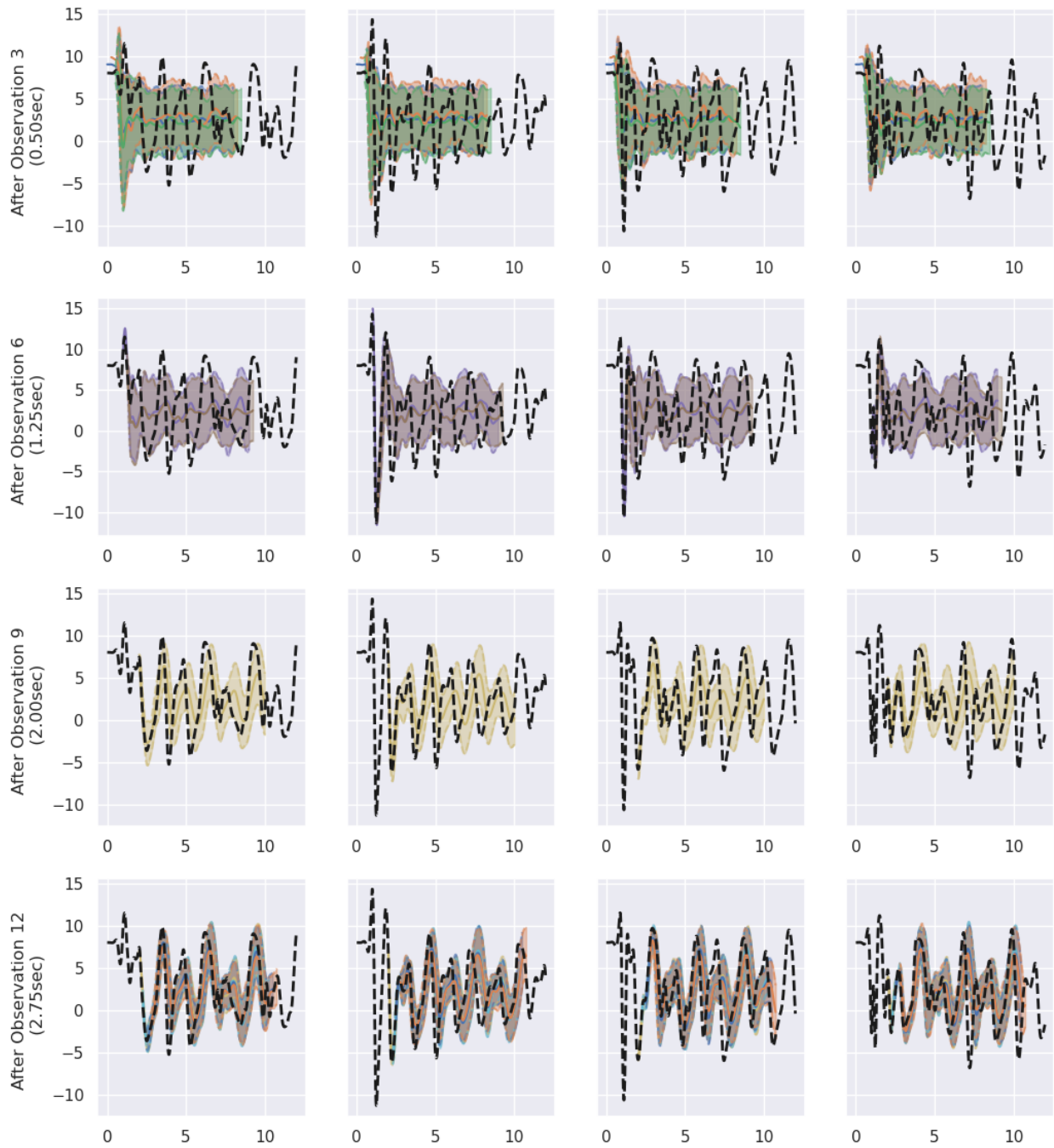
Figure 4.6: Eulerian forecast ensembles after various observations

$$X_{t_0, (i, \cdot)} | X_\varepsilon = X_{\varepsilon, (i)}$$
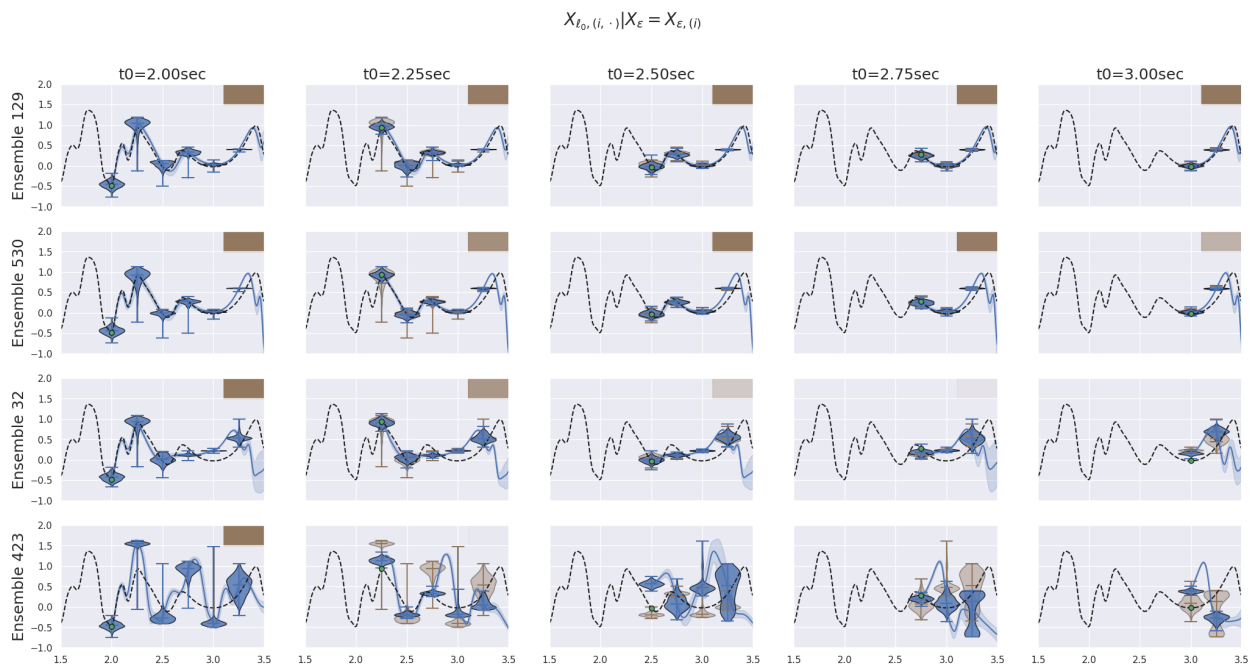
Figure 4.7: Simulations of fast dynamics conditioned on the slower dynamics
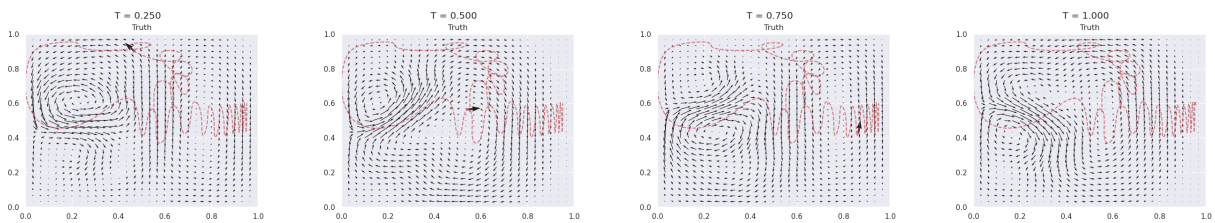
Figure 4.8: True Eulerian realization with the true trajectory superimposed on it
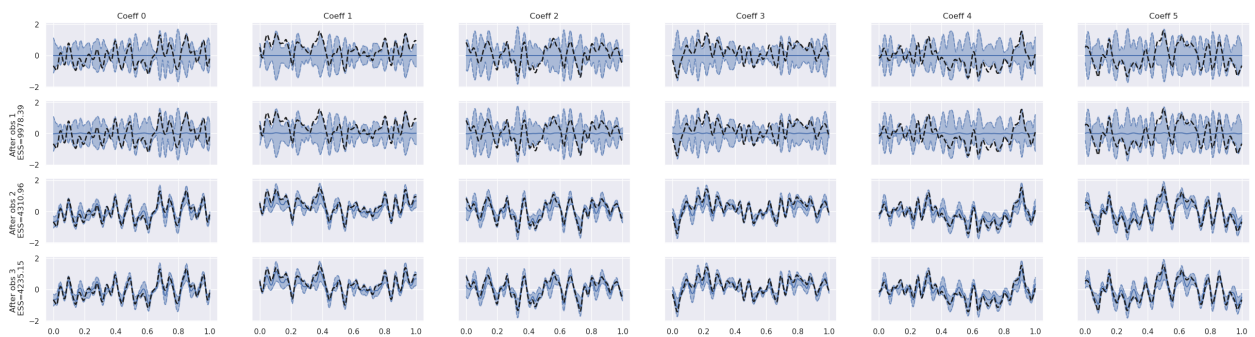
Figure 4.9: Eulerian forecast
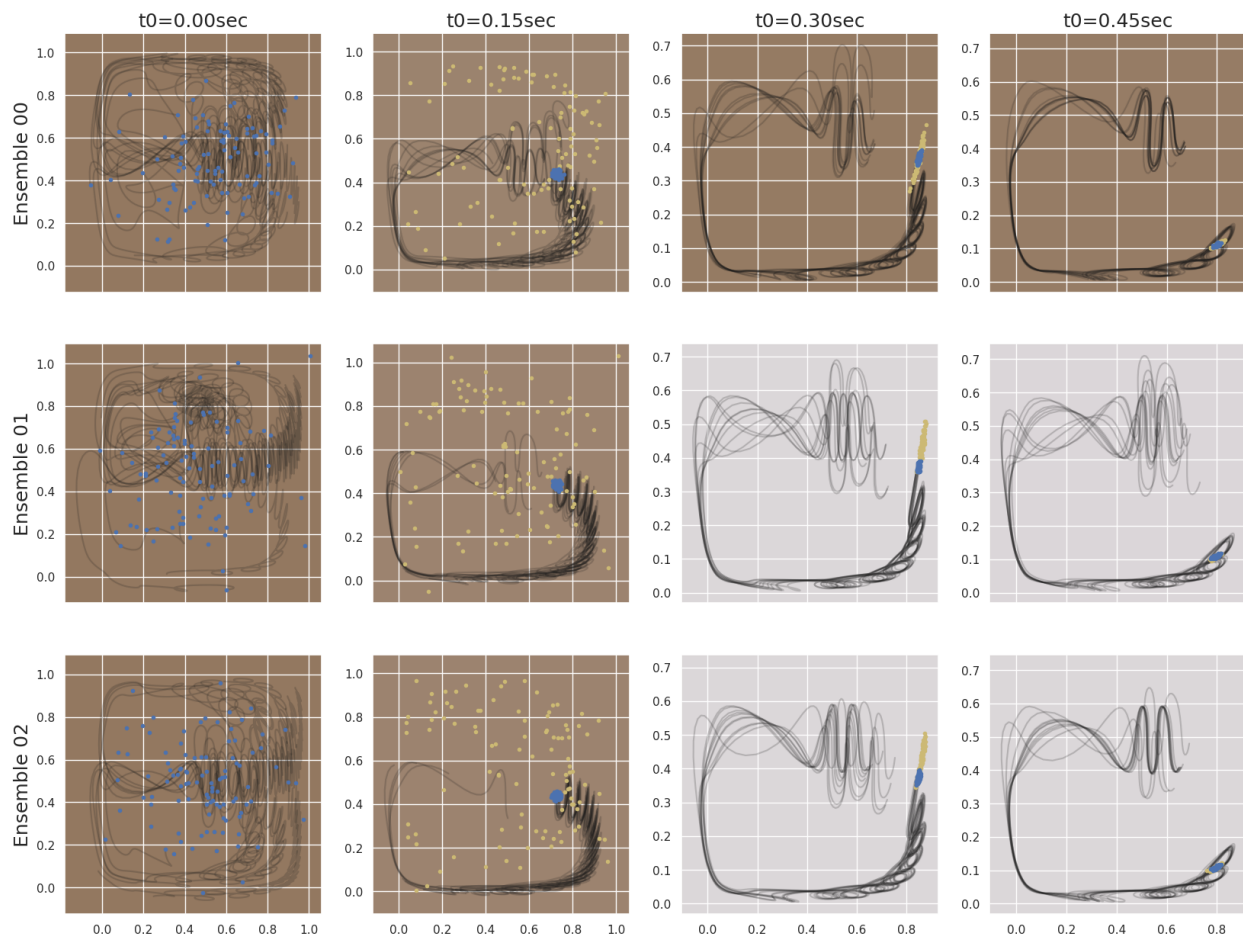
Figure 4.10: Conditional Lagrangian forecast

Chapter 5

Data Assimilative Path Planning

5.1 Introduction

Modern Autonomous Underwater Vehicles (AUVs) and Autonomous Surface Vehicles (ASVs) possess the endurance for extended missions spanning several weeks, making them highly suitable for prolonged ocean experiments. Such missions benefit from pre-planned optimal paths that consider factors like time, energy, and data collection efficiency. This thesis, particularly in Chapters 2 and 3, has explored path planning methodologies that leverage long-term ocean current forecasts. In these chapters, the forecasts were presumed to be accurate and deterministic. However, given the lengthy durations associated with modern AUV and ASV missions, the inherent forecast inaccuracies become non-trivial.

Probabilistic forecasts [197, 199] capture these errors by modelling them as uncertainties in the estimate of the state. Uncertainty quantification methods allow for these uncertainties to be propagated through the model. As a result, we obtain distributions of the state of the ocean at various times as opposed to a point estimate. The ability to obtain optimal paths in these stochastic environments would allow us to plan paths in a way which is robust to model errors.

Incorporating real-time data from AUVs and ASVs into their mission planning frame-

works presents a powerful approach to improve performance. By assimilating the immediate, on-the-fly data from these autonomous vehicles, we can dynamically refine our predictive models, leading to more adaptive and responsive mission strategies. As discussed above, ocean currents can change rapidly and deviate significantly from forecasted patterns due to numerical errors. By using real-time data, AUVs and ASVs can adjust their trajectories on-the-fly to accommodate these changes, ensuring that the mission objectives are met in the most efficient and robust manner possible.

The formulation of this problem is that of a stochastic optimal control problem with time-varying dynamics and colored noise (since errors with respect to the true background flow are not independent in time (in fact, they are highly correlated). Various approaches have been used to plan optimal paths in a stochastic setting. Work by Hollinger et al. [77] build upon their previous work[166], to plan in stochastic environments by modelling the errors as stationary (which assumes the dynamics don't change in time) and non-stationary Gaussian Processes. An Markov decision process (MDP) formulation of the problem inherently implies an assumption of white noise because of the Markovian assumption and subsequently leads to approximations being made despite considering time correlated Gaussian processes.

Another way to formulate this problem is to capture the time-correlated colored noise in the state space itself. This leads to a partially observable MDP (POMDP) formulation where the state now contains the location of the vehicle as well as the state of the total ocean. The dynamics now include the stochastic ocean dynamics augmented with the advection of the vehicle in the ocean. The 'partial' observation is just the location of the vehicle (the entire state of the ocean is not observed). Various existing approaches to solving MDPs and POMDPs tend to rely on machine learning based approaches and discretization of state and action spaces[102].

We wish to propose a method that works in continuous spaces and rigorously deals with the uncertainty in the environment of the vehicle and the position of the vehicle. Our proposed approach aims to use stochastic optimal control approaches based on the work

94

in chapter 3 coupled with Bayesian data assimilation approaches we introduced in Chapter 4 to simultaneously improve the ocean forecasts based on the vehicle measurement while attempting to complete its mission in a time optimal way.

5.2 Problem Statement

We first present a more basic time-optimal version of the problem statement and then propose various ways in which the problem statement can get more complicated. Consider stochastic ocean ocean dynamics, where the ocean state variables are given by $\boldsymbol{x}_{\mathcal{E}}$, and the vehicle dynamics, where the state variables are given by $\boldsymbol{x}_{\ell}$, be

$$\dot{\boldsymbol{x}}_{\mathcal{E}} = \boldsymbol{f}_{\mathcal{E}}(\boldsymbol{x}_{\mathcal{E}}, t; \omega) \qquad\qquad \text{Ocean dynamics} \qquad\qquad (5.1\text{a})$$

$$\dot{\boldsymbol{x}}_{\ell} = \boldsymbol{f}_{\ell}(\boldsymbol{x}_{\ell}, \boldsymbol{x}_{\ell}, \boldsymbol{u}, t; \omega) \qquad\qquad \text{Vehicle dynamics} \qquad\qquad (5.1\text{b})$$

where $\boldsymbol{u}$ represent the controls of the dynamical system.

The initial position of the vehicle is given by $\boldsymbol{x}_{\ell}(0) = \boldsymbol{x}_{\ell,0}$. The goal is to reach the target at a future time $\boldsymbol{x}_{\ell}(t_f) = \boldsymbol{x}_{\ell,f}$

The observation model is given by

$$\boldsymbol{y}_{\ell} \sim \mathcal{N}(\boldsymbol{x}_{\ell}, \Sigma_{obs}) \qquad\qquad (5.2)$$

implying that we observe the postition of the vehicle at observation times.

The goals of the algorithm are:

- Obtain a policy $\boldsymbol{u}(t) = \pi(\boldsymbol{x}_{\ell}, t)$ that minimizes the time t_f to reach the target $\boldsymbol{x}_{\ell,f}$ using the stochastic ocean forecast $\boldsymbol{x}_{\mathcal{E}}(t, \omega)$

- Assimilates the data $\boldsymbol{y}_{\ell}$ to update the ocean forecast $\boldsymbol{x}_{\mathcal{E}}(t, \omega)$ and subsequently the

policy $\pi(\boldsymbol{x_\ell}, t)$

5.3 Proposed Algorithm

We split the algorithm into two steps.

First, we compute the optimal control law within the known stochastic environment using ideas of stochastic optimal control. We essentially implement the multi-time reachability algorithm[39] on the expected velocity field to obtain a policy that is optimal under the expected velocity. Here, we implicitly (incorrectly) assume that the noise is white. We hope for future work which uses ideas from POMDP algorithms to explore alternative ways to compute this optimal policy which works under the assumption that future data is going to be assimilated and the noise model will change based on that assimilation. However, such an approach will require a tree based approach as is common in POMDP solvers and is expected to be expensive.

Secondly, we use the optimal policy and actuate our vehicle based on the optimal policy we computed. We obtain the observations as described by the observation mode. Under the given policy, the coupled ocean and vehicle dynamical system given by equations 5.1 obey the constraints and properties of coupled systems set out in chapter 4. As in the coupled systems we discussed when talking about Lagrangian Data assimilation, the primary system is still the stochastic ocean dynamical system which is extremely high dimensional and extremely expensive to solve. The coupled system on the other hand is the dynamical system of the vehicle and is a simple ODE. We thus use our multiscale filter to assimilate the background velocity of the ocean (by reweighting the ensemble members) and subsequently update the mean velocity of the ocean field. This updated velocity field (which varies in time) is then used to compute the new optimal control law.

Our approach is summarized in the flow chart given in Figure 5.1
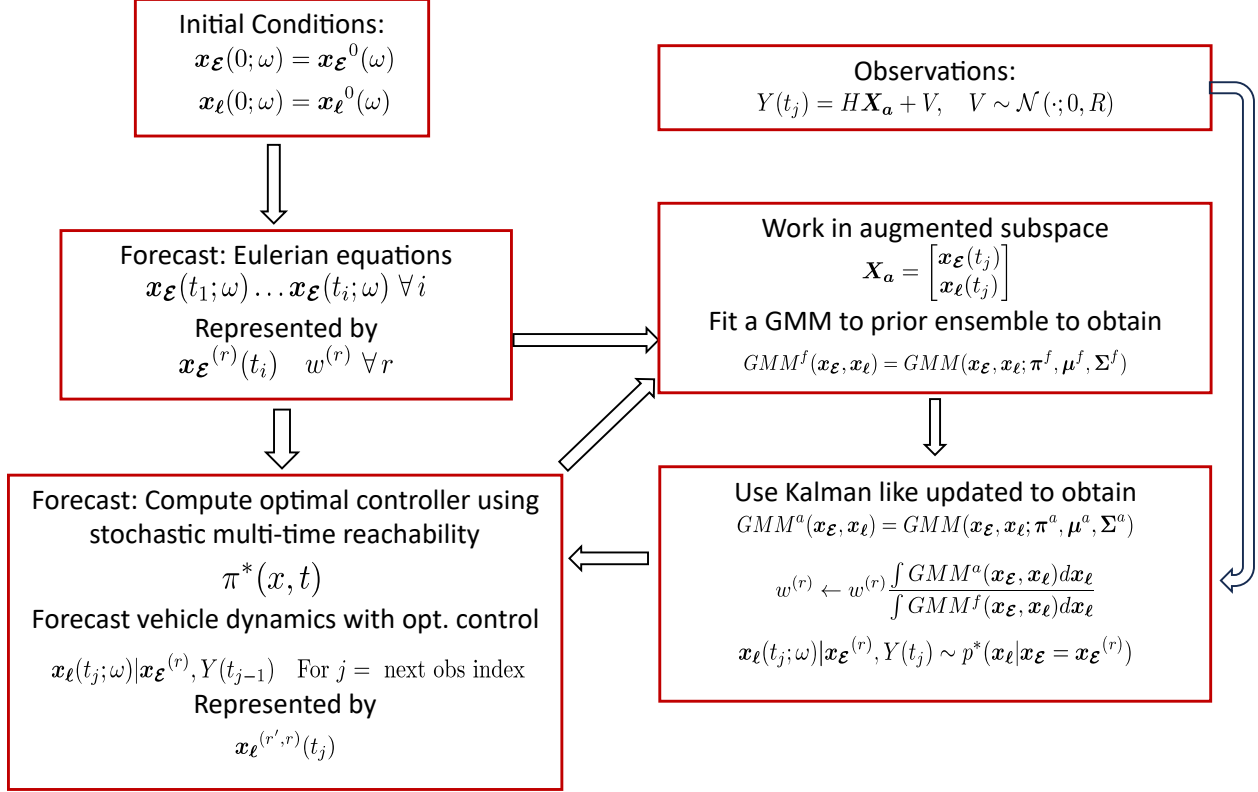
Figure 5.1: Proposed algorithm for data assimilative path planning

5.4 Preliminary Results

We tested out our approach in a moving swirl flow, where the parameters and the location of the swirl flow obeyed a chaotic Lorenz system. Results are summarized in Figures 5.2 and 5.3. We see that the vehicle does indeed learn about the environment and does reach the target. We note that at each assimilation step, we redo the path planning steps but only re-weight the fluid simulations.

We also tested out the approach on an analytical double gyre flow. Results are shown in figure 5.4

Finally, we also showcase the algorithm for a more realistic flow – the quasigeostrophic double gyre flow. This is the same flow we used in 4.5.3. The probabilistic forecasts are computed using the DO methodology discussed earlier in the thesis. Resulting paths and coefficient assimilation plots are give in Figures 5.5 and 5.6.
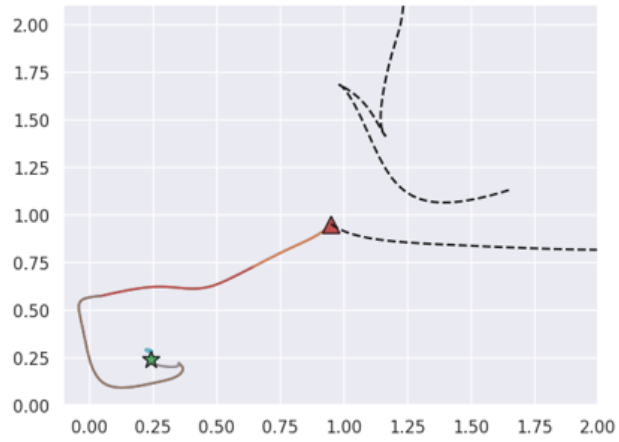
Figure 5.2: Path of the vehicle as it attempts to go from the start point(triangle) to the destination(star). The color of the path changes at every assimilation step.
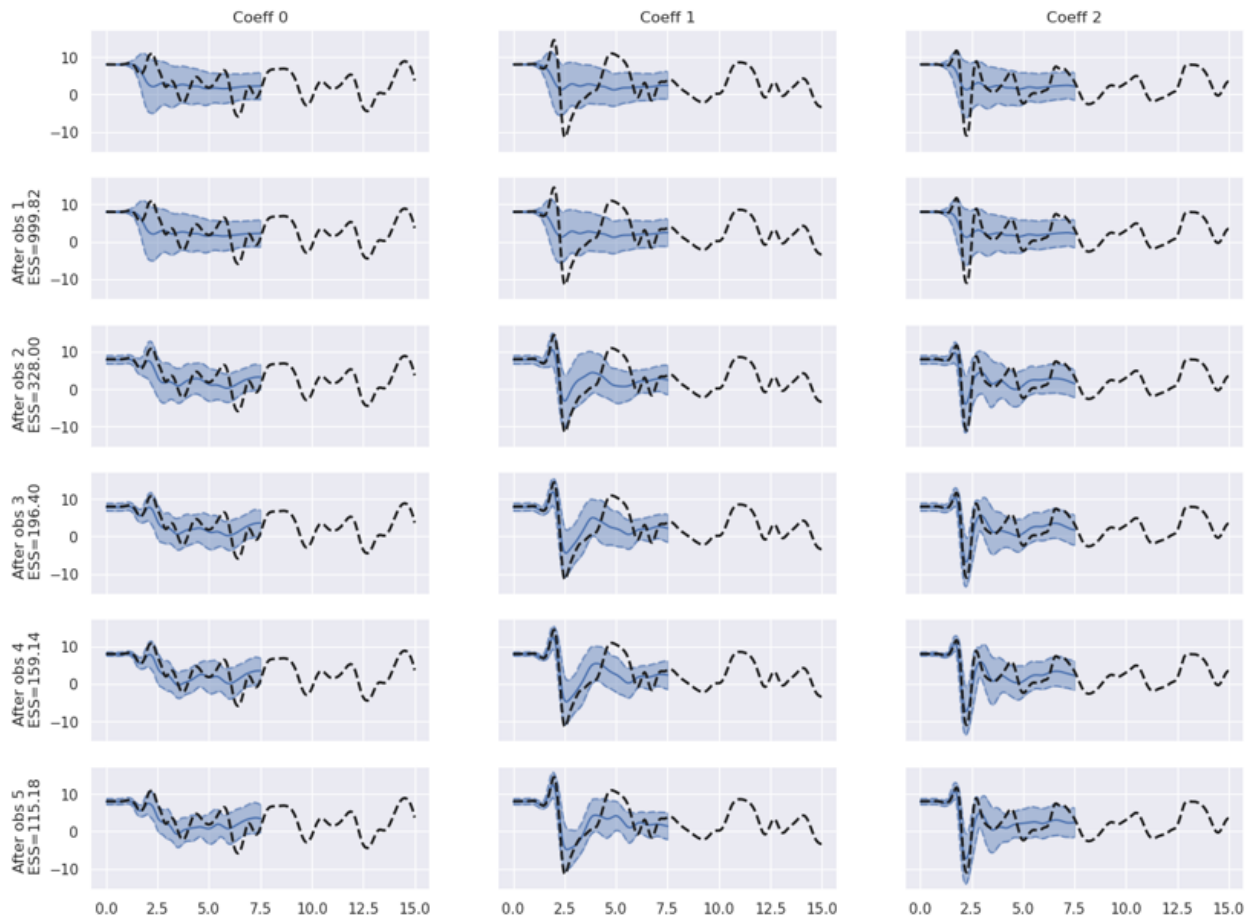
Figure 5.3: Assimilation of swirl flow parameters as the vehicle moves in the flow
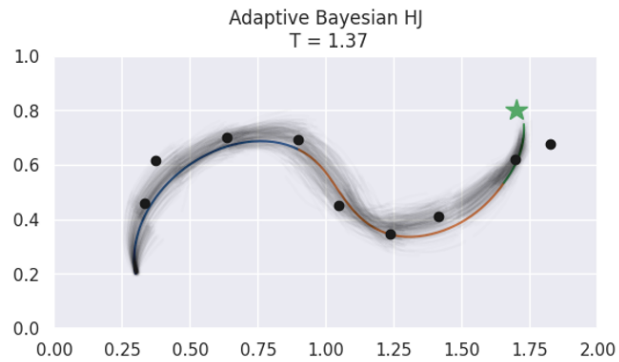
Figure 5.4: Data assimilative path planning on a double gyre flow. The black points are the noise position observations of the vehicle. The colored line is the true trajectory of the vehicle with the color changing when the planning algorithm is solved again. In this setup, 4 observations are assimilated at a time before replanning. The transparent black lines are the stochastic simulations of the vehicle between observation points.
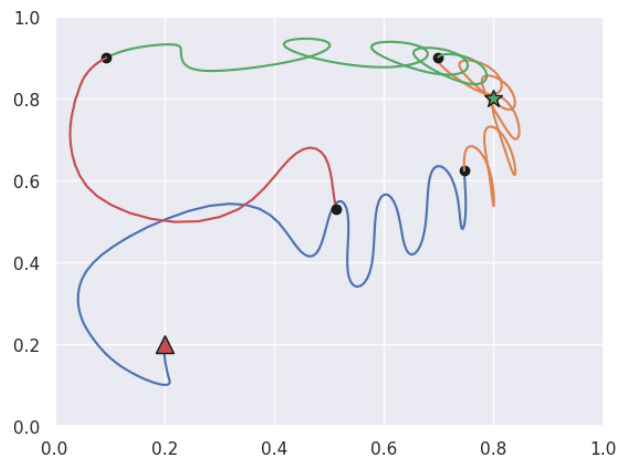
Figure 5.5: Path of the data assimilative vehicle. The black dots correspond to observations which were assimilated
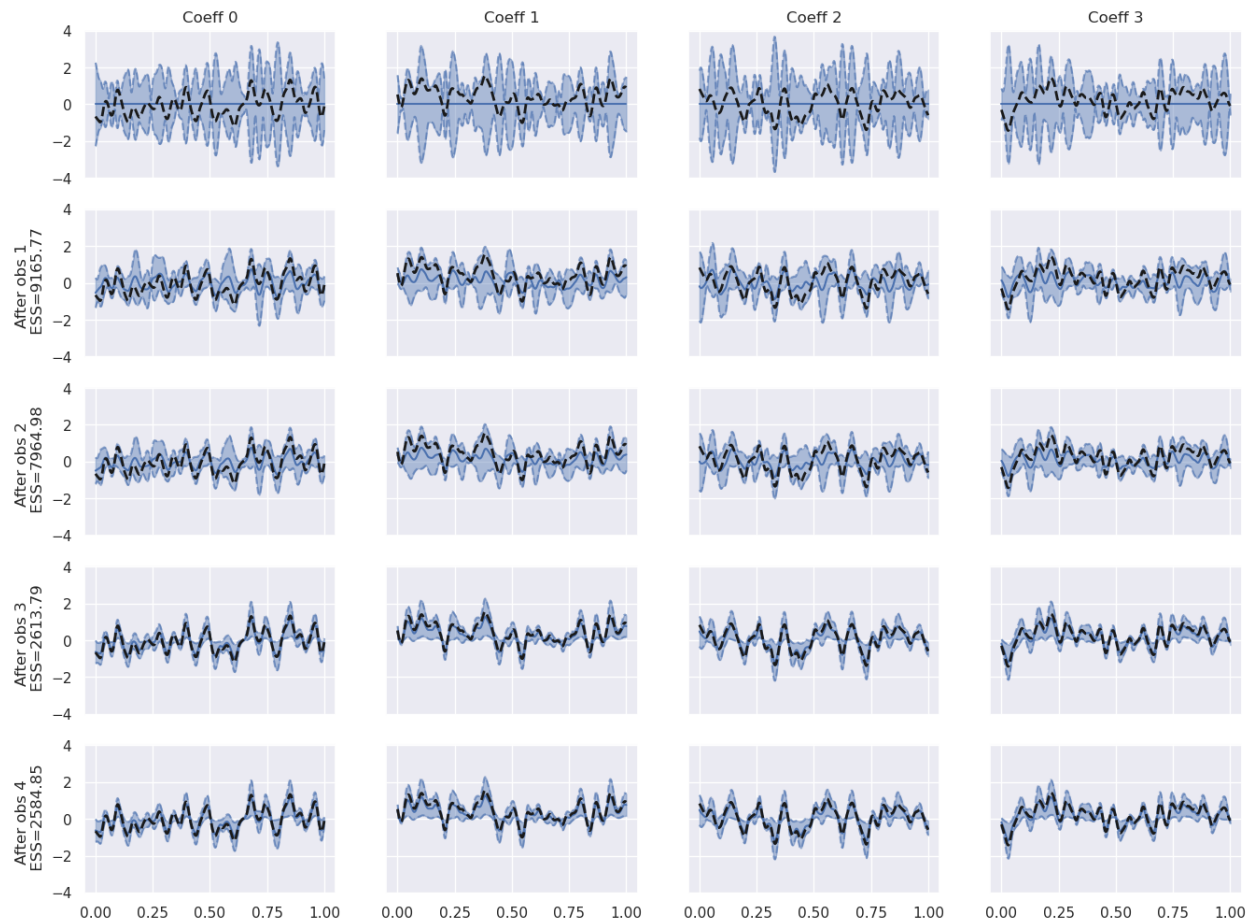
Figure 5.6: The assimilation of DO coefficients describing the quasigeostrophic double gyre flow. Every row corresponds to a new assimilation step

5.5 Conclusions and Future Work

What we present in this chapter are very preliminary results for an approach to a integrated path planning and data assimilation framework. It is a first attempt at formulating a data assimilative path planning framework in a continuous spacetime setting. Future work includes validation and comparison with POMDP and GP based approaches[77, 167], exploring more complicated loss functions and goals (robustness, risk optimality[192] as opposed to expected time optimality), and adding POMDP-like tree search steps when solving for the maximization term in the Hamilton-Jacobi-Bellman PDE.

Chapter 6

Application of Lagrangian Algorithms in Realistic Ocean Settings

In this Chapter, we demonstrate the utilization of several planning and Lagrangian algorithms in data-assimilative ocean simulations and real-time ocean experiments with real data and forecasts issued by our MIT MSEAS group. These results were obtained in collaboration with varied members of the MSEAS group. They involve the characterization of residence times and connectivity in the Red Sea (section 6.1), the study of the transport of plastics in the coastal ocean showcasing results for Massachusetts Bay (section 6.2), the computation of subduction pathways of surface waters to intermediate depths in the Alboran Sea (subsection 6.3.2), and the real-time Bayesian Eulerian-Lagrangian data assimilation of drifter data in the Balearic Sea (subsection 6.3.3).

6.1 Flow Maps and Coherent Sets for Characterizing Residence Times and Connectivity in Lagoons and Coral Reefs: The Case of the Red Sea[1]

For the results described in this subsection, we computed flow maps and coherent sets in the Red Sea using methods and software developed by others in our group [51, 52, 98, 99] and contributed to the writing of the results. The ocean fields and a significant portion of the text were contributed by the other authors of [40].

6.1.1 Introduction

Predicting the residence times and biophysical connectivity of ocean regions is extremely important to characterize the behaviors, dynamics, and health of marine ecosystems as well as to predict the effects of human activities in localized areas on the ecosystems connected to these areas. This is especially critical for the health and resiliency of marine lagoons and coral reefs. Considering the case of the Red Sea, its lagoons and coral reefs constitute an amazing undersea world home to 300 hard coral species and about 1,200 fish, of which 10 percent are local to the region. Its large number of lagoons along the coast (75 on the coast of Saudi Arabia) have large residence times that help coral growth due to the absence of erosion. However, the restricted exchange of water between these lagoons and the Red Sea is also responsible for pollution in the lagoons [170]. Characterizing the different connectivities in the region is thus very important. For example, [168] have showed that connectivity patterns can explain the gene diversity of the coral reefs found in the region.

To understand the connectivity patterns and study the exchange of water masses between various lagoons in the Red Sea, we resort to using Lagrangian field analyses. In the broadest sense, such analyses refer to studies performed using the Lagrangian viewpoint of fluid

---

[1]This section is based on [40].

mechanics [101]. These field analyses provide a quantitative understanding of the transport characteristics of passive materials that flow with the fluid. They compute the attracting basins and repulsive surfaces, and accurately predict the flow patterns of such passive material through determining coherent and incoherent sets [56, 71, 99]. Extensive work has been done regarding Lagrangian transport in geophysical systems, and we refer the readers to [60, 62] for comprehensive reviews.

To address the challenges in lagoons and coral reefs, we utilize our recent advances in efficient four-dimensional (4D: time and space) Lagrangian field theory and methods [50, 51, 97, 98] for characterizing in a principled fashion the residence times and connectivity fields, showcasing the results for the Red Sea. Specifically, we study the connectivity patterns between the Eastern and Western coasts of the Red Sea Basin and the isolation of the southern part of the sea. By looking at how the structures of the flow evolve in presence of seasonal streams, we better understand the effects of these streams on connectivity patterns. Our approach is rooted in the fundamental Eulerian partial differential equations (PDEs) for the Lagrangian flowmap. With our novel numerical method of composition, we can solve these PDEs accurately and efficiently without compounding numerical errors [98]. As a result, instead of classic trajectory-based analyses, we provide accurate 4D field characterization of the Red Sea coherent water masses, residence time, and connectivity dynamic features. The long-term goal is to provide sustained 4D Lagrangian predictions, analyses, and characterizations of multiscale ocean transports, coherent structures, material sets, residence times, connectivity, and stirring and mixing processes in the Red Sea region.

To represent the unsteady and multiscale nature of the ocean fields in the Red Sea region, we utilize the MIT general circulation model (MITgcm) [145] in 3D, including 8 major tidal components. The model is forced by hourly atmospheric fluxes, and a fine scale bathymetry field generated by assimilating several in situ observations is employed. The dynamical characteristics of the regional lagoon basins are mainly forced by tides at local scales, whereas the long term circulation inside the lagoons is driven by the general circulation outside the

lagoon. Another motivation of the present work is to investigate these regional dynamics in the Lagrangian field sense and, in the future, collaborate with observational scientists to help design adaptive monitoring campaigns and plan principled optimal sampling strategies for characterizing the 4D residence times and connectivity fields in the lagoons and coral reefs.

The long-term objectives of the present collaborative Red Sea research are to: (i) Utilize our new Lagrangian field transport theory and methods to forecast, characterize and quantify ocean processes involved in the four-dimensional transports and transformation of water masses, and residence times in the Red Sea; (ii) Apply and expand our multi-resolution submesoscale-to-regional-scale ocean modeling, 2-way nesting, and uncertainty predictions, for real-time forecasting and process studies in the region; (iii) Help design field experiments and predict sampling strategies that maximize information on residence times, 4D pathways and dynamics in the region.

The section is organized as follows. Subsection 6.1.2 overviews the state-of-the-art in Lagrangian analyses and our novel field PDE-based approach, with a specific focus on marine environments. Subsection 6.1.3 discusses the ocean modeling methodology and the regional oceanography of the Red Sea. We then showcase in Subsection 6.1.4 selected results regarding the Lagrangian field dynamics of the Red Sea and its residence times, with an emphasis on specific lagoons. Finally, conclusions are provided in Subsection 6.1.5.

6.1.2 Lagrangian Methods

Lagrangian Fields and Computation

We now briefly review the fundamentals of the Lagrangian viewpoint of material transport field analysis, and the associated recent advances. Typically, we denote any quantity that is being passively advected by the background fluid flow as a (passive) tracer, denoted henceforth by $\alpha(\mathbf{x}, t)$, where $\mathbf{x}$ is the (vectorial) position in the domain of interest Ω and t is

the time, with $t \in [0, T]$. Examples of typical passive tracers include temperature, salinity, inertia-free particulate matters etc. We assume that the tracer quantity $\alpha(\mathbf{x}_0, t_0)$ that was at location $\mathbf{x}_0$ at time t_0 is passively transported with the underlying fluid parcel that was at location $\mathbf{x}_0$ at time t_0, and ends up at location $\mathbf{x}$ at time t. Thus, we have that:

$$\alpha(\mathbf{x}, t) = \alpha(\mathbf{x}_0, t_0) = \alpha_0(\mathbf{x}_0) \tag{6.1}$$

However, we know that the motion of the fluid parcel is governed by eq. 6.2.

$$\dot{\mathbf{x}}(t) = v(\mathbf{x}(t), t) \quad \text{given} \quad \mathbf{x}(t_0) = \mathbf{x}_0 \tag{6.2}$$

where $\mathbf{v}(\mathbf{x}, t)$ is the dynamic velocity field in the domain Ω. For the dynamical system given by eq. 6.2, the forward flow map between times t_0 and $t_1(\geq t_0)$ is defined as:

$$\phi_{t_0}^{t}(\mathbf{x}_0) = \mathbf{x} \quad \text{where} \quad \dot{\mathbf{x}}(t) = v(\mathbf{x}(t), t) \quad \text{with} \quad \mathbf{x}(t_0) = \mathbf{x}_0 \tag{6.3}$$

That is, the forward flow map is simply the position of the fluid parcel at some later time (t) mapped onto its initial position (at time t_0). The inverse of the forward flow map, called the backward flow map is analogously given by eq. 6.4, where now the transport ODE 6.2 is solved in backward time with a specific terminal condition:

$$\phi_{t}^{t_0}(\mathbf{x}) = \mathbf{x}_0 \quad \text{where} \quad \dot{\mathbf{x}}(t) = v(\mathbf{x}(t), t) \quad \text{with} \quad \mathbf{x}(t) = \mathbf{x} \tag{6.4}$$

Substituting eq. 6.4 into eq. 6.1, we obtain eq. 6.5 that concisely states

$$\alpha(\mathbf{x}, t) = \alpha_0(\phi_{t}^{t_0}(\mathbf{x})) \, . \tag{6.5}$$

Eq. 6.5 suggests that computing a passive tracer transport ultimately amounts to accurately computing the flow maps of the underlying dynamical system and composing the said flow

maps with the tracer initial condition.

The forward and backward flow map fields also provide a wealth of additional information. The singular values of the Jacobians of these maps, when scaled logarithmically are referred to as the 'finite time Lyapunov exponents' (FTLEs) [70, 165]. These forward and backward FTLE fields are commonly used to identify Lagrangian coherent structures (LCSs). The ridges of the forward FTLEs approximate the repelling manifolds: they tend to 'repel' water parcels. Two parcels that are close to each other at initial time but on different sides of the forward FTLE ridge will tend to advect farther away from each other than other parcels. The forward FTLEs thus act as material barriers to connectivity, and the forward FTLE ridges can be thought of as a skeleton to the connectivity pattern. On the other hand, the ridges of the backward FTLEs approximate the attracting manifolds: they tend to 'attract' water parcels. They thus increase the chances of connectivity among different water regions, ultimately by sub-mesoscale or turbulent mixing along the ridges in the backward FTLEs. Several other theories and metrics rooted in the flow map are used to determine attracting - repelling manifolds, coherent - incoherent material sets and other quantities of interest in fluid flows [56, 62, 71].

The typical trajectory-based approach to compute the flow maps is to appropriately solve eq. 6.2 in forward or backward time using certain time marching schemes for all possible initial conditions. However, the same can also be achieved by solving a single PDE whose characteristics are described by the said ODE. Specifically, one can obtain the backward flow map ϕ_t^0 by solving the PDE eq. 6.6 forward in time from time 0 to t, with the initial condition $\alpha_0(\mathbf{x}) = \mathbf{x}$:

$$\frac{\partial \alpha}{\partial t} + v \cdot \nabla \alpha = 0; \ \alpha_0(\mathbf{x}) = \mathbf{x} \text{ then } \alpha(\mathbf{x}, t) = \phi_t^0(\mathbf{x}) . \tag{6.6}$$

Similarly, the forward flow map ϕ_0^t is obtained by solving eq. 6.7 backward in time, with the

terminal condition $\alpha_t(\mathbf{x}) = \mathbf{x}$:

$$\frac{\partial \alpha}{\partial t} + v \cdot \nabla \alpha = 0; \ \alpha_t(\mathbf{x}) = \mathbf{x} \text{ then } \alpha(\mathbf{x}, 0) = \phi_0^t(\mathbf{x}) \ . \tag{6.7}$$

Once the flow map is computed, its associated quantities can be appropriately computed. Further, the flow map can be composed with the tracer initial condition to obtain the advected tracer field.

Finally, instead of computing the flow maps over the entire considered interval, one can also compute flow maps over smaller intervals and then compose them appropriately to obtain the flow maps over the larger time interval. Specifically:

$$\phi_{t_0}^{t_n} = \phi_{t_{n-1}}^{t_n} \circ \phi_{t_{n-2}}^{t_{n-1}} \circ \ldots \phi_1^2 \circ \phi_0^1 \tag{6.8}$$

$$\phi_{t_n}^{t_0} = \phi_1^0 \circ \phi_2^1 \circ \ldots \phi_{t_{n-1}}^{t_{n-2}} \circ \phi_{t_n}^{t_{n-1}} \tag{6.9}$$

We refer to this method are the 'method of flow map composition'. Composing such independent flow maps over smaller intervals presents the opportunity to parallelize the computation in the temporal direction, yielding a significant speedup. The individual flow maps are computed over a short interval and hence introduce minimal numerical errors. Further, the individual flow map computations are independent and hence the numerical errors are not compounded, which results in a much lower total error. Further details can be found in [98].

Residence Times Fields

Presently, we are primarily interested in efficiently computing the residence time fields in the domain of interest. These fields represent the time required for a water parcel that started at the considered position to leave the chosen domain of interest. An efficient approach to compute these fields is now developed.

Let Ω_D be the domain of interest in which we wish to compute the residence times. We

initialize a hypothetical tracer field given by:

$$\alpha(\mathbf{x}) = \begin{cases} 1 & \forall \mathbf{x} \in \Omega_D \\ 0 & \text{otherwise} \end{cases} . \qquad (6.10)$$

As stated earlier (eq. 6.5), the tracer concentration at a location $\mathbf{x}$ at some time t, *i.e.* $\alpha(\mathbf{x}, t)$ is computed using the initial tracer concentration $(\alpha_0(\mathbf{x}))$ as:

$$\alpha(\mathbf{x}, t_i) = \alpha_0 \left(\phi_{t_i}^0(\mathbf{x}) \right) . \qquad (6.11)$$

This equation can simply be inverted to obtain eq. 6.12.

$$\alpha_0(\mathbf{x}) = \alpha \left(\phi_0^{t_i}(\mathbf{x}), t_i \right) . \qquad (6.12)$$

We can now use this initial concentration field to determine which water parcels (with their positions indexed at the initial time $t = 0$) will be inside or outside the domain of interest at $t = t_i$, specifically:

1. $\alpha_0(\mathbf{x}) = 0$ and $\mathbf{x} \in \Omega_D$ (inside-outside): Water parcel at $\mathbf{x}$ starts in the domain of interests and is outside the domain at time t_i.

2. $\alpha_0(\mathbf{x}) = 1$ and $\mathbf{x} \in \Omega_D$ (inside-inside): Water parcel at $\mathbf{x}$ starts in the domain of interests and stays in the domain at time t_i.

3. $\alpha_0(\mathbf{x}) = 0$ and $\mathbf{x} \notin \Omega_D$ (outside-outside): Water parcel at $\mathbf{x}$ starts from outside the domain and is outside the domain at time t_i.

4. $\alpha_0(\mathbf{x}) = 1$ and $\mathbf{x} \notin \Omega_D$ (outside-inside): Water parcel at $\mathbf{x}$ starts from outside the domain and is inside the domain at time t_i.

By computing these values at different times t_i we can construct the residence time fields based on when a water parcel exits the domain. Similar fields can be constructed to represent

the intruding time fields as well as the other two cases described above.

6.1.3 Ocean Modeling and Regional Dynamics

A high-resolution MIT general circulation model (MITgcm) [145] was configured at KAUST for the coastal lagoon area offshore of Al Wajh region in the central Red Sea, extending from $36.35°E$ to $37.25°E$ and from $25.2°N$ to $26.4°N$ (Figure 6.1). The coastal model has a horizontal resolution of about $75\ m$ and 50 vertical z-levels, the thickness of which gradually increases from $0.5\ m$ at the surface to $180\ m$ near the bottom. The model is nested within a regional 1-km model configured for the Red Sea with temperature, salinity, and horizontal velocity fields prescribed at the southern and western boundaries on a daily basis. Barotropic tidal currents are added through the amplitudes and phases extracted from the inverse barotropic tidal model TPXO 7.2 Indian Ocean (Red Sea) [REF], including eight major tidal components of semi-diurnal and diurnal frequencies (M2, S2, N2, K2, K1, O1, P1 and Q1). The model is forced by hourly surface wind, air temperature, specific humidity, precipitation, and downward shortwave and longwave radiation of a 3-km Weather Research Forecast (WRF) product [202] downscaled from ERA-Interim products of the European Centre for Medium-Range Weather Forecasts (ECMWF) [34]. Various sources of data have been collected and merged to generate the fine-scale model bathymetry, including several in-situ cruise measurements that were conducted in the lagoon, the General Bathymetric Chart of the Oceans (GEBCO) [80] and satellite images from Google Earth.

At local scales in the Al Wajh region, tides constitute the major forces that determine the dynamical characteristics of lagoon-like basins; however, the long-term circulation inside the lagoons is primarily driven by larger-scale meteorological forces and the general circulation outside the lagoon. Northwesterly winds are dominant over the sea all over the year [107], while the wind regime from the land is more variable with smaller valleys cutting across the mountain ridges and lead to strong easterly jets [84]. The regional oceanic circulation commonly consists of a northward boundary current along the Saudi coast [207, 208], and
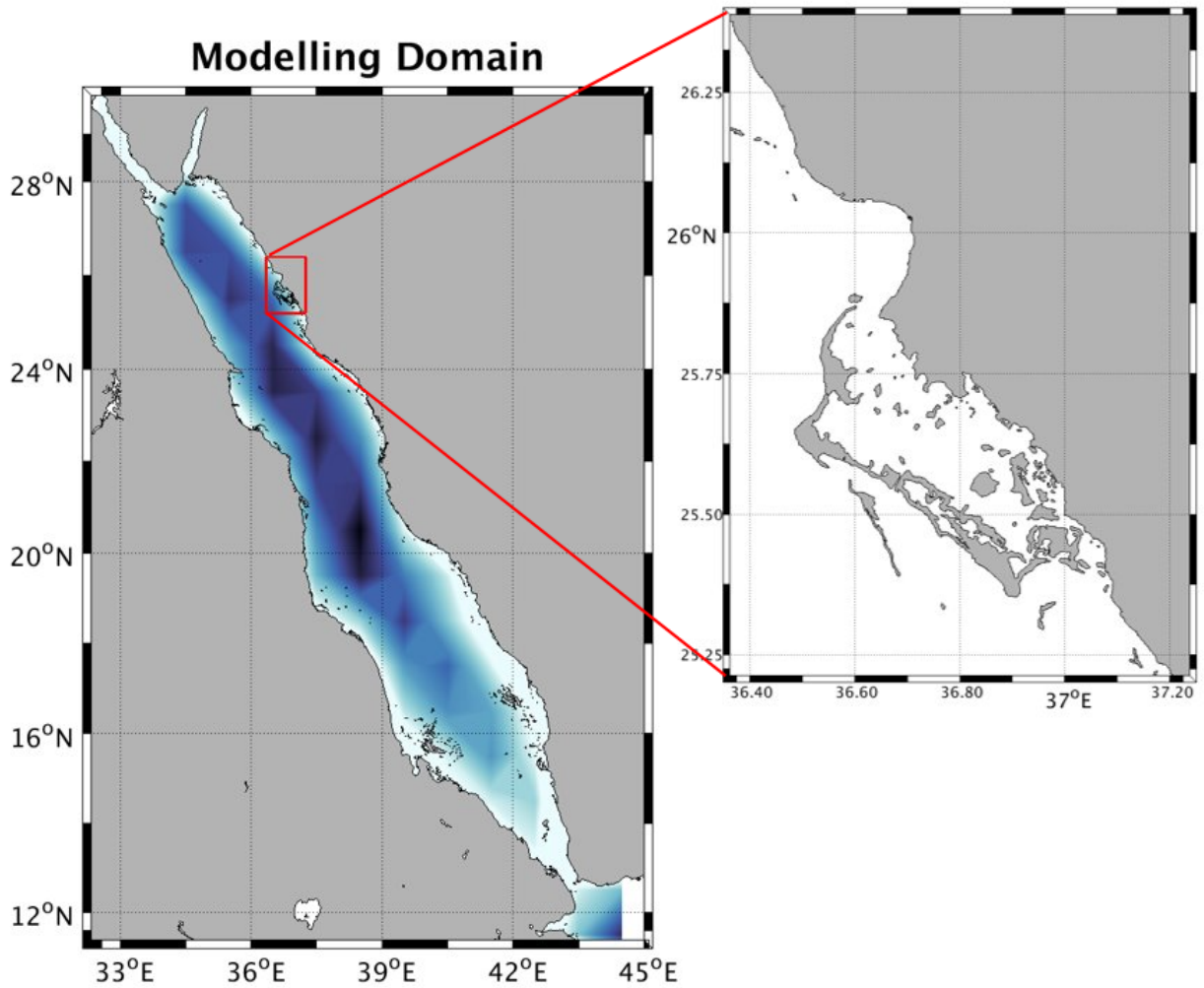
Figure 6.1: Modelling Domains

frequent eddies that are more energetic during winter [209–212]. Such eddy and boundary current events may affect the regional circulation outside the lagoon and potentially influence the flow inside.

6.1.4 Lagrangian Dynamics and Residence Times Results

We now apply the above methodology to compute flow maps, FTLEs, and residence times in the Al Wajh region and overall Red Sea. We then showcase how the FTLE fields qualitatively depicts the skeleton of connectivity in these regions.

Figures 6.2 show the forward x and y flow maps at $0.25\,\mathrm{m}$ and Figure 6.3 the forward x, y and z flow maps $2.75\,\mathrm{m}$, all plotted at the initial positions. That is, these maps collectively plot the final position (through x, y, and z coordinates, with z being positive downward) of a water parcel that started at a particular location at the start time. From the intensity in the gradients of the flow map, it can be seen that the amount of mixing in the Lagoon is much less than outside the Lagoon.

(a) x flow map
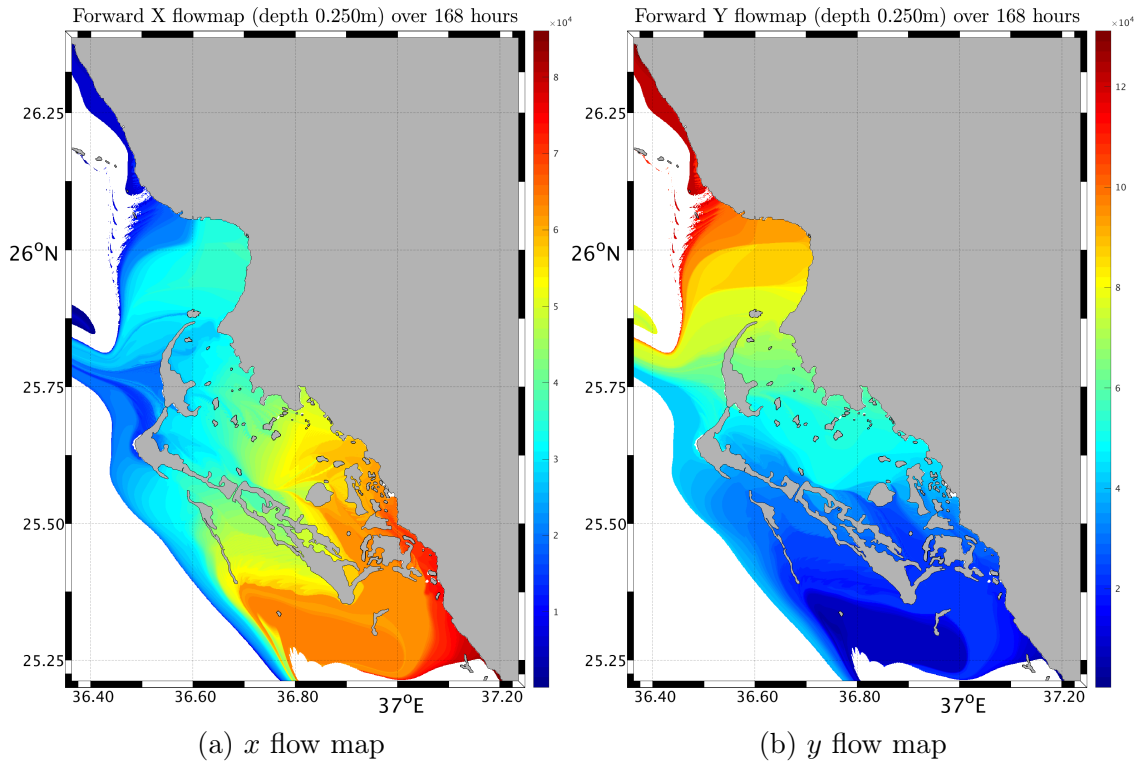
(b) y flow map

Figure 6.2: Forward flow maps (m) over the Al Wajh Lagoon modeling domain from 3 Nov, 2017 to 10 Nov, 2017 at $0.25\,\mathrm{m}$.

Figure 6.4 shows the vertical sections of the 3D x, y and z flow maps, with the Red Sea located to the left of the shown sections. The tall ridges in the repelling FTLE field signify very little mixing with the Red Sea. The z flow map shows upwelling at the eastern ridge of the Lagoon and downwelling on the western coast of the Lagoon. Hence, the regions of larger vertical transport within the Lagoon are located near its edges. Nutrient inputs can thus be expected to occur there as well.

The forward FTLE fields computed using the flow maps from Figure 6.2 are shown in

(a) x flow map (b) y flow map (c) z flow map

Figure 6.3: Forward flow maps (m) over the Al Wajh Lagoon modeling domain from 3 Nov, 2017 to 10 Nov, 2017 at 2.75 m (z being positive downward).

(a) x flow map (b) y flow map (c) z flow map

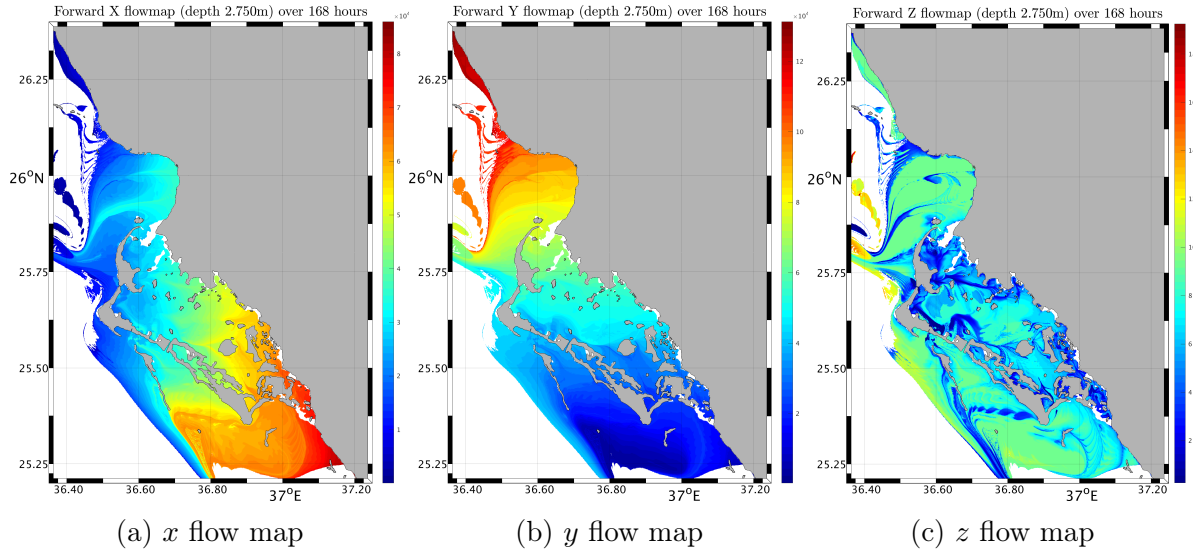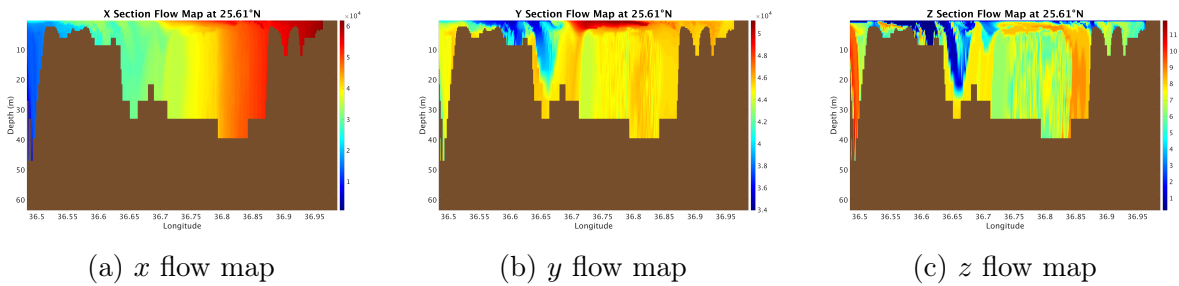Figure 6.4: Vertical section of forward flow maps over the Al Wajh Lagoon modeling domain from 3 Nov, 2017 to 10 Nov, 2017 at 25.61°N.

Figure 6.5. We illustrate the forward FTLE for two different depths: 0.25 m (*i.e.* close to the surface) and 2.75 m from Nov. 3, 2017 to Nov. 10, 2017. As mentioned before, forward FTLEs tend to repel water parcels and thus act as barriers to connectivity. In Figures 6.5(a) and (b), we see a prominent FTLE ridge on the north side of the domain at both the considered depths. Further, we also highlight the existence of the ridges connecting the different small islands at the southwestern boundary of the lagoon. As the forward FTLEs form barriers to connectivity, these ridges together imply that during the 7-days considered, the water in the lagoon does not mix very well with the waters offshore at the southwestern boundary. This can be further confirmed by the FTLE fields over the entire red sea in Figure

114

6.6 (from Jan. 1, 2006 to Jan. 13, 2006), where we see prominent FTLE ridges between the Red Sea and the northeastern coastal regions. Moreover, there seems to be a significant amount of mixing of parts of the lagoon waters and the Red Sea on the northwest and southeast boundaries of the Al Wajh lagoon.
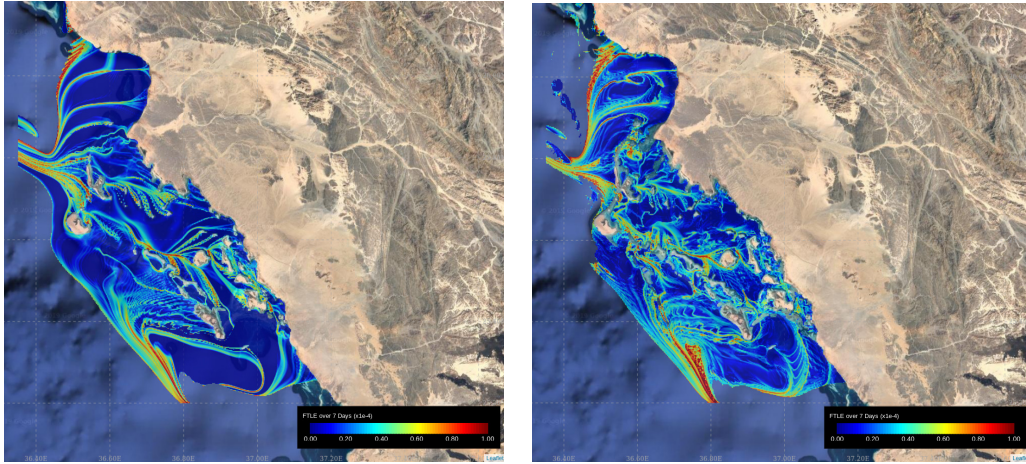
(a) forward FTLE at 0.25 m

(b) forward FTLE at 2.75 m

Figure 6.5: Forward FTLEs over the Al Wajh Lagoon modeling domain, from Nov. 3, 2017 to Nov. 10, 2017 at 0.25 m and 2.75 m, respectively.
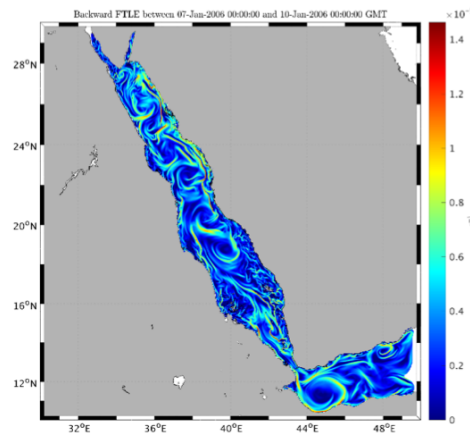

Figure 6.6: Forward FTLEs over the entire Red Sea from Jan. 1, 2006 to Jan. 13, 2006.

While the FTLE fields can indicate which waters of the lagoon are most likely (or not likely) to mix with the offshore Red Sea waters, they do not tell us directly where the mixing occurs spatially (*i.e.* whether the sea water enters the lagoon or whether the lagoon water

enters the offshore sea). The aforementioned residence time fields can be utilized to perform this analysis.

To this end, Figure 6.7 shows residence time fields for water parcels inside the lagoon. Specifically, what is show is the amount of time it takes for a water parcel that started at the specific position to leave the lagoon. We observe that waters near the southeastern boundary exit the domain while those on the northwestern boundary remain inside the lagoon. We also see that the parcels that leave the domain are not uniformly spread out in the lagoon but form a distinct structure near the south eastern boundary. This egress happens mainly at the surface as the residence time fields at 2.75 m depth show significantly less water exiting the domain, see Figure 6.7(b). This is also verified by the stronger FTLE ridges at 2.75 m, see Figure 6.5(b), at the border of the lagoons implying lower horizontal mixing at depth.
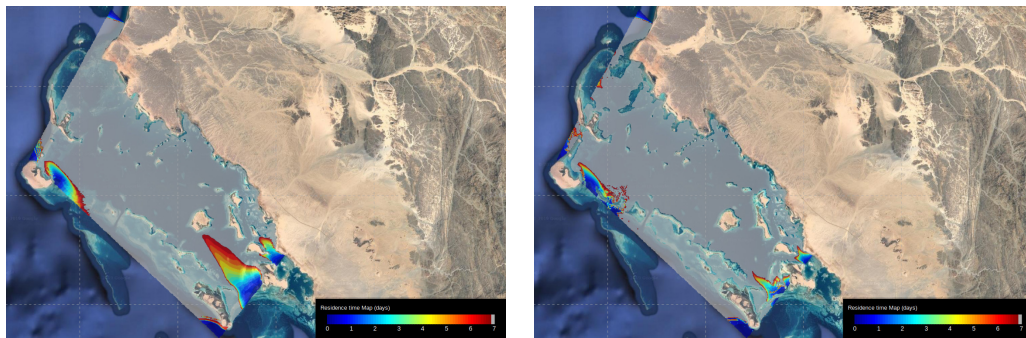
(a) Residence Time at 0.25 m   (b) Residence Time at 2.75 m

Figure 6.7: Residence time fields in the Al Wajh region, from Nov. 3, 2017 to Nov. 10, 2017 at 0.25 m and 2.75 m, respectively.

Using our PDE-based Lagrangian methodology, we can also compute when waters from outside the Lagoon in the offshore Red Sea have entered the Lagoon. We refer to these fields as the "Entrance time" fields, as shown in Figure 6.8. We see that the outside waters enter the northwestern boundary of the Lagoon mainly at the surface. This is the portion of the offshore sea which we had predicted would mix with the waters in the Lagoon. We also note that the seawater parcels that enter the Lagoon form interesting filament structures, as seen in Figure 6.8.

Finally, we observe structures on the southwestern boundary of the Lagoon that enter the

(a) Entrance Time at 0.25 m   (b) Entrance Time at 2.75 m
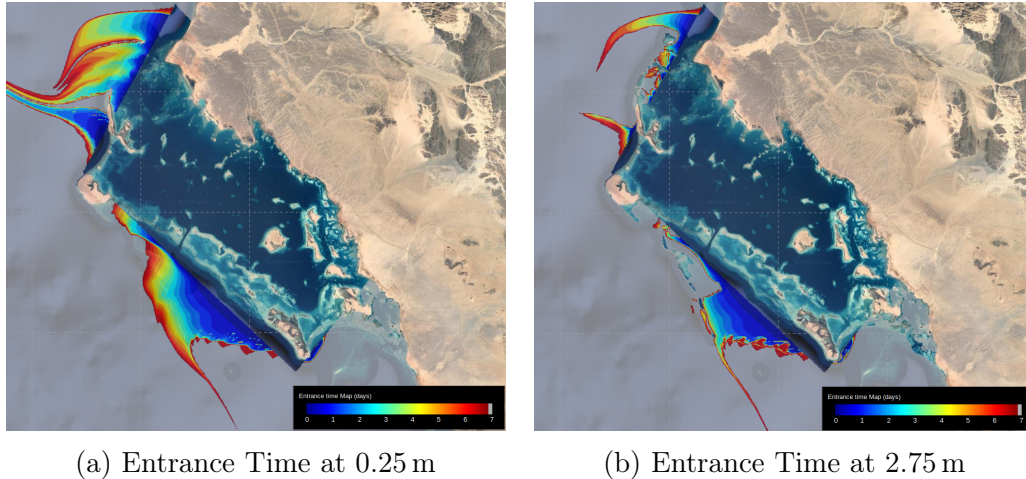
Figure 6.8: Entrance time fields in the Al Wajh region, from Nov. 3, 2017 to Nov. 10, 2017 at 0.25 m and 2.75 m, respectively.

domain of interest. Since we predict that these waters in the Red Sea will not significantly mix with the Lagoon waters, we predict that most of these waters enter and then leave the lagoon domain during the period of interest, without significant mixing.

6.1.5   Conclusions

In this work, we studied the residence times and connectivity patterns of water masses in the Red Sea and Al Wajh Lagoon region. Such capabilities are of great use in characterizing the behavior, dynamics and health of the marine ecosystems native to the region.

To compute the residence times and connectivity patterns, we resort to recent advances in efficient four-dimensional (3D+time) Lagrangian analyses using partial differential equations. Specifically, we show how the method of composition can be efficiently used to compute the residence time fields, *i.e.* spatial fields that denote the amount of time a water parcel spends before exiting the domain of interest. With the same method, we also compute and describe the entrance time fields, *i.e.* spatial fields that denote the amount of time before water parcels offshore enter the domain of interest. We confirm that the ridges of the forward FTLE fields (approximating the repelling coherent structures) do indeed correspond to barriers to material flow, and we observe minimal water flux across these FTLE ridges

in the simulations. That is, the residence time for most of the waters inside the Al Wajh Lagoon region is large, and a comparatively little amount of water mass leaves the Lagoon region. This indicates that even though the Lagoon waters are physically connected to the larger Red Sea offshore, they are only weakly connected in terms of material flow. This is especially important as the Lagoon ecosystem remains relatively protected from any major disturbances or events in the Red Sea. We believe that such in-depth scientific analyses of the biogeochemical ecosystems and their connectivities would go a long way in making informed policy decisions regarding their conservation.

6.2 Plastic Pollution in the Coastal Oceans: Characterization and Modeling[2]

For the results described in this subsection, we used the data-assimilative ocean fields obtained by several of the other authors of [125] to compute and study the plastic transports in the Massachusetts Bay region. For the first time, we characterized the plastic field structures and sets in the Bay based in part on the methods developed in [98, 99]. We contributed to the writing of these results. A significant portion of the text and analyses were completed by the other authors of [125].

6.2.1 Introduction

Since the 19th and early-20th century, plastics have become ubiquitous in the world. They have outgrown most man-made materials: plastics global volume production has surpassed that of steel in the late 1980s [53]. Plastic pollution has proliferated globally, in our lands, rivers and oceans, in wildlife, livestock and consumables, and even in snow from the Alps to the Arctic [11]. Plastic pollution has been described as the next planetary crisis after ozone depletion [194]. Solving this crisis can be broken into two problems: engineering sustainable

---

[2]This section is based on [125].

alternative materials and environmental cleanup of existing plastic contamination, especially in the oceans. The latter problem is of high importance due to the long decay times of most polymeric materials in nature. One of the challenges is the accurate characterization and modeling of the dynamics of marine plastics, from local to global scales. This is one of our motivations.

The need for comprehensive modeling and smart observing of marine plastic pollution is rapidly increasing. This is in part because of the societal realization of the dangers posed by marine microplastics. A major recent effort is that of the "Ocean Cleanup" team [187] who plans to remove surface plastic by utilizing floating collection devices and the ocean currents to gather debris, creating 'sinks' for collecting plastics. As part of this effort, Lebreton et al. [110] modeled and measured plastic concentration in the Great Pacific Garbage Patch (GPGP), and found evidence that the patch is rapidly accumulating plastic. They estimated that more than three-quarters of the GPGP mass consisted of debris larger than 5 cm and that at least 46% of it was comprised of fishing nets. These findings suggest that cleaning larger plastics (macroplastics) is an important task. They also indicate that macroplastics found in the open-ocean likely have sources other than rivers.

Prior studies on marine plastic pollution can be classified into observational and modeling efforts. Observational studies are important because they help us understand the dynamics of plastics in the ocean, and thus could guide the development of plastic models [e.g. 29, 109]. Modeling studies either utilize a global or a regional ocean model to track the dispersion of plastics, using plastic observations for initialization, source functions, and parameter tuning [e.g. 47, 110]. Most studies model plastic as a passive tracer on the surface. However, winds can cause subsurface mixing of microplastics [96]; thus three-dimensional plastic transport models are needed. To go beyond passive tracers, dynamic plastic models are also required to account for sinking, fragmentation, interaction with biology (biofouling), etc. [e.g. 83, 108]. In this spirit, theoretical developments in the motions of finite size particles in fluid flows [e.g. 68, 179] could be extended to modeling of larger plastic pieces as inertial particles.

119

Finally, several modeling efforts are source-inversion studies, with the aim of better locating the sources of plastic pollution [e.g. 2, 85, 86, 92]. For such efforts, high-resolution regional modeling is needed to better identify the main sources and best mitigate pollution.

There are many pathways through which plastics end up in the coastal ocean. The prominent sources are river and sewage discharges, beach and nearshore litter, and inflows from the local and remote oceans. Both macroplastics and microplastics contaminate coastal waters. The focus of the present study is to outline and illustrate a new partial-differential-equation (PDE) methodology for characterizing and modeling such plastic transports in time and three-dimensional space (4D), showcasing results for Massachusetts Bay (Mass. Bay). Specifically, we couple our primitive equation solver for ocean dynamics [64, 65] with our composition based advection solver for 4D Lagrangian transport [98]. We quantify the skill of our ocean physics predictions by comparison with synoptic data. We then forecast for Mass. Bay the fate of plastics originating from four different sources: rivers and sewage, beach and nearshore, local Bay, and remote offshore. We analyze the transport patterns and the regions where plastics tend to accumulate, comparing the results obtained with and without plastic settling. We evaluate our simulated transports and attracting regions using debris and plastic data from the literature and local monitoring systems. Finally, we illustrate global-scale estimates of plastic concentrations.

The section is organized as follows. The methodology is outlined in subsection 6.2.2. The 4D predictions of ocean physics and plastic transports for Mass. Bay are showcased, analyzed, and evaluated in subsection 6.2.3. Global scales estimates of plastic concentrations are not a part of the contribution in this thesis but are presented in the associated paper[125]. Conclusions are in subsection 6.2.4.

6.2.2   Methodology: Ocean and Plastic Modeling

Ocean currents and dynamics are required to model the influx, transport, dispersion, and accumulation of plastic waste in marine systems. Rigorous Lagrangian analyses are essential

to understand and predict such transport characteristics, ideally including settling, fragmentation, and degradation, for the main plastic classes. To plan and implement mitigation and cleanup strategies, understanding the origins and prominent sources of plastics entering the world's oceans is needed. Identifying regions where plastics are prone to be mixed and regions where plastics remain contained is equally useful. Finally, such studies should be performed in full three-dimensional (3D) domains as subduction zones and vertical mixing may have key impacts on plastic transport. Our methodology to address such modeling is outlined next.

Ocean Modeling

To model the ocean, we use PDEs that govern the 4D velocity, temperature, and salinity fields, the so-called primitive-equations [31], here also with a dynamic ocean free-surface field and tidal and atmospheric forcing. The modeling system is our Multidisciplinary Simulation, Estimation, and Assimilation System (MSEAS) [64, 65, 154]. It has been used around the world's oceans [26, 57, 63, 89, 116, 118, 121, 122, 127, 161, 169]. Applications include monitoring [117]; real-time acoustic predictions and DA [42, 106, 124, 206]; environmental predictions and management [9, 27, 28]; relocatable rapid response [33, 174]; path planning for autonomous vehicles [120, 133, 134, 185]; and, adaptive sampling [72, 73, 114]. MSEAS has been tested and validated in many real-time forecasting exercises [1, 57, 58, 116, 118, 121, 122, 124, 126, 163, 169]. Recently, we issued multi-resolution forecasts of 3D Lagrangian transports, coherent structures, and their uncertainties, and guided drifter releases for optimal sampling (NSF-ALPHA). Using ensemble methods [114], we issued large-ensemble forecasts at high-resolution for 3D underwater-GPS exercises (POINT). MSEAS also includes finite-element codes for non-hydrostatic dynamics [198, 200] and a stochastic modeling framework [197, 199].

121

Plastic Modeling

In the present study, we model marine plastics motions as Lagrangian transport with vertical settling. In the horizontal, plastics thus travel with ocean currents, *i.e.* they are passively advected by the flow. In the vertical, their motion is however driven by 2 components: (i) w, the ocean velocity in the vertical, and (ii) w_s, the local settling velocity of the plastic material. That is, the total vertical velocity is $w_{tot}(\mathbf{x}, t) = w(\mathbf{x}, t) + w_s(\mathbf{x}, t)$, where $\mathbf{x}$ is the 3D position in the domain of interest Ω and t is time, with $t \in [0, T]$. An implicit assumption is thus of quasi-staticity, *i.e.* the material is assumed to reach the settling velocity immediately.

We denote the plastic field by $\alpha(\mathbf{x}, t)$. We assume that the plastic quantity $\alpha(\mathbf{x}_0, t_0)$ that was at location $\mathbf{x}_0$ at time t_0 is transported with the underlying fluid parcel that was at location $\mathbf{x}_0$ at time t_0 and also settles due to the buoyancy effects, and ends up at location $\mathbf{x}$ at time t. Thus, we have:

$$\alpha(\mathbf{x}, t) = \alpha(\mathbf{x}_0, t_0) = \alpha_0(\mathbf{x}_0) \ . \tag{6.13}$$

However, the motion of the fluid parcel is governed by,

$$\dot{\mathbf{x}}(t) = v(\mathbf{x}(t), t) \ , \quad \text{given} \quad \mathbf{x}(t_0) = \mathbf{x}_0 \ , \tag{6.14}$$

where $v(\mathbf{x}, t)$ is the velocity field in Ω. As described earlier, the motion of the plastic field can then be written as:

$$\dot{\mathbf{x}}_\alpha(t) = v(\mathbf{x}(t), t) + w_s(\mathbf{x}(t), t) = v_{tot}(\mathbf{x}(t), t) \tag{6.15}$$

$$\text{given} \quad \mathbf{x}(t_0) = \mathbf{x}_0 \ .$$

For the dynamical system given by eq. 6.14, the forward flow map between times t_0 and

122

$t_1 (\geq t_0)$ is defined as:

$$\bar{\phi}_{t_0}^t(\mathbf{x}_0) = \mathbf{x} \ \text{ where } \dot{\mathbf{x}}(t) = v(\mathbf{x}(t), t) \ \text{ with } \mathbf{x}(t_0) = \mathbf{x}_0 \ . \tag{6.16}$$

That is, the forward flow map is simply the position of the fluid parcel at some later time (t) mapped onto its initial position (at t_0). The inverse of the forward flow map, called the backward flow map is given by eq. 6.17, where now the transport ODE (6.14) is solved in backward time with a specific terminal condition,

$$\bar{\phi}_{t_0}^t(\mathbf{x}) = \mathbf{x}_0 \ \text{ where } \dot{\mathbf{x}}(t) = v(\mathbf{x}(t), t) \ \text{ with } \mathbf{x}(t) = \mathbf{x} \ . \tag{6.17}$$

Similarly, one can also define the forward and backward flow maps for the modified dynamical system (eq. 6.15) that accounts for plastic settling. These are given by eqs. 6.18 and 6.19,

$$\phi_{t_0}^t(\mathbf{x}_0) = \mathbf{x} \ \text{ where } \dot{\mathbf{x}}(t) = v_{tot}(\mathbf{x}(t), t) \ \text{ with } \mathbf{x}(t_0) = \mathbf{x}_0 \tag{6.18}$$

$$\phi_{t_0}^t(\mathbf{x}) = \mathbf{x}_0 \ \text{ where } \dot{\mathbf{x}}(t) = v_{tot}(\mathbf{x}(t), t) \ \text{ with } \mathbf{x}(t) = \mathbf{x} \tag{6.19}$$

Substituting eq. 6.19 in eq. 6.13, we obtain eq. 6.20 that concisely states

$$\alpha(\mathbf{x}, t) = \alpha_0(\phi_{t_0}^t(\mathbf{x})) \ . \tag{6.20}$$

Eq. 6.20 implies that computing the plastic transport amounts to computing the flow maps of the underlying (modified) dynamical system and composing the said flow maps with the initial condition.

The forward and backward flow map fields also provide a wealth of information about the flow characteristics over the time interval of interest. 'Finite time Lyapunov exponents' (FTLEs), which are the logarithmic scaling of the singular values of the Jacobians of these maps are often used to identify Lagrangian Coherent Structures (LCSs) [70, 165]. Two parcels

that are close to each other at initial time but on different sides of a forward FTLE ridge will tend to advect further apart from each other than other parcels, and thus forward FTLEs approximate repelling coherent structures. On the other hand, ridges of the backward FTLEs act as repelling coherent structures in backward time, *i.e.* attracting coherent structures in forward time. Several other theories and metrics rooted in the flow map are used to determine attracting - repelling manifolds, coherent - incoherent material sets and other quantities of interest in fluid flows [56, 62, 71].

The typical trajectory-based approach to compute flow maps is to solve eq. 6.14 in forward or backward time using time-marching schemes for all possible initial conditions. However, for continuous fields, the same can also be achieved by solving a single PDE whose characteristics are described by the said ODE. Specifically, one can obtain the backward flow map ϕ_t^0 by solving the PDE (6.21) forward in time from time 0 to t, with the initial condition $\alpha_0(\mathbf{x}) = \mathbf{x}$:

$$\frac{\partial \alpha}{\partial t} + v \cdot \nabla \alpha = 0; \ \alpha_0(\mathbf{x}) = \mathbf{x} \text{ then } \alpha(\mathbf{x}, t) = \phi_t^0(\mathbf{x}) \ . \tag{6.21}$$

The flow map can then be composed with the tracer initial condition to obtain the advected tracer field. Finally, instead of computing the flow maps over the entire considered interval, it is beneficial to compute flow maps over smaller intervals and then compose them appropriately to obtain the flow maps over the larger time interval. Specifically:

$$\phi_{t_0}^{t_n} = \phi_{t_{n-1}}^{t_n} \circ \phi_{t_{n-2}}^{t_{n-1}} \circ \ldots \phi_1^2 \circ \phi_0^1 \tag{6.22}$$

$$\phi_{t_n}^{t_0} = \phi_1^0 \circ \phi_2^1 \circ \ldots \phi_{t_{n-1}}^{t_{n-2}} \circ \phi_{t_n}^{t_{n-1}} \tag{6.23}$$

We refer to this method are the 'method of flow map composition'. Composing such independent flow maps over smaller intervals presents the opportunity to parallelize the computation in the temporal direction, yielding a significant speedup. The individual flow maps are computed over a short interval and hence introduce minimal numerical errors. Further, the individual flow map computations are independent and hence the numerical errors are not

compounded, which results in a much lower total error. Further details can be found in [98].

6.2.3 Plastic Predictions in Mass. Bay

Mass. Bay Regional Dynamics

The circulation in Mass. Bay is commonly from north to south and remotely driven from the Gulf of Maine coastal current and mean wind stress. However, it varies seasonally and in response to wind events. The coastal current can have three branches [113]: one goes around the Bay, one enters the Bay but not Cape Cod Bay, and one flows along Stellwagen Bank, without entering the Bay. Two gyres are often present: one in Cape Cod Bay and another to the north of Stellwagen Basin, but their sense of rotation is variable. Below the main pycnocline, currents are usually of smaller amplitudes than, and of directions opposite to, the main buoyancy flow.

Mass. Bay Ocean Predictions

Ocean Simulation Set-up   Our MSEAS-PE modeling system was used to produce analyses and forecasts for Mass. Bay. The modeling domain (Fig. 6.9) off the northeast US coast has a 333 m horizontal resolution and 100 vertical levels with optimized level depths (e.g., in deeper water, higher resolution near the surface or large vertical derivatives, while at coasts, evenly spaced to minimize vertical CFL restrictions). The bathymetry was obtained from the 3 arc-second USGS Gulf of Maine digital elevation model [196]. The sub-tidal initial and boundary conditions were downscaled from $1/12°$ Hybrid Coordinate Ocean Model (HYCOM) analyses [30] via optimization for our higher resolution coastlines and bathymetry [65]. Local corrections were made using synoptic CTDs of opportunity. Tidal forcing was computed from the high-resolution TPXO8-Atlas from OSU [45, 46], by reprocessing for our higher resolution bathymetry/coastline and quadratic bottom drag (a nonlinear extension of [130]). The atmospheric forcing consisted of hourly analyses/forecasts of wind stresses, net
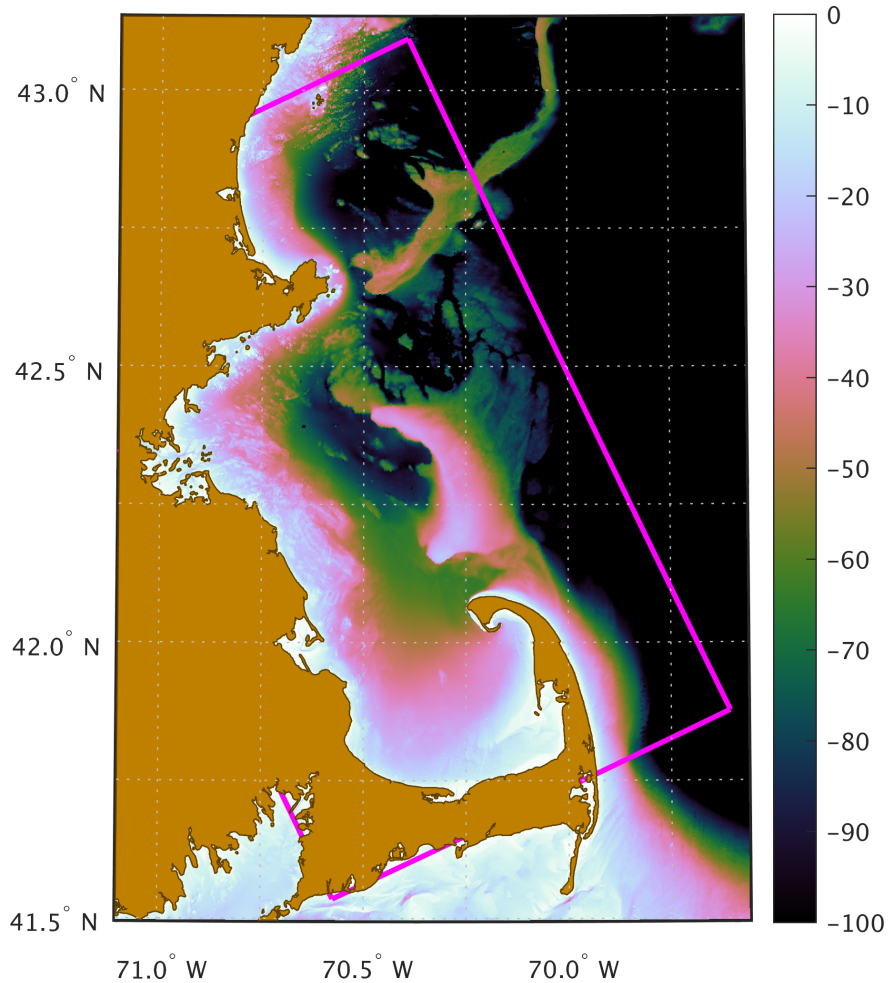
Figure 6.9: MSEAS PE Mass. Bay modeling domain (boundary shown in magenta) and bathymetry (m).

heat flux, and surface fresh water flux from the 3 km North American Mesoscale Forecast System (NAM) [156].

Atmospheric Forcing   The wind stress fields used to force our simulations were computed from wind fields provided by the National Centers for Environmental Prediction (NCEP) NAM forecasts (3 km at 1 hr temporal resolution) [156]. Our analysis of these winds showed six moderate wind events (stresses at least 0.1 N/m^2) and one major event. Specifically, during the first event (Jul. 31–Aug. 1), the prevailing winds were toward the northeast; during the second (Aug. 7–8), toward the northeast; during the third (Aug. 21–22), toward the north-northeast; during the fourth (Aug. 24–26), toward the west-southwest; during the
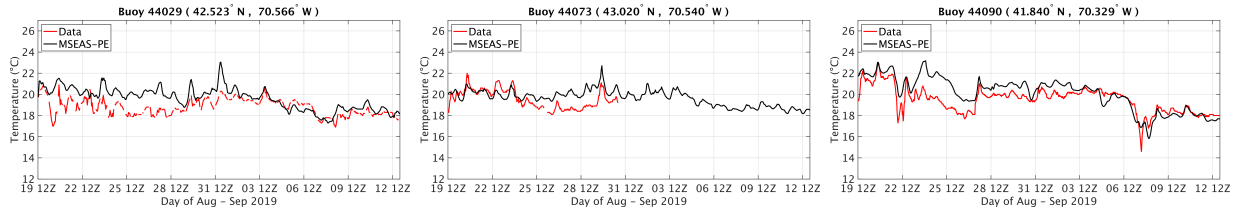
Figure 6.10: Comparison of MSEAS-PE simulated temperature (°C; black line) and NDBC buoy temperature (red line) between August 19 12Z and September 13 0Z, 2019, at buoy 44029 (off Gloucester, MA; left), 44073 (near Isles of Shoals; center; stopped recording on August 31), and 44090 (Cape Cod Bay; right).

fifth (Sep. 2–3), toward the north; and during the sixth (Sep. 4–5), toward the northeast. Finally, on Sep. 7–8, tropical storm force winds from Hurricane Dorian were first toward the northwest, then transitioned toward the southwest. At all other times during the study period, winds were generally light and variable. Also computed from NCEP NAM fields were net heat flux and evaporation minus precipitation (E-P); analysis of the daily-averaged net heat flux fields revealed cooling events on Aug. 6, 14–17, and 25, Sep. 1–2, 6–7, and Sep. 12; analysis of the daily-averaged E-P fields revealed significant rain events on Jul. 31, Aug. 8 and 29, Sep. 3, and Sep. 7.

Ocean Observations

Temperature Buoys. Temperature fields predicted by our simulations were compared to data recorded by four buoys from the NOAA National Data Buoy Center (NDBC) [157]. One buoy (44090) is located near the center of Cape Cod Bay; two (44013, 44029) are near the center of Mass. Bay; the remaining one (44073) is by the Isles of Shoals, near the northern boundary of our modeling domain. Data depths range from 0.46 m to 1 m. The temporal resolution is 30 minutes for buoy 44090 and 1 hour for the other buoys.

CTD Data. During Aug. 2019, the National Marine Fishery Service conducted one of their regular surveys of the US eastern seaboard (ECOMON GU1902 survey [158]). As a part of this survey a number of CTD profiles were taken in the Gulf of Maine, including eight profiles in our modeling domain. The 8 profiles were collected on Aug. 28.

Historical Current Meter Data. Data from a 2011 survey of Boston Harbor and Mass. Bay

127

(a) 10 m, August 20   (b) 10 m, August 26   (c) 10 m, September 4

(d) 30 m, August 20   (e) 30 m, August 26   (f) 30 m, September 4
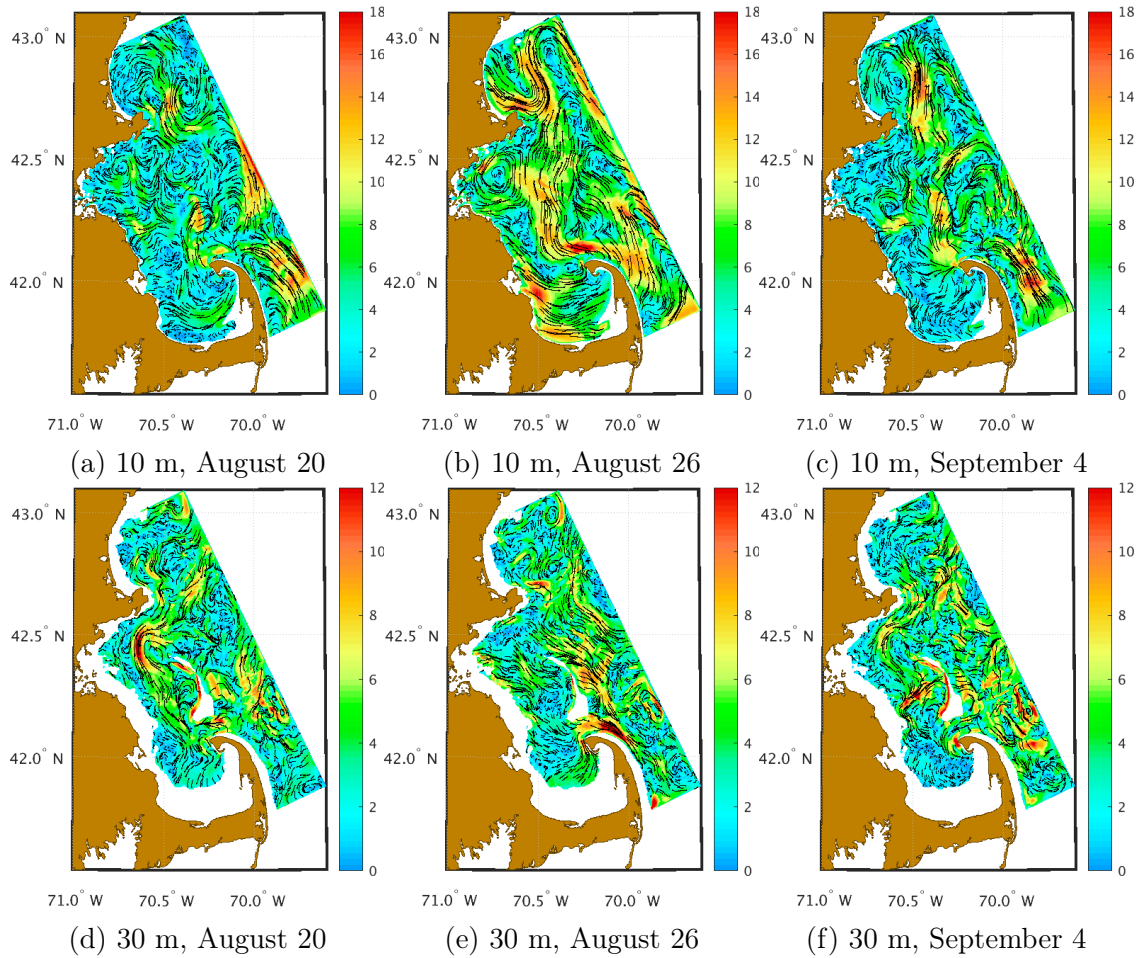
Figure 6.11: MSEAS-PE simulated daily-averaged velocity (cm/s) overlaid on speed, at 10 m and 30 m on Aug. 20, 26, and Sep. 4, 2019.

were obtained from the National Oceanic and Atmospheric Administration (NOAA) [160]. These data consist of time series of velocity measurements at 2–10 minute intervals and at 10–20 depths at a single location. For this survey, the duration was a bit over 1 month.

Ocean Model Validation and Data-Model Comparisons   Mass. Bay has a fairly small extent (roughly $\frac{1}{2}^{\circ} \times 1^{\circ}$) and even smaller features affecting its circulation (e.g., Cape Cod, Cape Ann, narrow coastal currents, river inputs). It is therefore not feasible for a $\frac{1}{12}^{\circ}$ global model to resolve its dynamics. Hence, part of our downscaling methodology includes the use of in situ data to correct the under-resolved fields. We were able to acquire synoptic CTD data from the NMFS [158]. We computed differences between these profiles and the HYCOM
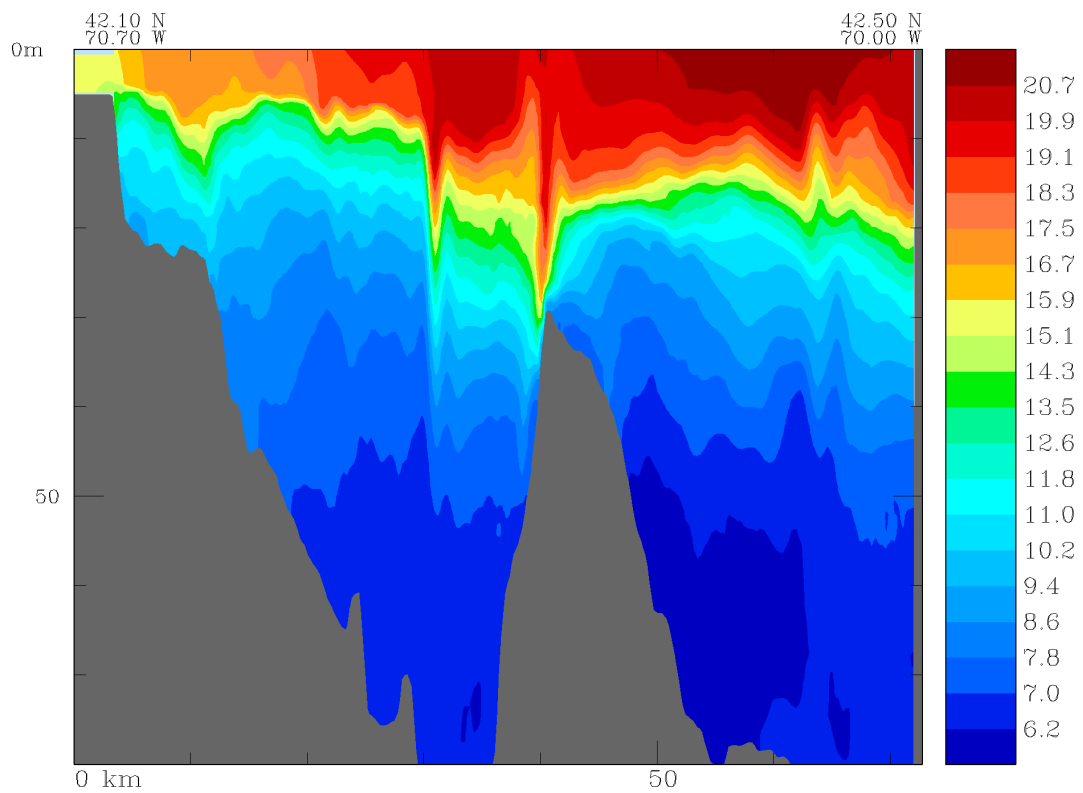
Figure 6.12: MSEAS-PE simulated temperature (Aug 21, 2019) in a section through Stellwagen Bank showing internal tides/waves.

fields and objectively mapped these error profiles to correct the downscaled HYCOM IC/BC fields.

We used the historical NOAA current meter data to improve our tidal forcing. From these data, time series of the barotropic velocities were constructed. Tidal constituents were then best fit to these series using the UTide code [25]. These were then used to tune the bottom drag and friction parameters in our barotropic tide model. The tuned tidal fields had a 30% smaller RMSE than the original global TPXO8 fields [45]. These tuned tides were then used to force our MSEAS-PE simulations.

Having employed the CTD profiles in the downscaled IC/BCs, they are no longer independent validation data. Hence, for such validation, we used other data, including NOAA NDBC buoy data [157]. In Fig. 6.10, we show the comparison of near-surface temperature data from the buoys (red curves) to the MSEAS-PE simulated temperature interpolated to the buoy positions/depths (black curves). Given the uncertainties in the 3 km atmospheric forcing and those arising from the unresolved processes in the downscaled IC/BCs, we do not expect tight matching in these point comparisons. Nonetheless, we find that the MSEAS-PE produces similar daily cycle excursions (both in amplitude and frequency). We also see that the general trends and events do align well and that the mismatches (typically between 0 and 2 °C) are what we expect for the given uncertainties. We also note that by September, for the two buoys that recorded data, the accuracy becomes very good. Comparisons with SST and HF-radar data (not shown) also indicate acceptable simulations.

Simulated Dynamics During Aug.–Sep. 2019, several wind events modified the coastal circulation, as in [9, 113]. Initially, the flow in the thermocline (30 m) enters Mass. Bay from the north by Cape Ann (Fig. 6.11d). It proceeds southward to the west of Stellwagen Bank and enters Cape Cod Bay. The flow then moves up the shallower bathymetry of Cape Cod Bay and joins an upper layer (10 m) anticyclonic circulation in Cape Cod Bay before it exits Mass. Bay by Race Point (Fig. 6.11a). Also during this period, a number of small

eddies persist in the upper layers of north and central Mass. Bay but below the mixed layer. Following the wind event of August 24–26, the 30 m southward flow is displaced east of Stellwagen Bank (bypassing Mass. Bay; Fig. 6.11e). In the upper layers (10 m) a cyclonic coastal circulation is established all along Mass. Bay, including a cyclonic coastal flow in Cape Cod Bay (Fig. 6.11b). The small subsurface eddies are replaced by a large cyclonic eddy in northern Mass. Bay whose western side is part of the cyclonic coastal circulation. During Aug. 26–31, the 30 m flow reestablishes itself in Mass. Bay. The 30 m inflow by Cape Ann is maintained through the wind event of Sep. 2–3, along with the general southward flow in the northern half of the Mass. Bay (Fig. 6.11f). South of 42° 12', the flow is still mainly south but with some rising along bathymetry on the western side and in Cape Cod Bay. At 10 m depth south of 42° 6', the remnants of the cyclonic coastal circulation carry the water that came up from 30 m around to the south of Cape Cod Bay where it again climbs topography to join an anticyclonic circulation at the surface (Fig. 6.11c). These overall conditions are modified by tides and resulting internal tides and solitary waves generated by the bathymetry, especially from Stellwagen Bank (Fig. 6.12).

Mass. Bay Plastics Predictions: Surface Passive Tracers

We now showcase the method of composition to predict and analyze plastic transport in Mass. Bay, using the MSEAS-PE 4D current fields. We first consider surface plastics and assume that plastics are passively advected by the surface ocean flow during Aug. 16–Sep. 5, 2019. We consider four initial sources of surface plastics: (i) river mouths, (ii) beach and nearshore, (iii) offshore inside domain, and (iv) offshore outside domain (plastics entering the domain during the simulation), as shown in Fig. 6.13(a). The final surface plastic field after 10 and 20 days of passive advection are shown on Figs. 6.13(b) and (c), respectively. We observe that there is significant stirring between the nearshore and interior plastics, especially over 20 days. Further, plastics from the Merrimack River mouth exit the domain through the northern boundary. This is largely driven by winds over the first 3 days. Although not

(a) Initial plastic location

(b) Plastic location after 10 days (Aug. 16–26)

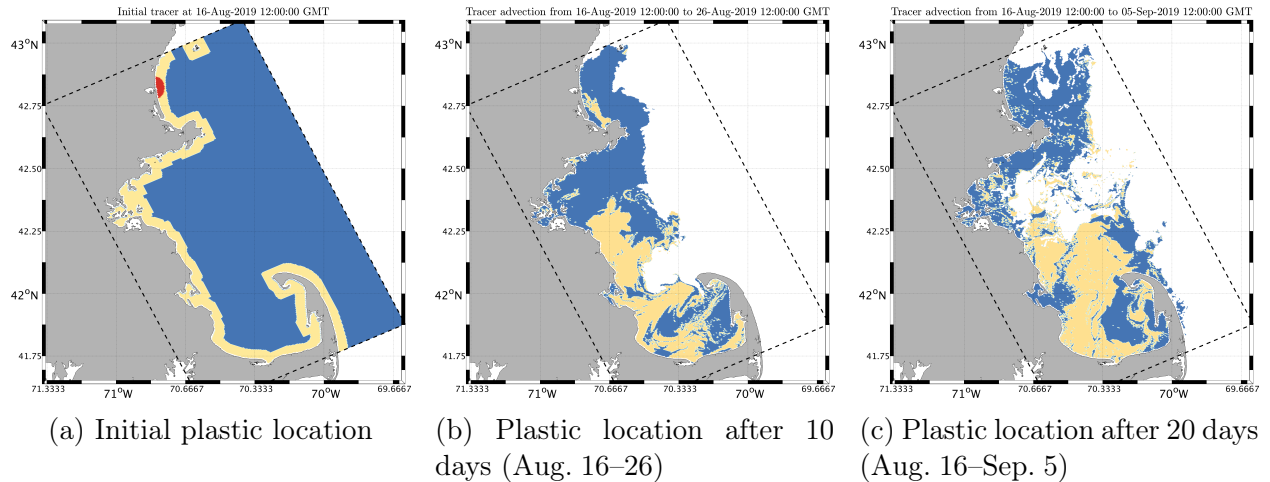(c) Plastic location after 20 days (Aug. 16–Sep. 5)

Figure 6.13: Surface plastic location initially and after 10 and 20 days of simulated passive advection. Red denotes plastic originating at the mouth of the Merrimack River, beige plastic originating at the shoreline, blue plastic originating in the rest of the Mass. Bay domain, and white plastic originating outside the domain.

strong, the daily average winds are consistently to the northwest during this time, north of Cape Ann, while the instantaneous winds are to the northwest and north-northeast. We further observe that the surface waters (and hence the passively advected plastics) that start around the Stellwagen Bank area are replaced by waters from outside the domain especially after 20 days.

Comparing the advected fields (Fig. 6.13) with the attracting FTLE fields (Fig. 6.14), we clearly observe the chaotic stirring in the Stellwagen Bank and Basin, and Boston harbor regions, as delineated by the presence of several entangled FTLE ridges. We also observe strong attractive ridges near Cape Cod that include regions of subduction. These ridges attract the surface waters and also the passively advected plastics in this region, as corroborated by Fig. 6.13(b). Much of the beach and nearshore plastic from northern Mass. Bay is flushed into the Stellwagen Bank/Basin stirring region by the cyclonic circulation set up during the wind event of Aug. 24-26 (see subsection 6.2.3). The cyclonic circulation established in Cape Cod Bay by the same wind event also drives the beach and nearshore plastic from the "Upper Cape" (southwest portion of the Bay) into the attracting ridges of the northern Cape Cod Bay, while the beach and nearshore plastic from the "Middle Cape"

132

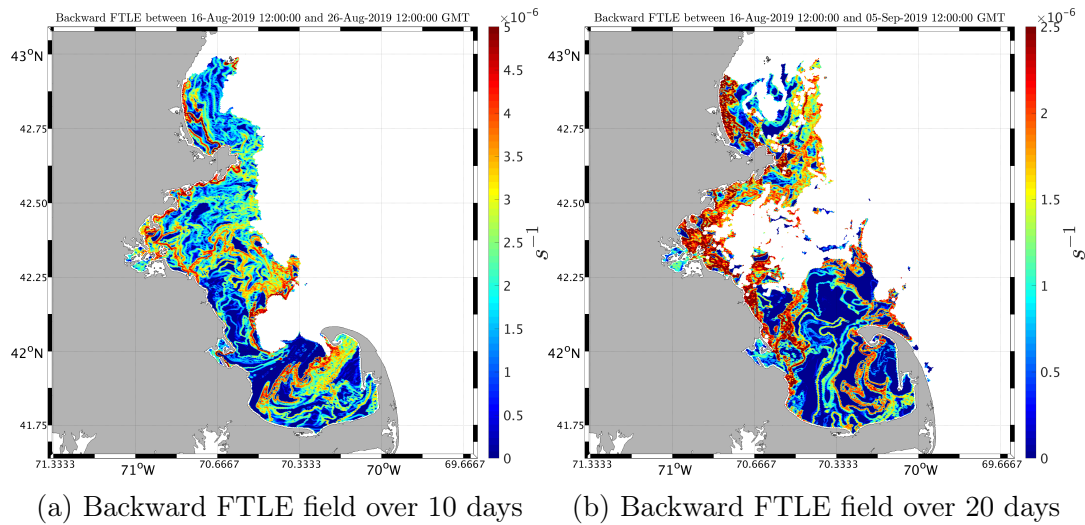(a) Backward FTLE field over 10 days (b) Backward FTLE field over 20 days

Figure 6.14: Predicted backward (*i.e.*, attracting) FTLE fields over the Mass. Bay domain: (a) Aug. 16–26 and (b) Aug. 16–Sep. 5, 2019.

(southern portion of the Bay) is driven to the western shore of the "Lower and Outer Cape" (southeast corner of the Bay). Later, the surface anticyclone that develops from the Sep. 2-3 wind event flushes the plastic off this south-southeast corner of the Bay and into the large patch that develops in western Cape Cod Bay extending northeast to Stellwagen Bank.

(a) Plastics released from the Merrimack River mouth (b) Plastics released at the shoreline (c) Plastics released in the coastal ocean interior (d) Plastics entering from the domain boundaries
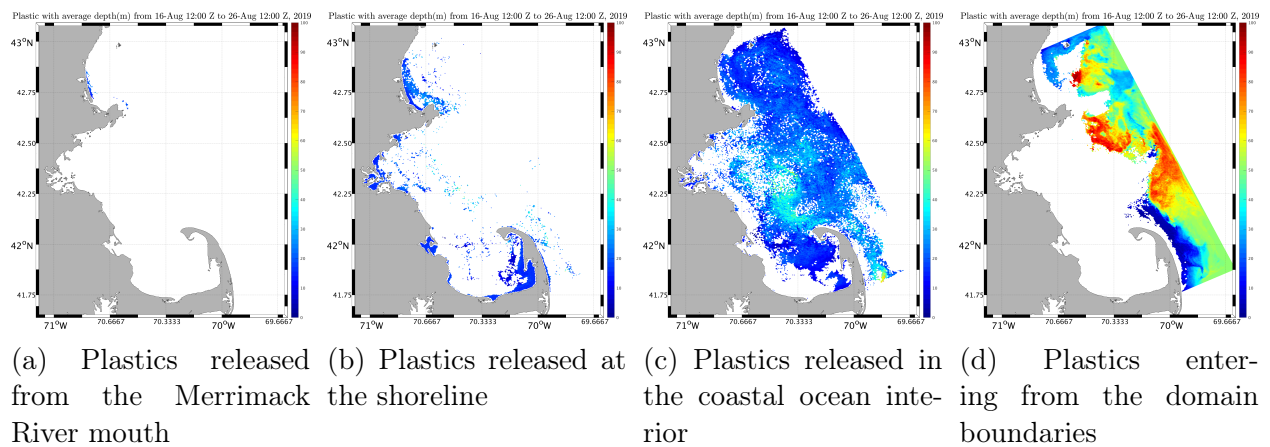
Figure 6.15: Predicted final spatial location and depth of marine plastics after 10 days of advection with settling (Aug. 16–26) when starting within 0–10 m depth, from the: (a) mouth of Merrimack, (b) shoreline, (c) offshore inside domain, and (d) offshore outside. Final location colored by vertically-averaged depth.

Mass. Bay Plastics Predictions: 3D Active Tracers with / without Settling

We now analyze 3D simulations of plastic transport, with and without plastic settling. For this settling, we assume that the plastic settles down homogeneously at a vertical velocity of 1 m/day (based on published values [81, 88, 90, 93]). In reality, plastics of different types and sizes settle at different velocities. Further, the local dynamics (such as the temperature and density) also affects settling velocities.

Plastics are now initialized within a 10 m deep layer at the surface. We highlight the same source regions as before: mouth of Merrimack, beach and nearshore, offshore inside domain, and offshore outside. Fig. 6.15 shows the final plastic positions, but colored with their final vertically-averaged depths, after 10 days of advection and settling.

Most of the plastics that start at the mouth of the Merrimack settle to the bottom near the coast (especially off Plum Island). Some plastics make it as far south as Cape Ann. We find that the majority of the plastics that started nearshore also settle in shallow water. A large portion of that nearshore plastics in western Cape Cod Bay follows the cyclonic flow which develops from the August 24-26 winds (subsection 6.2.3) to end up along the western shore of Cape Cod. A bit of plastics that started nearshore sink deeper in the interior of Mass. Bay. Some of the plastics that start within Mass. Bay, but away from the shore, manage to get closer to the shoreline (following the cyclonic coastal circulation, especially near the South Shore). However, most remain in the interior but sink deeper, especially in Stellwagen Basin where large solitary waves from Stellwagen Bank may bring the plastics to depth where they become entrained in the deeper flows, see Fig. 6.12. Finally, we observe a sizable influx of plastics from outside the domain, mainly from the eastern boundary. These plastics have 3 distinct zones: (i) the ones that end up near the eastern boundary of Cape Cod rise close to the surface (following flows forced up topography, not shown); (ii) the ones at the eastern boundary of the domain settle deeper, around 85 m; and (iii) the others settle at around 50 m. The regions outside Mass. Bay have a general slight bias towards downward ocean vertical velocities at depth in this time period (not shown). The regions

where plastics reach 85 m are regions where internal tides are frequently propagating (not shown), with smaller amplitudes than the solitary waves of Stellwagen Basin but more wide spread. These waves can give an initial downward impetus into the zones with the slight downward bias.

When comparing these results with those from Fig. 6.13, we observe that plastics that started at the mouth of the Merrimack sink before they can exit the domain (as they did in Fig. 6.13). We also find that in the 3D case, the plastics that started off near the coast do not spread as much. They instead accumulate and sink around the attracting ridges at the surface near Cape Cod, indicating subduction. Finally, we also observe that when settling is on, plastics that enter our modeling domain from the outside do not advect west (towards the coast) as much as they did in the case of 2D floating plastics, see Fig. 6.13(b).

Mass. Bay Plastics Observations

There are no sustained comprehensive plastic observation programs in Mass. Bay, but debris and plastic data have been collected in the region off and on in the past decades [150, 159, 171, 204]. In the Gulf of Maine, [76] find that most debris from beach cleanups appear to be from shore-based sources, while commercial fishermen account for half of the ocean-based debris. Overall, the Northeast region, with a limited population growth, has relatively limited land-based and general-source debris loads [173].

Mortimer [150] observed surface debris and humpback whales from 17,700 km of trackline by commercial whale watch vessels during the summer of 2014. These synoptic data indicate that plastic and other floating trash and debris concentrated in several areas, in accord with our modeling results. Plastics were found in the region from the South Shore (e.g. Scituate) to Provincetown, and the southwest corner of Stellwagen Bank, as in Fig. 6.13 and in accord with FTLEs. Another region was around the northwest corner of Stellwagen Bank, but plastics there were more dispersed, again in accord with our simulation results. The MWRA samples the Mass. Bay outfall every year and has completed debris and plastic surveys [171].

They found that much of the surface debris caught in tows were likely advected by wind-driven currents, as in our simulations. Several smaller debris and plastic pieces were also sampled, indicating that microplastics from rivers and offshore sources were also present.

While we have focused on the Massachusetts bay region for our work, global-scale estimates of plastic transports also pose a critical question in the context of plastic cleanup. This is discussed in Lermusiaux et al. [125]

6.2.4 Conclusions

In this work, we outlined our MSEAS coupled data-driven ocean modeling and Lagrangian transport PDE methodology for marine plastics, and showcased results in Mass. Bay.

We showed that our ocean physics predictions had skill by comparison with synoptic data. We predicted the fate of plastics originating from four sources: rivers, nearshore, local Bay, and remote offshore. We showed that the distribution of floating plastics vary in time and space, often in response to wind-driven ocean circulations. However, intermittent preferential locations are likely since wind events tend to be similar. We also found that: (i) Currents set-up by wind events strongly affect floating plastics. Winds can for example prevent Merrimack outflows to reach the Bay; (ii) There is significant chaotic stirring between nearshore and offshore floating plastics as explained by ridges of Lagrangian Coherent Structures (LCSs); (iii) With 4D plastic motions and settling, plastics from the Merrimack and nearshore regions can settle to the seabed before offshore advection; (iv) Internal waves and tides can bring plastics downward and out of main currents, leading to settling to the deep bottom. (v) Attractive LCSs ridges are frequent in the northern Cape Cod Bay, west of the South Shore, and southern Stellwagen Bank. They lead to plastic accumulation and sinking along thin subduction zones. Our study can help guide plastic cleanup strategies in the region.

6.3 Real-time Forecasting of Subduction Pathways and Real-time Bayesian Lagrangian Data Assimilation[3]

In this subsection, we describe our real-time results in the Mediterranean Sea, the forecasts of three-dimensional subduction pathways and the real-time Bayesian assimilation of drifter data. To obtain these results, we employed the stochastic data-assimilative ocean field forecasts and analyses issued in real-time by members of our MIT MSEAS research group as part of the Coherent Lagrangian Pathways from the Surface Ocean to Interior (CALYPSO) Departmental Research Initiative (DRI) [151]. These MSEAS forecasts and analyses were completed during the international multi-university CALYPSO real-time ocean experiments in the Alboran Sea [141, 152] and Balearic Sea [153]. Some of the MSEAS results are described in [66, 67, 147]. For our contributions, for the first time, we predicted three-dimensional subduction pathways of surface waters to intermediate depths in the Alboran Sea in 2019 (section 6.3.2), using three-dimensional PDE-based flow maps [98, 99] and our new developments (see prior sections of this thesis). For our second contribution, for the first time, we assimilated drifter data in the Balearic Sea in 2022 (section 6.3.3) improving forecast skill in real-time, using new Bayesian Eulerian-Lagrangian data assimilation based on the uncertainty quantification and assimilation methods developed in [43, 44, 51] and in Section 4 of this thesis.

6.3.1 Introduction

The CALYPSO initiative aims to describe and quantify the truly three-dimensional and time-dependent transports of ocean properties from the surface ocean to the interior, with a focus on the southwest Mediterranean Sea region [142]. This integrated DRI effort involved many national and international observing and modeling scientists. Many of the research

---

[3]This section is based on [147].

results are based on two real-time ocean experiments.

The 2019 CALYPSO real-time ocean experiment took place during the late winter of 2018-2019 (March 28 to April 11) in the Alboran Sea [152]. The goal of this cruise was to identify transport pathways from the surface into the interior ocean during the late winter in the Alboran sea. Theory and previous observations indicated that these pathways likely originated at strong fronts, such as the one that separates salty Mediterranean water and the fresher water inflowing from the Atlantic [141]. Our specific goal was to map such pathways and quantify their transport (section 6.3.2).

The two-part 2022 CALYPSO ocean experiment occurred in the Balearic Sea from February to June 2022 [153]. In real-time, our MIT-MSEAS group issued multi-resolution deterministic and uncertainty forecasts of ocean fields, as well as Lagrangian flow maps, coherent sets, subduction forecasts, and drifter forecasts.

During the two real-time experiments, nested high-resolution deterministic Eulerian simulations were completed using the MIT Multidisciplinary Simulation, Estimation, and Assimilation System primitive equation (MSEAS-PE) model [64, 65], and stochastic uncertainty predictions were completed using the Error Subspace Statistical Estimation (ESSE) method [112, 115]. At its core, MSEAS-PE is a solver of governing fluid and ocean dynamics equations. It is part of an extensive modeling system for hydrostatic primitive-equation dynamics with a nonlinear free surface, based on second-order structured finite volumes [64]. It is used to study and quantify tidal-to-mesoscale processes over regional domains with complex geometries and varied interactions. The modeling system is used for fundamental research and for realistic simulations and predictions in varied regions of the World Ocean [63, 119, 121, 122, 127, 161, 169]. Its many applications include monitoring [117], real-time acoustic prediction and data assimilation [42, 106, 206], and ecosystem prediction and environmental management [9, 27].

6.3.2 Transport, Flow Maps, and Subduction Pathways in the Alboran Sea

The CALYPSO 2019 experiment occurred in the Alboran Sea from March 26 to April 10, 2019. The specific objectives of our MSEAS group [147, 152] were to: (i) Utilize our new Lagrangian transport theory and methods to forecast, characterize, and quantify ocean processes involved in the three-dimensional transports and transformation of water masses and subduction dynamics in the Alboran Sea; (ii) Apply and expand our multi-resolution submesoscale-to-regional-scale ocean modeling, 2-way nesting, and uncertainty predictions, for real-time forecasting and process studies; (iii) Help design field experiments and predict sampling strategies that maximize information on 4D pathways and dynamics in the region.

To map the transport pathways described above, Lagrangian analyses of the ocean flow are utilized. As opposed to Eulerian descriptors of fluid flow, where properties of fluids are monitored at fixed locations in space, Lagrangian descriptors follow fluid parcels as they move through the flow. One set of descriptors, the forward (backward) flow map, refers to a map from initial (final) positions of passive particles to their final (initial) positions when advected by a fluid flow in a given time interval. Lagrangian coherent structures (LCS), which refer to a robust skeleton of material surfaces that shape the patterns of passive trajectories in the ocean, can be computed using these flow maps [70]. Surface LCS attractors are considered good descriptors of subducting regions [3]. Flow maps are also used to compute subduction maps, the set of points on the surface of the ocean which will be advected below a certain depth under the flow. These maps provide a more direct description of the subducting water masses and their pathways.

The computation of the flow maps, and subsequently the other Lagrangian descriptors, is done using a novel numerical partial differential equation (PDE) based method which uses flow map composition to remove compounding errors [98]. This method has been successfully used to compute flow maps and tracer advection in Massachusetts Bay [125], the Red Sea [40],
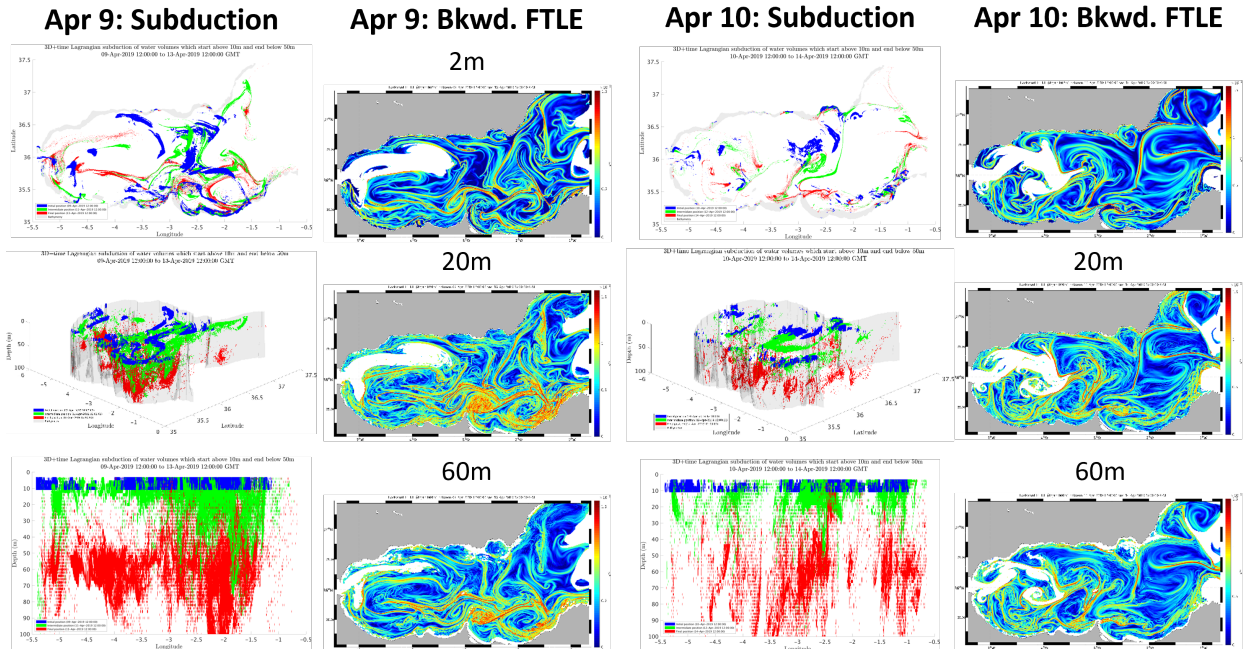
Figure 6.16: Subduction maps and FTLE fields for forecasts issued on April 08 2019

and other domains.

Furthermore, we used the flow map forecasts to compute regions of the ocean near the surface that would subduct in the future. This allowed us to try and infer the underlying ocean dynamics at play by looking at the subduction pathways. Examples of such subduction maps and FTLE fields are given in figure 6.16

6.3.3 Real-time Bayesian Eulerian-Lagrangian Data Assimilation of Drifter Data in the Balearic Sea

The two-part CALYPSO 2022 experiment occurred in the Balearic Sea [153] from February 18 to March 12, 2022 (with modeling work starting February 8) and from March 25 to June 29, 2022 (with modeling work starting on April 13). Specific new capabilities included nested ensemble forecasts downscaled from multiple models, the use of our MSEAS 2D and 3D SeaVizKit visualization tools, and the evaluation of our Lagrangian data assimilation and adaptive sampling in real-time.
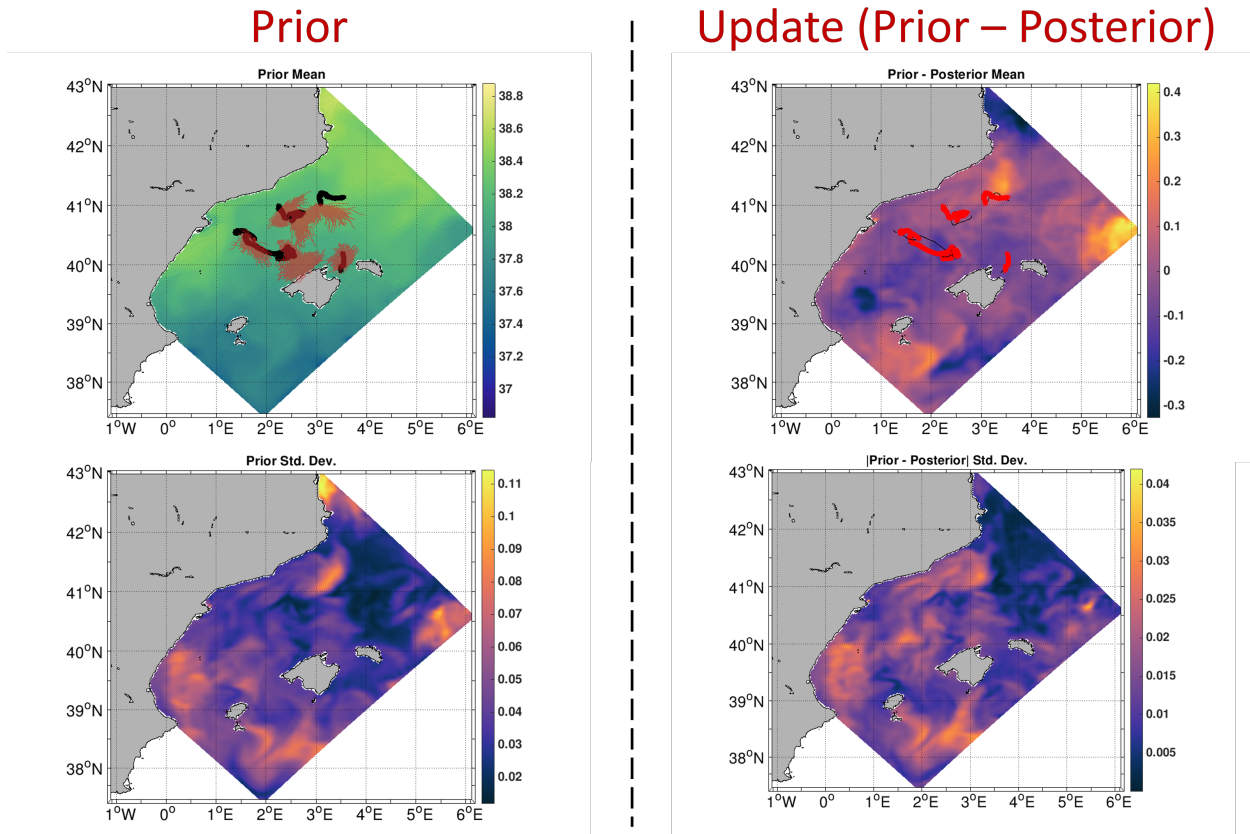
Figure 6.17: Lagrangian Data Assimilation for probabilistic MSEAS-PE forecasts using drifter data in realtime

In collaboration with our MSEAS group, during the experiment and for the first time, we assimilated data from real drifters in the ocean. Members of our research group then issued forecasts starting from our real-time Eulerian-Lagrangian data assimilation results. We found that the forecast skill significantly improved after assimilating this data. These results are summarized in figures 6.17 and 6.18. This assimilation was performed using the GMM-DO filter in an augmented space. We note that the multi-timescale filter was *not* used to assimilate this data. This exercise motivated the derivation of the multi-timescale GMM-DO filter presented in chapter 4.
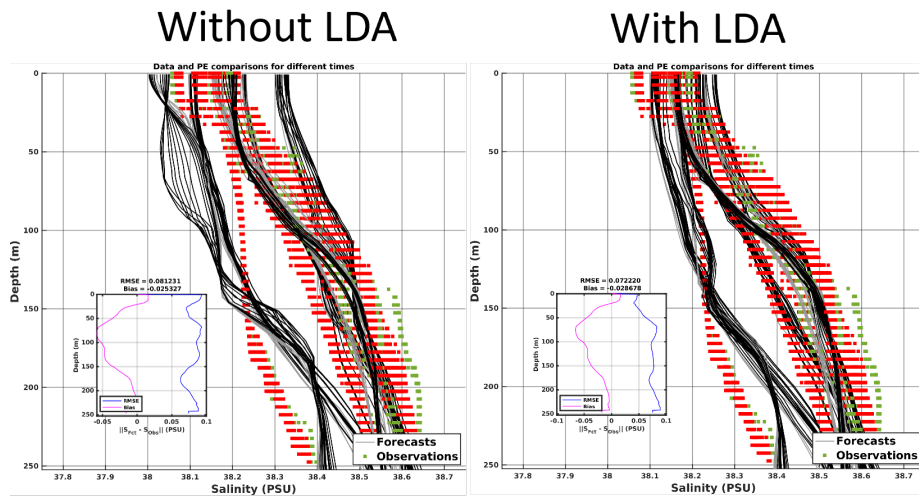
Figure 6.18: Improvement of forecast skill when using fields assimilated by real drifter data

Chapter 7

Conclusions and Future Work

This thesis presented various contributions that were made under the primary goal of developing methods to allow path planning in strong stochastic dynamic ocean environments. In pursuit of this goal, we developed various algorithms for path planning, lagrangian analysis, and data assimilation.

7.1   Summary of Contributions

Optimal Path Planning   We introduced a variety of novel methods for optimal path planning for ocean vehicles with complex mission objectives including time, energy and collection optimality for multiple start and end times all at ones in a time-dependant highly dynamic ocean environment with strong flow.

Lagrangian Data Assimilation   We derived and implemented a novel filtering algorithm aimed at multi-timescale coupled systems in general and specifically for assimilation of data from Lagrangian instruments in the ocean. This approach adeptly addresses the nonlinear dynamics and computational challenges inherent in oceanographic data assimilation, thereby improving the quality of probabilistic ocean forecasts.

Data Assimilative Path Planning   The integration of path planning and LaDA methodologies represents a significant stride towards achieving long-term autonomy for ocean vehicles. This coupled approach enables continuous learning and adaptation to new information, optimizing both the exploration capabilities and the operational efficiency of these vehicles.

Real-World Applications   In collaboration with members of our MSEAS research group, we demonstrated the implementation of various Lagrangian algorithms in real-time ocean experiments and with real ocean data and forecasts.

7.2   Future Work

There are various avenues for future research for each of the contributions discussed.

Optimal Path Planning   One straightforward extension to the work presented in this thesis is to derive and implements multi-time reachability schemes for vehicles with different dynamics (for e.g., floats, sailboats). Another extension of our work could be implementing our energy optimal schemes for vehicles that can harvest wind, wave, tidal and other sources of energy from their environment.

Lagrangian Data Assimilation   The novel filtering algorithm presented in chapter 4 can be extended to other multi-timescale coupled systems such as a coupled weather-climate model, coupled biology-ocean dynamics systems, etc., . The proposed filter can also be extended to coupled dynamical systems with more than two dynamical systems. By choosing different filtering schemes for various marginal and conditional distributions one can potentially derive similar filtering schemes tailored to the properties of the various dynamical systems.

Data Assimilative Path Planning   Extensions to the work we presented include implementing POMDP-like tree search approaches when evaluating the maximization term in the

Hamilton-Jacobi-Bellman term, exploring risk-optimal and robust path planning strategies as opposed to minimizing expected time and exploring strategies to minimize on-board compute and communication costs to implement this scheme for a realistic low-powered ocean vehicle.

Appendix A

Equations for Gaussian Mixture Models

A.1 Weighted Expectation Maximization

The weighted expectation maximization algoritm for fitting a GMM is very similar to the expectation maximization algorithm with the exception that the weights are taken into account in the expectation step when computing the likelihood that a datapoint x_i comes from mixture j. The algorithm is summarized in algorithm box 2

As with [189], we can use the Bayesian information criteria (BIC) to obtain the optimal number of mixture components.

A.2 Conditionals of GMMs

Consider a GMM in the space of $\begin{bmatrix} x \\ y \end{bmatrix}$ characterized by the mixture coefficients, means, and covariances $\left\{ \pi_k, \begin{bmatrix} \boldsymbol{\mu}_{x,k} \\ \boldsymbol{\mu}_{y,k} \end{bmatrix}, \begin{bmatrix} \boldsymbol{\Sigma}_{xx,k} & \boldsymbol{\Sigma}_{xy,k} \\ \boldsymbol{\Sigma}_{yx,k} & \boldsymbol{\Sigma}_{yy,k} \end{bmatrix} \right\}_{k=1}^{K}$. The objective is to compute the conditional distribution $p(\boldsymbol{y}|\boldsymbol{x})$.

In a hierarchical GMM framework, a latent categorical variable Z determines the com-

---

Algorithm 2: Weighted Expectation Maximization for GMM

Result: Parameters of the GMM: $\{\pi_k, \mu_k, \Sigma_k\}_{k=1}^{K}$

Initialize the number of components K;

Initialize π_k, μ_k, Σ_k for all k randomly or using something like the k-means algorithm;

Start with data points x_i and corresponding weights w_i;

while *not converged* **do**

    // E-Step: Compute responsibilities

    for *each data point i* **do**

        for *each component k* **do**

            $\gamma(z_{ik}) = \frac{w_i \pi_k \mathcal{N}(x_i | \mu_k, \Sigma_k)}{\sum_{j=1}^{K} w_i \pi_j \mathcal{N}(x_i | \mu_j, \Sigma_j)}$;

        end

    end

    // M-Step: Update parameters

    for *each component k* **do**

        $\pi_k = \frac{\sum_{i=1}^{N} \gamma(z_{ik})}{\sum_{i=1}^{N} w_i}$;

        $\mu_k = \frac{\sum_{i=1}^{N} \gamma(z_{ik}) x_i}{\sum_{i=1}^{N} \gamma(z_{ik})}$;

        $\Sigma_k = \frac{\sum_{i=1}^{N} \gamma(z_{ik})(x_i - \mu_k)(x_i - \mu_k)^T}{\sum_{i=1}^{N} \gamma(z_{ik})}$;

    end

    // Check for convergence

    Check if the log-likelihood of the data under the model has converged;

end

---

ponent from which a data point is sampled. For each component $Z = k$, data points are generated from a multivariate Gaussian distribution $\mathcal{N}(\boldsymbol{\mu}_k, \boldsymbol{\Sigma}_k)$. The conditional distribution $p(\boldsymbol{y}|\boldsymbol{x})$ can be expressed as a mixture of the component-specific conditional distributions, weighted by the posterior probabilities of Z given $\boldsymbol{x}$:

$$p(\boldsymbol{y}|\boldsymbol{x}) = \sum_{k=1}^{K} p(\boldsymbol{y}|\boldsymbol{x}, Z = k)p(Z = k|\boldsymbol{x}) \tag{A.1}$$

$$= \sum_{k=1}^{K} \mathcal{N}(\boldsymbol{y}; \boldsymbol{\mu}_{y|x,k}, \boldsymbol{\Sigma}_{y|x,k})p(Z = k|\boldsymbol{x}) \tag{A.2}$$

where $p(Z = k|\boldsymbol{x})$ is the posterior probability of component k given $\boldsymbol{x}$, computed as:

$$p(Z = k|\boldsymbol{x}) = \frac{\pi_k \mathcal{N}(\boldsymbol{x}; \boldsymbol{\mu}_{x,k}, \boldsymbol{\Sigma}_{xx,k})}{\sum_{j=1}^{K} \pi_j \mathcal{N}(\boldsymbol{x}; \boldsymbol{\mu}_{x,j}, \boldsymbol{\Sigma}_{xx,j})} \tag{A.3}$$

The parameters of the component-specific conditional distributions are given by:

$$\boldsymbol{\mu}_{y|x,k} = \boldsymbol{\mu}_{y,k} + \boldsymbol{\Sigma}_{yx,k}\boldsymbol{\Sigma}_{xx,k}^{-1}(\boldsymbol{x} - \boldsymbol{\mu}_{x,k}) \tag{A.4}$$

$$\boldsymbol{\Sigma}_{y|x,k} = \boldsymbol{\Sigma}_{yy,k} - \boldsymbol{\Sigma}_{yx,k}\boldsymbol{\Sigma}_{xx,k}^{-1}\boldsymbol{\Sigma}_{xy,k} \tag{A.5}$$

This formulation leverages the hierarchical structure of the GMM, where the latent variable Z guides the mixture component selection, and the conditional distribution within each component follows a Gaussian distribution parameterized by the adjusted means and covariances. One can use a very similar approach to compute posterior GMMs under a linear observation model. A detailed derivation for computing the posterior can be found in Sondergaard and Lermusiaux [189].

A.3　Marginals of GMMs

Consider a GMM in the space of $\begin{bmatrix} \boldsymbol{x} \\ \boldsymbol{y} \end{bmatrix}$ characterized by mixture coefficients, means, and covariances $\left\{ \pi_k, \begin{bmatrix} \boldsymbol{\mu}_{x,k} \\ \boldsymbol{\mu}_{y,k} \end{bmatrix}, \begin{bmatrix} \boldsymbol{\Sigma}_{xx,k} & \boldsymbol{\Sigma}_{xy,k} \\ \boldsymbol{\Sigma}_{yx,k} & \boldsymbol{\Sigma}_{yy,k} \end{bmatrix} \right\}_{k=1}^{K}$. The goal of this section is to derive the marginal distribution $p(\boldsymbol{x})$, which involves integrating out the variable $\boldsymbol{y}$ from the joint distribution.

The marginal distribution of $\boldsymbol{x}$ in a GMM is a mixture of the marginal distributions of $\boldsymbol{x}$ for each component, weighted by the mixture coefficients. For each component k, the marginal distribution of $\boldsymbol{x}$ is a Gaussian distribution with mean $\boldsymbol{\mu}_{x,k}$ and covariance $\boldsymbol{\Sigma}_{xx,k}$. Therefore, the marginal distribution $p(\boldsymbol{x})$ can be expressed as:

$$p(\boldsymbol{x}) = \sum_{k=1}^{K} \pi_k \mathcal{N}(\boldsymbol{x}; \boldsymbol{\mu}_{x,k}, \boldsymbol{\Sigma}_{xx,k}) \tag{A.6}$$

This expression shows that the marginal distribution of $\boldsymbol{x}$ is a weighted sum of the Gaussian distributions for $\boldsymbol{x}$ in each component of the GMM, with weights given by the mixture coefficients π_k. The mean and covariance of $\boldsymbol{x}$ in each component come directly from the parameters of the GMM associated with $\boldsymbol{x}$, without the need to perform any integration explicitly.

References

[1] A. Agarwal and P. F. J. Lermusiaux. Statistical field estimation for complex coastal regions and archipelagos. *Ocean Modelling*, 40(2):164–189, 2011. doi:10.1016/j.ocemod.2011.08.001.

[2] V. Akçelik, G. Biros, O. Ghattas, K. R. Long, and B. van Bloemen Waanders. A variational finite element method for source inversion for convective–diffusive transport. *Finite Elements in Analysis and Design*, 39(8):683–705, 2003.

[3] Michael Allshouse and HM Aravind. Predicting regions of ocean vertical transport via surface coherent structures. In *APS Division of Fluid Dynamics Meeting Abstracts*, pages H39–002, 2019.

[4] Amit Apte, Christopher KRT Jones, and A. M. Stuart. A Bayesian approach to Lagrangian data assimilation. *Tellus A: Dynamic Meteorology and Oceanography*, 60 (2):336–347, 2008. Publisher: Taylor & Francis.

[5] Anil Aswani, Humberto Gonzalez, S Shankar Sastry, and Claire Tomlin. Provably safe and robust learning-based model predictive control. *Automatica*, 49(5):1216–1226, 2013.

[6] Saeed Asadi Bagloee, Madjid Tavana, Mohsen Asadi, and Tracey Oliver. Autonomous vehicles: challenges, opportunities, and future implications for transportation policies. *Journal of modern transportation*, 24(4):284–303, 2016.

[7] Somil Bansal, Mo Chen, Sylvia Herbert, and Claire J Tomlin. Hamilton-jacobi reachability: A brief overview and recent advances. In *2017 IEEE 56th Annual Conference on Decision and Control (CDC)*, pages 2242–2253. IEEE, 2017.

[8] Alexandre M Bayen, Ian M Mitchell, Meeko MK Oishi, and Claire J Tomlin. Aircraft autolander safety analysis through optimal control-based reach set computation. *Journal of Guidance, Control, and Dynamics*, 30(1):68–77, 2007.

[9] Ş. T. Beşiktepe, P. F. J. Lermusiaux, and A. R. Robinson. Coupled physical and biogeochemical data-driven simulations of Massachusetts Bay in late summer: Real-time and post-cruise data assimilation. *Journal of Marine Systems*, 40–41:171–212, 2003. doi:10.1016/S0924-7963(03)00018-6.

[10] Thomas Bengtsson, Chris Snyder, and Doug Nychka. Toward a nonlinear ensemble filter for high-dimensional systems. *Journal of Geophysical Research: Atmospheres*, 108(D24), 2003. ISSN 2156-2202. doi:10.1029/2002JD002900. URL https://onlinelibrary.wiley.com/doi/abs/10.1029/2002JD002900. _eprint: https://onlinelibrary.wiley.com/doi/pdf/10.1029/2002JD002900.

[11] Melanie Bergmann, Sophia Mützel, Sebastian Primpke, Mine B Tekman, Jürg Trachsel, and Gunnar Gerdts. White and wonderful? Microplastics prevail in snow from the Alps to the Arctic. *Science Advances*, 5(8):eaax1157, 2019.

[12] Dimitri Bertsekas. *Dynamic programming and optimal control: Volume I*, volume 1. Athena scientific, 2012.

[13] Manmeet S. Bhabra and Pierre F. J. Lermusiaux. Stochastic dynamically orthogonal acoustic wavefront equations. In preparation, 2024.

[14] Manmeet S. Bhabra, Manan Doshi, Benjamin C. Koenig, Patrick J. Haley, Jr., C. Mirabito, Pierre F. J. Lermusiaux, C. A. Goudey, J. Curcio, D. Manganelli, and H. Goudey. Optimal harvesting with autonomous tow vessels for offshore macroalgae farming. In *OCEANS 2020 IEEE/MTS*, pages 1–10. IEEE, October 2020. doi:10.1109/IEEECONF38699.2020.9389474.

[15] Manmeet Singh Bhabra. Harvest-time optimal path planning in dynamic flows. Master's thesis, Massachusetts Institute of Technology, Department of Mechanical Engineering and Computational Science & Engineering, Cambridge, Massachusetts, September 2021.

[16] Olivier Bokanowski and Hasnaa Zidani. Minimal time problems with moving targets and obstacles. *IFAC Proceedings Volumes*, 44(1):2589–2593, 2011. ISSN 1474-6670. doi:https://doi.org/10.3182/20110828-6-IT-1002.02261. 18th IFAC World Congress.

[17] Olivier Bokanowski, Nicolas Forcadel, and Hasnaa Zidani. Reachability and minimal times for state constrained nonlinear problems without any controllability assumption. *SIAM J. on Control and Optim.*, 48(7):4292–4316, 2010. doi:10.1137/090762075.

[18] James Bradbury, Roy Frostig, Peter Hawkins, Matthew James Johnson, Chris Leary, Dougal Maclaurin, George Necula, Adam Paszke, Jake VanderPlas, Skye Wanderman-Milne, and Qiao Zhang. JAX: composable transformations of Python+NumPy programs, 2018.

[19] M. Carlu, F. Ginelli, V. Lucarini, and A. Politi. Lyapunov analysis of multi-scale dynamics: the slow bundle of the two-scale lorenz 96 model. *Nonlinear Processes in Geophysics*, 26(2):73–89, 2019. doi:10.5194/npg-26-73-2019. URL https://npg.copernicus.org/articles/26/73/2019/.

[20] James Carpenter, Peter Clifford, and Paul Fearnhead. Improved particle filter for nonlinear problems. *IEE Proceedings-Radar, Sonar and Navigation*, 146(1):2–7, 1999.

[21] Alberto Carrassi, Marc Bocquet, Laurent Bertino, and Geir Evensen. Data assimilation in the geosciences: An overview of methods, issues, and perspectives. *WIREs Climate Change*, 9(5):e535, 2018. ISSN 1757-7799. doi:10.1002/wcc.535. URL https://onlinelibrary.wiley.com/doi/abs/10.1002/wcc.535. _eprint: https://onlinelibrary.wiley.com/doi/pdf/10.1002/wcc.535.

[22] Mo Chen and Claire J Tomlin. Hamilton–jacobi reachability: Some recent theoretical advances and applications in unmanned airspace management. *Annual Review of Control, Robotics, and Autonomous Systems*, 1:333–358, 2018.

[23] Mo Chen, Sylvia L Herbert, Mahesh S Vashishtha, Somil Bansal, and Claire J Tomlin.

Decomposition of reachable sets and tubes for a class of nonlinear systems. *IEEE Transactions on Automatic Control*, 63(11):3675–3688, 2018.

[24] Yan Chen, Weimin Zhang, and Mengbin Zhu. A localized weighted ensemble kalman filter for high-dimensional systems. *Quarterly Journal of the Royal Meteorological Society*, 146(726):438–453, 2020. doi:https://doi.org/10.1002/qj.3685. URL https://rmets.onlinelibrary.wiley.com/doi/abs/10.1002/qj.3685.

[25] D. L. Codiga. Unified Tidal Analysis and Prediction Using the UTide Matlab Functions. GSO Technical Report 2011-01, Graduate School of Oceanography, U. of Rhode Island, 2011. URL ftp://www.po.gso.uri.edu/pub/downloads/codiga/pubs/2011Codiga-UTide-Report.pdf.

[26] M. E. G. D. Colin, T. F. Duda, L. A. te Raa, T. van Zon, P. J. Haley, Jr., P. F. J. Lermusiaux, W. G. Leslie, C. Mirabito, F. P. A. Lam, A. E. Newhall, Y.-T. Lin, and J. F. Lynch. Time-evolving acoustic propagation modeling in a complex ocean environment. In *OCEANS - Bergen, 2013 MTS/IEEE*, pages 1–9, 2013. doi:10.1109/OCEANS-Bergen.2013.6608051.

[27] G. Cossarini, P. F. J. Lermusiaux, and C. Solidoro. Lagoon of Venice ecosystem: Seasonal dynamics and environmental guidance with uncertainty analyses and error subspace data assimilation. *Journal of Geophysical Research: Oceans*, 114(C6), June 2009. doi:10.1029/2008JC005080.

[28] J. Coulin, P. J. Haley, Jr., S. Jana, C. S. Kulkarni, P. F. J. Lermusiaux, and T. Peacock. Environmental ocean and plume modeling for deep sea mining in the Bismarck Sea. In *Oceans 2017 - Anchorage*, Anchorage, AK, September 2017.

[29] A. Cózar, F. Echevarría, J I. González-Gordillo, X. Irigoien, B. Úbeda, S. Hernández-León, A. T. Palma, S. Navarro, J. García-de Lomas, A. Ruiz, et al. Plastic debris in the open ocean. *Proc. of the National Academy of Sciences*, 111(28):10239–10244, 2014.

[30] James A. Cummings and Ole Martin Smedstad. *Variational Data Assimilation for the Global Ocean*, pages 303–343. Springer Berlin Heidelberg, Berlin, Heidelberg, 2013. doi:10.1007/978-3-642-35088-7_13.

[31] B. Cushman-Roisin and J.M. Beckers. *Introduction to Geophysical Fluid Dynamics. Physical and Numerical aspects*, volume 101. Academic Press, Waltham, MA, 2011.

[32] Wessam Z. Daoud, Jonathan D. W. Kahl, and Jugal K. Ghorai. On the Synoptic-Scale Lagrangian Autocorrelation Function. *Journal of Applied Meteorology and Climatology*, 42(2):318–324, February 2003. ISSN 1520-0450, 0894-8763. doi:10.1175/1520-0450(2003)042<0318:OTSSLA>2.0.CO;2. URL https://journals.ametsoc.org/view/journals/apme/42/2/1520-0450_2003_042_0318_otssla_2.0.co_2.xml. Publisher: American Meteorological Society Section: Journal of Applied Meteorology and Climatology.

[33] Michela De Dominicis, Silvia Falchetti, Francesco Trotta, Nadia Pinardi, Luca Giacomelli, Ernesto Napolitano, Leopoldo Fazioli, Roberto Sorgente, Patrick J. Haley, Jr., Pierre F. J. Lermusiaux, F. Martins, and M. Cocco. A relocatable ocean

model in support of environmental emergencies. *Ocean Dynamics*, 64(5):667–688, 2014. doi:10.1007/s10236-014-0705-x.

[34] D. P. Dee, S. M. Uppala, A. J. Simmons, P. Berrisford, P. Poli, S. Kobayashi, U. Andrae, M. A. Balmaseda, G. Balsamo, P. Bauer, P. Bechtold, A. C.M. Beljaars, L. van de Berg, J. Bidlot, N. Bormann, C. Delsol, R. Dragani, M. Fuentes, A. J. Geer, L. Haimberger, S. B. Healy, H. Hersbach, E. V. Hólm, L. Isaksen, P. Kållberg, M. Köhler, M. Matricardi, A. P. Mcnally, B. M. Monge-Sanz, J. J. Morcrette, B. K. Park, C. Peubey, P. de Rosnay, C. Tavolato, J. N. Thépaut, and F. Vitart. The ERA-Interim reanalysis: Configuration and performance of the data assimilation system. *Quarterly Journal of the Royal Meteorological Society*, 2011. ISSN 00359009. doi:10.1002/qj.828.

[35] Jerry Ding, Jonathan Sprinkle, S Shankar Sastry, and Claire J Tomlin. Reachability calculations for automated aerial refueling. In *47th IEEE Conf. on Dec. & Con.*, pages 3706–3712. IEEE, 2008.

[36] Petar M Djuric, Jayesh H Kotecha, Jianqui Zhang, Yufei Huang, Tadesse Ghirmai, Mónica F Bugallo, and Joaquin Miguez. Particle filtering. *IEEE signal processing magazine*, 20(5):19–38, 2003.

[37] Manan Doshi. Energy-time optimal path planning in strong dynamic flows. Master's thesis, Massachusetts Institute of Technology, Center for Computational Science and Engineering, Cambridge, Massachusetts, February 2021.

[38] Manan Doshi and Pierre F. J. Lermusiaux. Split GMM schemes for coupled multi-timescale dynamical systems: Application to Lagrangian data assimilation. *Monthly Weather Review*, 2024. In preparation.

[39] Manan Doshi, Manmeet Bhabra, Marius Wiggert, Claire J. Tomlin, and Pierre F. J. Lermusiaux. Hamilton–Jacobi multi-time reachability. In *2022 IEEE 61st Conference on Decision and Control (CDC)*, pages 2443–2450, Cuncún, Mexico, December 2022. doi:10.1109/CDC51059.2022.9993328.

[40] Manan M. Doshi, Chinmay S. Kulkarni, Wael Hajj Ali, Abhinav Gupta, Pierre F. J. Lermusiaux, Peng Zhan, Ibrahim Hoteit, and Omar Knio. Flow maps and coherent sets for characterizing residence times and connectivity in lagoons and coral reefs: The case of the Red Sea. In *OCEANS 2019 MTS/IEEE SEATTLE*, pages 1–8, Seattle, October 2019. IEEE. doi:10.23919/OCEANS40490.2019.8962643.

[41] Manan M. Doshi, Manmeet S. Bhabra, and Pierre F. J. Lermusiaux. Energy-time optimal path planning in dynamic flows: Theory and schemes. *Computer Methods in Applied Mechanics and Engineering*, 405:115865, February 2023. doi:10.1016/j.cma.2022.115865.

[42] Timothy F. Duda, Ying-Tsong Lin, W. Zhang, Bruce D. Cornuelle, and Pierre F. J. Lermusiaux. Computational studies of three-dimensional ocean sound fields in areas of complex seafloor topography and active ocean dynamics. In *Proceedings of the 10th International Conference on Theoretical and Computational Acoustics*, Taipei, 2011.

[43] Arkopal Dutt. High order stochastic transport and Lagrangian data assimilation. Master's thesis, Massachusetts Institute of Technology, Department of Mechanical Engineering, Cambridge, Massachusetts, February 2018.

[44] Arkopal Dutt, Deepak N. Subramani, Chinmay S. Kulkarni, and Pierre F. J. Lermusiaux. Clustering of massive ensemble of vehicle trajectories in strong, dynamic and uncertain ocean flows. In *OCEANS Conference 2018*, Charleston, SC, October 2018. IEEE. doi:10.1109/OCEANS.2018.8604634.

[45] Gary D. Egbert and Svetlana Y. Erofeeva. Efficient inverse modeling of barotropic ocean tides. *Journal of Atmospheric and Oceanic Technology*, 19(2):183–204, 2002. doi:10.1175/1520-0426(2002)019<0183:EIMOBO>2.0.CO;2.

[46] Gary D. Egbert and Svetlana Y. Erofeeva. OSU tidal inversion. http://volkov.oce.orst.edu/tides/tpxo8_atlas.html, 2013.

[47] M. Eriksen, L.C.M. Lebreton, H.S. Carson, M. Thiel, C.J. Moore, J.C. Borerro, F. Galgani, P.G. Ryan, and J. Reisser. Plastic pollution in the world's oceans: more than 5 trillion plastic pieces weighing over 250,000 tons afloat at sea. *PloS one*, 9(12):e111913, 2014.

[48] L.C. Evans. *Partial Differential Equations*. Graduate studies in mathematics. American Mathematical Society, 2010. ISBN 9780821849743.

[49] Geir Evensen. The ensemble kalman filter: Theoretical formulation and practical implementation. *Ocean dynamics*, 53:343–367, 2003.

[50] Florian Feppon and Pierre F. J. Lermusiaux. A geometric approach to dynamical model-order reduction. *SIAM Journal on Matrix Analysis and Applications*, 39(1):510–538, 2018. doi:10.1137/16M1095202.

[51] Florian Feppon and Pierre F. J. Lermusiaux. Dynamically orthogonal numerical schemes for efficient stochastic advection and Lagrangian transport. *SIAM Review*, 60(3):595–625, 2018. doi:10.1137/16M1109394.

[52] Florian Feppon and Pierre F. J. Lermusiaux. Rigid sets and coherent sets in realistic ocean flows. *Nonlinear Processes in Geophysics*, 2024. doi:10.5194/npg-2022-1. Sub-judice.

[53] J. E. Fernandez, A. C. Graham, et al. Microfibers and microplastics: Pursuing a life-cycle approach to solutions. *MIT*, pages 1–2, 2018.

[54] Jaime F Fisac, Mo Chen, Claire J Tomlin, and S Shankar Sastry. Reach-avoid problems with time-varying dynamics, targets and constraints. In *Proc. of the 18th international conference on hybrid systems: computation and control*, pages 11–20, 2015.

[55] Dario Floreano and Robert J Wood. Science, technology and the future of small autonomous drones. *Nature*, 521(7553):460–466, 2015.

[56] Gary Froyland, Simon Lloyd, and Naratip Santitissadeekorn. Coherent sets for nonautonomous dynamical systems. *Physica D: Nonlinear Phenomena*, 239(16):1527–1541, 2010.

[57] Avijit Gangopadhyay, Pierre F.J. Lermusiaux, Leslie Rosenfeld, Allan R. Robinson, Leandro Calado, Hyun Sook Kim, Wayne G. Leslie, and Patrick J. Haley, Jr. The California Current system: A multiscale overview and the development of a feature-oriented regional modeling system (FORMS). *Dynamics of Atmospheres and Oceans*, 52(1–2):131–169, September 2011. doi:10.1016/j.dynatmoce.2011.04.003. Special issue of Dynamics of Atmospheres and Oceans in honor of Prof. A. R. Robinson.

[58] G. Gawarkiewicz, S. Jan, P. F. J. Lermusiaux, J. L. McClean, L. Centurioni, K. Taylor, B. Cornuelle, T. F. Duda, J. Wang, Y. J. Yang, T. Sanford, R.-C. Lien, C. Lee, M.-A. Lee, W. Leslie, P. J. Haley, Jr., P. P. Niiler, G. Gopalakrishnan, P. Velez-Belchi, D.-K. Lee, and Y. Y. Kim. Circulation and intrusions northeast of Taiwan: Chasing and predicting uncertainty in the cold dome. *Oceanography*, 24(4):110–121, 2011. doi:10.5670/oceanog.2011.99.

[59] Arthur Gelb et al. *Applied optimal estimation*. MIT press, 1974.

[60] Annalisa Griffa, AD Kirwan Jr, Arthur J Mariano, Tamay Özgökmen, and H Thomas Rossby. *Lagrangian analysis and prediction of coastal and ocean dynamics*. Cambridge University Press, 2007.

[61] Gwyn Griffiths. *Technology and applications of autonomous underwater vehicles*, volume 2. CRC Press, 2002.

[62] Alireza Hadjighasem, Mohammad Farazmand, Daniel Blazevski, Gary Froyland, and George Haller. A critical comparison of lagrangian methods for coherent structure detection. *Chaos: An Interdisciplinary Journal of Nonlinear Science*, 27(5):053104, 2017.

[63] P. J. Haley, Jr., P. F. J. Lermusiaux, A. R. Robinson, W. G. Leslie, O. Logoutov, G. Cossarini, X. S. Liang, P. Moreno, S. R. Ramp, J. D. Doyle, J. Bellingham, F. Chavez, and S. Johnston. Forecasting and reanalysis in the Monterey Bay/California Current region for the Autonomous Ocean Sampling Network-II experiment. *Deep Sea Research Part II: Topical Studies in Oceanography*, 56(3–5):127–148, February 2009. doi:10.1016/j.dsr2.2008.08.010.

[64] Patrick J. Haley, Jr. and Pierre F. J. Lermusiaux. Multiscale two-way embedding schemes for free-surface primitive equations in the "Multidisciplinary Simulation, Estimation and Assimilation System". *Ocean Dynamics*, 60(6):1497–1537, December 2010. doi:10.1007/s10236-010-0349-4.

[65] Patrick J. Haley, Jr., Arpit Agarwal, and Pierre F. J. Lermusiaux. Optimizing velocities and transports for complex coastal regions and archipelagos. *Ocean Modelling*, 89:1–28, May 2015. doi:10.1016/j.ocemod.2015.02.005.

[66] Patrick J. Haley, Jr., Pierre F. J. Lermusiaux, Chris Mirabito, Manan Doshi, Kyprianos A. Gkirgkis, Wael Hajj Ali, Chinmay Kulkarni, and Abhinav Gupta. Process studies in the Alboran Sea during the CALYPSO real-time sea experiment 2019. In preparation, 2024.

[67] Patrick J. Haley, Jr., Pierre F. J. Lermusiaux, Chris Mirabito, Manan Doshi, Kyprianos A. Gkirgkis, Wael Hajj Ali, Chinmay Kulkarni, and Abhinav Gupta. The CALYPSO real-time Balearic Sea experiment 2022. In preparation, 2024.

[68] G. Haller and T. Sapsis. Where do inertial particles go in fluid flows? *Physica D: Nonlin. Phen.*, 237(5):573–583, 2008.

[69] George Haller. A variational theory of hyperbolic Lagrangian Coherent Structures. *Physica D: Nonlinear Phenomena*, 240(7):574–598, March 2011. ISSN 0167-2789. doi:10.1016/j.physd.2010.11.010. URL https://www.sciencedirect.com/science/article/pii/S0167278910003143.

[70] George Haller. Lagrangian coherent structures. *Annual Review of Fluid Mechanics*, 47:137–162, 2015.

[71] George Haller, Alireza Hadjighasem, Mohammad Farazmand, and Florian Huhn. Defining coherent vortices objectively from the vorticity. *Journal of Fluid Mechanics*, 795:136–173, 2016.

[72] Kevin D. Heaney, Glen Gawarkiewicz, Timothy F. Duda, and Pierre F. J. Lermusiaux. Nonlinear optimization of autonomous undersea vehicle sampling strategies for oceanographic data-assimilation. *Journal of Field Robotics*, 24(6):437–448, 2007. ISSN 1556-4967. doi:10.1002/rob.20183.

[73] Kevin D. Heaney, Pierre F. J. Lermusiaux, Timothy F. Duda, and Patrick J. Haley, Jr. Validation of genetic algorithm based optimal sampling for ocean data assimilation. *Ocean Dynamics*, 66:1209–1229, 2016. doi:10.1007/s10236-016-0976-5.

[74] Fabrice Hernandez, Pierre-Yves Le Traon, and Norman H. Barth. Optimizing a Drifter Cast Strategy with a Genetic Algorithm. *Journal of Atmospheric and Oceanic Technology*, 12(2):330–345, April 1995. ISSN 0739-0572, 1520-0426. doi:10.1175/1520-0426(1995)012<0330:OADCSW>2.0.CO;2. URL https://journals.ametsoc.org/view/journals/atot/12/2/1520-0426_1995_012_0330_oadcsw_2_0_co_2.xml. Publisher: American Meteorological Society Section: Journal of Atmospheric and Oceanic Technology.

[75] Jan S Hesthaven and Tim Warburton. *Nodal discontinuous Galerkin methods: algorithms, analysis, and applications*. Springer Science & Business Media, 2007.

[76] Porter Hoagland and Hauke L. Kite-Powell. Characterization and mitigation of marine debris in the Gulf of Maine. Technical report, WHOI, Duxbury, MA, October 1997.

[77] Geoffrey A. Hollinger, Arvind A. Pereira, Jonathan Binney, Thane Somers, and Gaurav S. Sukhatme. Learning uncertainty in ocean current predictions for safe and reliable navigation of underwater vehicles. *Journal of Field Robotics*, 33(1):47–66, 2016. doi:https://doi.org/10.1002/rob.21613. URL https://onlinelibrary.wiley.com/doi/abs/10.1002/rob.21613.

[78] Haomiao Huang, Jerry Ding, Wei Zhang, and Claire J Tomlin. A differential game approach to planning in adversarial scenarios: A case study on capture-the-flag. In *2011 IEEE Int. Conf. on Robotics and Automation*, pages 1451–1456. IEEE, 2011.

[79] Kayo Ide, Leonid Kuznetsov, and Christopher KRT Jones. Lagrangian data assimilation for point vortex systems. *Journal of Turbulence*, 3(1):053, 2002. Publisher: IOP Publishing.

[80] Iho Ioc. BODC, 2003. Centenary Edition of the GEBCO Digital Atlas, published on CD-ROM on behalf of the Intergovernmental Oceanographic Commission and the International Hydrographic Organization as part of the General Bathymetric Chart of the Oceans. *British oceanographic data centre, Liverpool*, 2008.

[81] Igor Isachenko, Liliya Khatmullina, Irina Chubarenko, and Natalia Stepanova. Settling velocity of marine microplastic particles: laboratory tests. April 2016.

[82] Yoichi Ishikawa, Tochiyuki Awaji, Kazunori Akitomo, and Bo Qiu. Successive Correction of the Mean Sea Surface Height by the Simultaneous Assimilation

of Drifting Buoy and Altimetric Data. *Journal of Physical Oceanography*, 26 (11):2381–2397, November 1996. ISSN 0022-3670, 1520-0485. doi:10.1175/1520-0485(1996)026<2381:SCOTMS>2.0.CO;2. URL https://journals.ametsoc.org/view/journals/phoc/26/11/1520-0485_1996_026_2381_scotms_2_0_co_2.xml. Publisher: American Meteorological Society Section: Journal of Physical Oceanography.

[83] A. Jahnke, H. P. H. Arp, B. I. Escher, B. Gewert, E. Gorokhova, D. Kühnel, M. Ogonowski, A. Potthoff, C. Rummel, M. Schmitt-Jansen, et al. Reducing uncertainty and confronting ignorance about the possible impacts of weathering plastic in the marine environment. *Environmental Science & Technology Letters*, 4(3):85–90, 2017.

[84] H S Jiang, T Farrar, R C Beardsley, R Chen, and C S Chen. Zonal surface wind jets across the Red Sea due to mountain gap forcing along both sides of the Red Sea. *Geophysical Research Letters*, 36, 2009. doi:Artn L19605 Doi 10.1029/2009gl040008.

[85] S. Kako, A. Isobe, S. Seino, and A. Kojima. Inverse estimation of drifting-object outflows using actual observation data. *Journal of oceanography*, 66(2):291–297, 2010.

[86] S. Kako, A. Isobe, S. Magome, H. Hinata, S. Seino, and A. Kojima. Establishment of numerical beach-litter hindcast/forecast models: An application to Goto Islands, Japan. *Marine pollution bulletin*, 62(2):293–302, 2011.

[87] Rudolph Emil Kalman. A new approach to linear filtering and prediction problems. *Transactions of the ASME–Journal of Basic Engineering*, 82(Series D):35–45, 1960.

[88] I. A. Kane and M. A. Clare. Dispersion, Accumulation, and the Ultimate Fate of Microplastics in Deep-Marine Environments: A Review and Future Directions. *Front. in Earth Sc.*, 7, 2019. ISSN 2296-6463. doi:10.3389/feart.2019.00080. URL https://www.frontiersin.org/articles/10.3389/feart.2019.00080/full.

[89] S. M. Kelly and P. F. J. Lermusiaux. Internal-tide interactions with Gulf Stream and Middle Atlantic Bight shelfbreak front. *Journal of Geophysical Research: Oceans*, 121: 6271–6294, 2016. doi:10.1002/2016JC011639.

[90] Liliya Khatmullina and Igor Isachenko. Settling velocity of microplastic particles of regular shapes. *Marine Pollution Bulletin*, 114(2):871–880, January 2017. ISSN 0025-326X. doi:10.1016/j.marpolbul.2016.11.024. URL http://www.sciencedirect.com/science/article/pii/S0025326X16309201.

[91] Donald E Kirk. *Optimal control theory: an introduction*. Courier Corporation, 2004.

[92] A. A Koelmans, M. Kooi, K. L. Law, and E. Van Sebille. All is not lost: deriving a top-down mass budget of plastic at sea. *Environmental Research Letters*, 12(11): 114028, 2017.

[93] M. Kooi, J. Reisser, B. Slat, F. F. Ferrari, M. S. Schmid, S. Cunsolo, R. Brambini, K. Noble, L.-A. Sirks, T. E. W. Linders, R. I. Schoeneich-Argent, and A. A. Koelmans. The effect of particle properties on the depth profile of buoyant plastics in the ocean. *Scientific Reports*, 6, October 2016. ISSN 2045-2322. doi:10.1038/srep33882. URL https://www.ncbi.nlm.nih.gov/pmc/articles/PMC5056413/.

[94] J.H. Kotecha and P.M. Djuric. Gaussian particle filtering. *IEEE Transactions on Signal Processing*, 51(10):2592–2601, 2003. doi:10.1109/TSP.2003.816758.

[95] J.H. Kotecha and P.M. Djuric. Gaussian sum particle filtering. *IEEE Transactions on Signal Processing*, 51(10):2602–2612, 2003. doi:10.1109/TSP.2003.816754.

[96] T Kukulka, G Proskurowski, S Morét-Ferguson, DW Meyer, and KL Law. The effect of wind mixing on the vertical distribution of buoyant plastic debris. *Geophysical Res. Letters*, 39(7), 2012.

[97] C. S. Kulkarni, P. J. Haley, Jr., P. F. J. Lermusiaux, A. Dutt, A. Gupta, C. Mirabito, D. N. Subramani, S. Jana, W. H. Ali, T. Peacock, C. M. Royo, A. Rzeznik, and R. Supekar. Real-time sediment plume modeling in the Southern California Bight. In *OCEANS Conference 2018*, Charleston, SC, October 2018. IEEE. doi:10.1109/OCEANS.2018.8653642.

[98] Chinmay S. Kulkarni and Pierre F. J. Lermusiaux. Advection without compounding errors through flow map composition. *Journal of Computational Physics*, 398:108859, December 2019. doi:10.1016/j.jcp.2019.108859.

[99] Chinmay S. Kulkarni and Pierre F. J. Lermusiaux. Persistent Lagrangian material coherence in fluid and ocean flows using flow map composition. *Ocean Modelling*, 2024. Sub-judice.

[100] Chinmay Sameer Kulkarni. *Prediction, Analysis, and Learning of Advective Transport in Dynamic Fluid Flows*. PhD thesis, Massachusetts Institute of Technology, Department of Mechanical Engineering and Center for Computational Science and Engineering, Cambridge, Massachusetts, February 2021.

[101] Pijush K. Kundu, Ira M. Cohen, and David R. Dowling. *Fluid Mechanics*. Elsevier, 2012.

[102] Hanna Kurniawati. Partially observable markov decision processes and robotics. *Annual Review of Control, Robotics, and Autonomous Systems*, 5(1):253–277, 2022. doi:10.1146/annurev-control-042920-092451. URL https://doi.org/10.1146/annurev-control-042920-092451.

[103] A. B. Kurzhanski and P. Varaiya. Ellipsoidal techniques for reachability under state constraints. *SIAM Journal on Control and Optimization*, 45(4):1369–1394, 2006. doi:10.1137/S0363012903437605.

[104] Alexander B Kurzhanski and Pravin Varaiya. Dynamic optimization for reachability problems. *J. of Optimization Theory and Applications*, 108(2):227–251, 2001.

[105] L. Kuznetsov, K. Ide, and C. K. R. T. Jones. A Method for Assimilation of Lagrangian Data. *Monthly Weather Review*, 131(10):2247–2260, October 2003. ISSN 1520-0493, 0027-0644. doi:10.1175/1520-0493(2003)131<2247:AMFAOL>2.0.CO;2. URL https://journals.ametsoc.org/view/journals/mwre/131/10/1520-0493_2003_131_2247_amfaol_2.0.co_2.xml. Publisher: American Meteorological Society Section: Monthly Weather Review.

[106] Frans-Peter A. Lam, Patrick J. Haley, Jr., Jeroen Janmaat, Pierre F. J. Lermusiaux, Wayne G. Leslie, Mathijs W. Schouten, Lianke A. te Raa, and Michel Rixen. At-sea real-time coupled four-dimensional oceanographic and acoustic forecasts during Battlespace Preparation 2007. *Journal of Marine Systems*, 78(Supplement):S306–S320, November 2009. doi:10.1016/j.jmarsys.2009.01.029.

[107] Sabique Langodan, Luigi Cavaleri, Yesubabu Vishwanadhapalli, Angela Pomaro, Luciana Bertotti, and Ibrahim Hoteit. The climatology of the Red Sea – part 1: the wind. *International Journal of Climatology*, 2017. ISSN 10970088. doi:10.1002/joc.5103.

[108] Kara Lavender Law. Plastics in the marine environment. *Annual Review of Marine Science*, 9:205–229, 2017.

[109] Kara Lavender Law and Richard C Thompson. Microplastics in the seas. *Science*, 345 (6193):144–145, 2014.

[110] L Lebreton, B Slat, F Ferrari, B Sainte-Rose, J Aitken, R Marthouse, S Hajbane, Serena Cunsolo, A Schwarz, A Levivier, et al. Evidence that the Great Pacific Garbage Patch is rapidly accumulating plastic. *Scientific reports*, 8(1):4666, 2018.

[111] John J. Leonard and Alexander Bahr. *Autonomous Underwater Vehicle Navigation*, pages 341–358. Springer International Publishing, Cham, 2016. ISBN 978-3-319-16649-0. doi:10.1007/978-3-319-16649-0_14. URL https://doi.org/10.1007/978-3-319-16649-0_14.

[112] P. F. J. Lermusiaux. Estimation and study of mesoscale variability in the Strait of Sicily. *Dynamics of Atmospheres and Oceans*, 29(2):255–303, 1999. doi:10.1016/S0377-0265(99)00008-1.

[113] P. F. J. Lermusiaux. Evolving the subspace of the three-dimensional multiscale ocean variability: Massachusetts Bay. *Journal of Marine Systems*, 29(1):385–422, 2001. doi:10.1016/S0924-7963(01)00025-2.

[114] P. F. J Lermusiaux. Adaptive modeling, adaptive data assimilation and adaptive sampling. *Physica D: Nonlinear Phenomena*, 230(1):172–196, 2007. doi:10.1016/j.physd.2007.02.014.

[115] P. F. J. Lermusiaux, C.-S. Chiu, and A. R. Robinson. Modeling uncertainties in the prediction of the acoustic wavefield in a shelfbreak environment. In E.-C. Shang, Q. Li, and T. F. Gao, editors, *Proceedings of the 5th International Conference on Theoretical and Computational Acoustics*, pages 191–200. World Scientific Publishing Co., May 21-25 2002. doi:10.1142/9789812777362_0020. Refereed invited manuscript.

[116] P. F. J. Lermusiaux, C.-S. Chiu, G. G. Gawarkiewicz, P. Abbot, A. R. Robinson, R. N. Miller, P. J. Haley, Jr, W. G. Leslie, S. J. Majumdar, A. Pang, and F. Lekien. Quantifying uncertainties in ocean predictions. *Oceanography*, 19(1):92–105, 2006. doi:10.5670/oceanog.2006.93.

[117] P. F. J Lermusiaux, P. J. Haley, Jr, and N. K. Yilmaz. Environmental prediction, path planning and adaptive sampling: Sensing and modeling for efficient ocean monitoring, management and pollution control. *Sea Technology*, 48(9):35–38, 2007.

[118] P. F. J. Lermusiaux, P. J. Haley, W. G. Leslie, A. Agarwal, O. Logutov, and L. J. Burton. Multiscale physical and biological dynamics in the Philippine Archipelago: Predictions and processes. *Oceanography*, 24(1):70–89, 2011. doi:10.5670/oceanog.2011.05. Special Issue on the Philippine Straits Dynamics Experiment.

[119] P. F. J Lermusiaux, A. J. Miller, and N. Pinardi. Special issue of Dynamics of Atmospheres and Oceans in honor of Prof. A. R. Robinson. *Dynamics of Atmospheres and Oceans*, 52(1–2):1–3, September 2011. doi:10.1016/j.dynatmoce.2011.08.001. Editorial.

[120] P. F. J. Lermusiaux, T. Lolla, P. J. Haley, Jr., K. Yigit, M. P. Ueckermann, T. Sondergaard, and W. G. Leslie. Science of autonomy: Time-optimal path planning and adaptive sampling for swarms of ocean vehicles. In Tom Curtin, editor, *Springer Handbook of Ocean Engineering: Autonomous Ocean Vehicles, Subsystems and Control*, chapter 21, pages 481–498. Springer, 2016. doi:10.1007/978-3-319-16649-0_21.

[121] P. F. J. Lermusiaux, P. J. Haley, Jr., S. Jana, A. Gupta, C. S. Kulkarni, C. Mirabito, W. H. Ali, D. N. Subramani, A. Dutt, J. Lin, A. Shcherbina, C. Lee, and A. Gangopadhyay. Optimal planning and sampling predictions for autonomous and Lagrangian platforms and sensors in the northern Arabian Sea. *Oceanography*, 30(2):172–185, June 2017. doi:10.5670/oceanog.2017.242. Special issue on Autonomous and Lagrangian Platforms and Sensors (ALPS).

[122] P. F. J. Lermusiaux, D. N. Subramani, J. Lin, C. S. Kulkarni, A. Gupta, A. Dutt, T. Lolla, P. J. Haley, Jr., W. H. Ali, C. Mirabito, and S. Jana. A future for intelligent autonomous ocean observing systems. *Journal of Marine Research*, 75(6):765–813, November 2017. doi:10.1357/002224017823524035. The Sea. Volume 17, The Science of Ocean Prediction, Part 2.

[123] Pierre F. J. Lermusiaux and A. R. Robinson. Data assimilation via Error Subspace Statistical Estimation, part I: Theory and schemes. *Monthly Weather Review*, 127(7): 1385–1407, 1999. doi:10.1175/1520-0493(1999)127<1385:DAVESS>2.0.CO;2.

[124] Pierre F. J. Lermusiaux, Jinshan Xu, Chi-Fang Chen, Sen Jan, L.Y. Chiu, and Yiing-Jang Yang. Coupled ocean–acoustic prediction of transmission loss in a continental shelfbreak region: Predictive skill, uncertainty quantification, and dynamical sensitivities. *IEEE Journal of Oceanic Engineering*, 35(4):895–916, October 2010. doi:10.1109/JOE.2010.2068611.

[125] Pierre F. J. Lermusiaux, Manan Doshi, Chinmay S. Kulkarni, Abhinav Gupta, Patrick J. Haley, Jr., Chris Mirabito, Francesco Trotta, S. J. Levang, G. R. Flierl, J. Marshall, Thomas Peacock, and C. Noble. Plastic pollution in the coastal oceans: Characterization and modeling. In *OCEANS 2019 MTS/IEEE SEATTLE*, pages 1–10, Seattle, October 2019. IEEE. doi:10.23919/OCEANS40490.2019.8962786.

[126] Pierre F. J. Lermusiaux, Patrick J. Haley, Jr., Glen G. Gawarkiewicz, and Sen Jan. Evaluation of multiscale ocean probabilistic forecasts: Quantifying, predicting and exploiting uncertainty. *Ocean Dynamics*, 2024. In preparation.

[127] W. G. Leslie, A. R. Robinson, P. J. Haley, Jr, O. Logutov, P. A. Moreno, P. F. J. Lermusiaux, and E. Coelho. Verification and training of real-time forecasting of multiscale ocean dynamics for maritime rapid environmental assessment. *Journal of Marine Systems*, 69(1):3–16, 2008. doi:10.1016/j.jmarsys.2007.02.001.

[128] Weiwei Liao and Tao Liang. Computation of reachable sets based on hamilton-jacobi-bellman equation with running cost function, 2021.

[129] Jing Lin and Pierre F. J. Lermusiaux. Bayesian learning of turbulent bottom gravity currents models. In preparation, 2024.

[130] O. G. Logutov and P. F. J. Lermusiaux. Inverse barotropic tidal estimation for regional ocean applications. *Ocean Modelling*, 25(1–2):17–34, 2008. ISSN 1463-

5003. doi:10.1016/j.ocemod.2008.06.004. URL http://www.sciencedirect.com/science/article/pii/S1463500308000851.

[131] T. Lolla and P. F. J. Lermusiaux. A Gaussian mixture model smoother for continuous nonlinear stochastic dynamical systems: Theory and scheme. *Monthly Weather Review*, 145:2743–2761, July 2017. doi:10.1175/MWR-D-16-0064.1.

[132] T. Lolla and Pierre F. J. Lermusiaux. A forward reachability equation for minimum-time path planning in strong dynamic flows. MSEAS Report 27, Department of Mechanical Engineering, Massachusetts Institute of Technology, Cambridge, MA, USA, 2017.

[133] T. Lolla, P. J. Haley, Jr., and P. F. J. Lermusiaux. Time-optimal path planning in dynamic flows using level set equations: Realistic applications. *Ocean Dynamics*, 64 (10):1399–1417, 2014. doi:10.1007/s10236-014-0760-3.

[134] T. Lolla, P. F. J. Lermusiaux, M. P. Ueckermann, and P. J. Haley, Jr. Time-optimal path planning in dynamic flows using level set equations: Theory and schemes. *Ocean Dynamics*, 64(10):1373–1397, 2014. doi:10.1007/s10236-014-0757-y.

[135] T. Lolla, P. J. Haley, Jr., and P. F. J. Lermusiaux. Path planning in multiscale ocean flows: Coordination and dynamic obstacles. *Ocean Modelling*, 94:46–66, 2015. doi:10.1016/j.ocemod.2015.07.013.

[136] Tapovan Lolla, Mattheus P. Ueckermann, Konur Yiğit, Patrick J. Haley, Jr., and Pierre F. J. Lermusiaux. Path planning in time dependent flow fields using level set methods. In *IEEE International Conference on Robotics and Automation (ICRA), 14-18 May 2012*, pages 166–173, 2012. doi:10.1109/ICRA.2012.6225364.

[137] Harvard Lomax, Thomas H Pulliam, and David W Zingg. *Fundamentals of computational fluid dynamics*. Springer Science & Business Media, 2013.

[138] Edward N Lorenz. Predictability: A problem partly solved. In *Proc. Seminar on predictability*, volume 1. Reading, 1996.

[139] R Lumpkin and L Centurioni. Global drifter program quality-controlled 6-hour interpolated data from ocean surface drifting buoys. noaa national centers for environmental information. dataset, 2019.

[140] Rick Lumpkin, Mayra Pazos, et al. Measuring surface currents with surface velocity program drifters: the instrument, its data, and some recent results. *Lagrangian analysis and prediction of coastal and ocean dynamics*, 39:67, 2007.

[141] Amala Mahadevan, Eric D'Asaro, John Allen, Pablo Almaraz García, Eva Alou-Font, Harilal Meenambika Aravind, Pau Balaguer, Isabel Caballero, Noemi Calafat, Andrea Carbornero, Benjamin Casas, Carlos Castilla, Luca Centurioni, Margaret Conley, Gino Cristofano, Eugenio Cutolo, Mathieu Dever, Angélica Enrique Navarro, Francesco M. Falcieri, Mara Freilich, Evan Goodwin, Raymond Graham, Cedric Guigand, Ben Hodges, Helga Huntley, Shaun Johnston, Matthias Lankhorst, Pierre Lermusiaux, Irene Lizaran, Chris Mirabito, A. Miralles, Baptiste Mourre, Gabriel Navarro, Michael Ohmart, Said Ouala, Tamay Özgökmen, Ananda Pascual, Joan Horrach Pou, Pierre-Marie Poulain, Alice Ren, Daniel Rodríguez Tarry, Dan Rudnick, M. Rubio, Simón Ruiz, Irina Rypina, Joaquín Tintoré, Uwe Send, Andrey Shcherbina, M. Torner, Guil-

herme Salvador Vieira, Nikolaus Wirth, and Nikolaos Zarokanellos. CALYPSO 2019 cruise report: Field campaign in the Mediterranean. Technical Report WHOI-2020-02, Woods Hole Oceanographic Institution, Woods Hole, MA, January 2020.

[142] Amala Mahadevan, Ananda Pascual, Daniel L Rudnick, Simón Ruiz, Joaquín Tintoré, and Eric D'Asaro. Calypso. *Bulletin of the American Meteorological Society*, 102(6): 532–540, 2021.

[143] Andrew J. Majda, Di Qi, and Themistoklis P. Sapsis. Blended particle filters for large-dimensional chaotic dynamical systems. *Proceedings of the National Academy of Sciences*, 111(21):7511–7516, May 2014. doi:10.1073/pnas.1405675111. URL https://www.pnas.org/doi/abs/10.1073/pnas.1405675111. Publisher: Proceedings of the National Academy of Sciences.

[144] Gianandrea Mannarini, Deepak N. Subramani, Pierre F. J. Lermusiaux, and Nadia Pinardi. Graph-search and differential equations for time-optimal vessel route planning in dynamic ocean waves. *IEEE Transactions on Intelligent Transportation Systems*, 21(6):1–13, June 2020. doi:10.1109/TITS.2019.2935614.

[145] John Marshall, Chris Hill, Lev Perelman, and Alistair Adcroft. Hydrostatic, quasi-hydrostatic, and nonhydrostatic ocean modeling. *Journal of Geophysical Research*, 102(C3):5733, 1997. ISSN 0148-0227. doi:10.1029/96JC02776.

[146] Robert N. Miller. Topics in data assimilation: Stochastic processes. *Physica D: Nonlinear Phenomena*, 230(1):17–26, 2007. ISSN 0167-2789. doi:https://doi.org/10.1016/j.physd.2006.07.015. URL https://www.sciencedirect.com/science/article/pii/S0167278906002600. Data Assimilation.

[147] Chris Mirabito, Patrick J. Haley, Jr., Manan Doshi, Kyprianos Gkirgkis, Wael Hajj Ali, Chinmay Kulkarni, Abhinav Gupta, Pierre F. J. Lermusiaux, Amala Mahadevan, Mara Freilich, Mathieu Dever, Shaun Johnston, Tamay Özgökmen, Larry Pratt, Irina Rypina, Dan Rudnick, Andrey Shcherbina, Craig McNeil, Ruth Musgrave, Sutanu Sarkar, Luca Centurioni, Eric D'Asaro, James McWilliams, Peter Sullivan, Helga Huntley, Denny Kirwan, Tom Farrar, Annalisa Griffa, Uwe Send, Matthias Lankhorst, Michael Allshouse, Thomas Peacock, Pierre-Marie Poulain, Simón Ruiz, Ananda Pascual, Joaquín Tintoré, John Allen, Baptiste Mourre, Eva Alou-Font, Nikolaos Zarakanellos, Cristian Muñoz, Inma Ruiz, and Alexandra Z. Worden. Real-time high-resolution probabilistic Eulerian and Lagrangian forecasting in the Alboran Sea: Skill, subduction, and multi-downscaling ensemble predictions. *Ocean Modelling*, 2024. In preparation.

[148] Ian M Mitchell et al. A toolbox of level set methods. *UBC Department of Computer Science Technical Report TR-2007-11*, page 31, 2007.

[149] Anne Molcard, Leonid I. Piterbarg, Annalisa Griffa, Tamay M. Özgökmen, and Arthur J. Mariano. Assimilation of drifter observations for the reconstruction of the Eulerian circulation field. *Journal of Geophysical Research: Oceans*, 108(C3), 2003. ISSN 2156-2202. doi:10.1029/2001JC001240. URL https://onlinelibrary.wiley.com/doi/abs/10.1029/2001JC001240. _eprint: https://onlinelibrary.wiley.com/doi/pdf/10.1029/2001JC001240.

[150] T. A. L. Mortimer. Risk in the urban ocean: Mapping marine debris and feeding

humpback whales (Megaptera novaeangliae) in the Stellwagen Bank Nat. Mar. Sanct. Poster, December 2015.

[151] MSEAS CALYPSO. Coherent Lagrangian pathways from the surface ocean to interior (CALYPSO) project, November 2018. URL http://mseas.mit.edu/Research/CALYPSO/.

[152] MSEAS CALYPSO Ex. CALYPSO real-time sea experiment 2019: Alboran Sea – March - April 2019, April 2019. URL http://mseas.mit.edu/Sea_exercises/CALYPSO/2019/.

[153] MSEAS CALYPSO Ex. CALYPSO real-time Balearic Sea experiment 2022: Balearic Sea – February - June 2022, June 2022. URL http://mseas.mit.edu/Sea_exercises/CALYPSO/2022/.

[154] MSEAS (Multidisciplinary Simulation, Estimation, and Assimilation Systems) Group. Software, August 2011. URL http://mseas.mit.edu/software/.

[155] Kevin Murphy and Stuart Russell. *Rao-Blackwellised Particle Filtering for Dynamic Bayesian Networks*, pages 499–515. Springer New York, New York, NY, 2001. ISBN 978-1-4757-3437-9. doi:10.1007/978-1-4757-3437-9_24. URL https://doi.org/10.1007/978-1-4757-3437-9_24.

[156] National Centers for Environmental Prediction (NCEP). North American Mesoscale Forecast System (NAM). https://www.emc.ncep.noaa.gov/index.php?branch=NAM, September 2019.

[157] National Data Buoy Center (NDBC). https://www.ndbc.noaa.gov/, September 2019.

[158] National Marine Fisheries Service. https://www.nefsc.noaa.gov/HydroAtlas/, August 2019.

[159] National Oceanic and Atmospheric Administration (NOAA). 2018 NOAA Marine Debris program accomplishments report. Technical report, NOAA, October 2018. URL https://marinedebris.noaa.gov.

[160] National Oceanic and Atmospheric Administration (NOAA). Tides and currents. https://tidesandcurrents.noaa.gov/cdata/StationList?type=Current+Data&filter=historic, 2019.

[161] Reiner Onken, Allan R. Robinson, Pierre F. J. Lermusiaux, Patrick J. Haley, and Larry A. Anderson. Data-driven simulations of synoptic circulation and transports in the Tunisia-Sardinia-Sicily region. *Journal of Geophysical Research: Oceans*, 108(C9), 2003. doi:10.1029/2002JC001348.

[162] Stanley Osher and Ronald P Fedkiw. *Level set methods and dynamic implicit surfaces*, volume 1. Springer New York, 2005.

[163] Yulin Pan, Patrick J. Haley, Jr., and Pierre F. J. Lermusiaux. Interactions of internal tides with a heterogeneous and rotational ocean. *Journal of Fluid Mechanics*, 920:A18, August 2021. doi:10.1017/jfm.2021.423.

[164] Nicolas Papadakis, Étienne Mémin, Anne Cuzol, and Nicolas Gengembre. Data assimilation with the weighted ensemble kalman filter. *Tellus A: Dynamic Meteorology and Oceanography*, 62(5):673–697, 2010.

[165] Thomas Peacock and George Haller. Lagrangian coherent structures: The hidden skeleton of fluid flows. *Physics today*, 66(2):41–47, 2013.

[166] Arvind A. Pereira, Jonathan Binney, Geoffrey A. Hollinger, and Gaurav S. Sukhatme. Risk-aware path planning for autonomous underwater vehicles using predictive ocean models. *Journal of Field Robotics*, 30(5):741–762, 2013. doi:https://doi.org/10.1002/rob.21472. URL https://onlinelibrary.wiley.com/doi/abs/10.1002/rob.21472.

[167] Eduardo Pereira, Marcos Tieppo, João Faria, Douglas Hart, Pierre Lermusiaux, and The K2D Project Team. Subsea cables as enablers of a next generation global ocean sensing system. *Oceanography*, 36(Supp. 1), February 2023. doi:10.5670/oceanog.2023.s1.22. Special issue: "Frontiers in Ocean Observing: Emerging Technologies for Understanding and Managing a Changing Ocean".

[168] Dionysios E. Raitsos, Robert J. W. Brewin, Peng Zhan, Denis Dreano, Yaswant Pradhan, Gerrit B. Nanninga, and Ibrahim Hoteit. Sensing coral reef connectivity pathways from space. *Scientific Reports*, 7(1):9338, August 2017. ISSN 2045-2322. doi:10.1038/s41598-017-08729-w. URL https://www.nature.com/articles/s41598-017-08729-w.

[169] Steven R. Ramp, Pierre F. J. Lermusiaux, Igor Shulman, Yi Chao, Rebecca E. Wolf, and Frederick L. Bahr. Oceanographic and atmospheric conditions on the continental shelf north of the Monterey Bay during August 2006. *Dynamics of Atmospheres and Oceans*, 52(1–2):192–223, September 2011. doi:10.1016/j.dynatmoce.2011.04.005. Special issue of Dynamics of Atmospheres and Oceans in honor of Prof. A. R. Robinson.

[170] Najeeb M. A. Rasul. Lagoon Sediments of the Eastern Red Sea: Distribution Processes, Pathways and Patterns. In Najeeb M.A. Rasul and Ian C.F. Stewart, editors, *The Red Sea: The Formation, Morphology, Oceanography and Environment of a Young Ocean Basin*, Springer Earth System Sciences, pages 281–316. Springer Berlin Heidelberg, Berlin, Heidelberg, 2015. ISBN 978-3-662-45201-1. doi:10.1007/978-3-662-45201-1_17. URL https://doi.org/10.1007/978-3-662-45201-1_17.

[171] A. C. Rex and M. F. Delaney. Summary of marine debris observations at MWRA's Deer Island Treatment Plant effluent discharge site in Massachusetts Bay: 2000–2012. Report 2013-01, Massachusetts Water Resources Authority, Boston, 2013.

[172] Maria Isabel Ribeiro. Kalman and extended kalman filters: Concept, derivation and properties. *Institute for Systems and Robotics*, 43(46):3736–3741, 2004.

[173] C. A. Ribic, S. B. Sheavly, D. J. Rugg, and E. S. Erdmann. Trends and drivers of marine debris on the Atlantic coast of the United States: 1997–2007. *Mar. Pol. Bul.*, 60:1231–1242, 2010. doi:10.1016/j.marpolbul.2010.03.021.

[174] Michel Rixen, Pierre F. J. Lermusiaux, and John Osler. Quantifying, predicting, and exploiting uncertainties in marine environments. *Ocean Dynamics*, 62(3):495–499, 2012. doi:10.1007/s10236-012-0526-8.

[175] Allan R. Robinson and Pierre F. J. Lermusiaux. Data assimilation for modeling and predicting coupled physical–biological interactions in the sea. In Allan R. Robinson, James J. McCarthy, and Brian J. Rothschild, editors, *Biological-Physical Interactions*

in the Sea, volume 12 of *The Sea*, chapter 12, pages 475–536. John Wiley and Sons, New York, 2002.

[176] Daniel L Rudnick, Russ E Davis, Charles C Eriksen, David M Fratantoni, and Mary Jane Perry. Underwater gliders for ocean research. *Marine Technology Society Journal*, 38(2):73–84, 2004.

[177] H. Salman. A hybrid grid/particle filter for Lagrangian data assimilation. I: Formulating the passive scalar approximation. *Quarterly Journal of the Royal Meteorological Society*, 134(635):1539–1550, 2008. ISSN 1477-870X. doi:10.1002/qj.270. URL https://onlinelibrary.wiley.com/doi/abs/10.1002/qj.270. _eprint: https://onlinelibrary.wiley.com/doi/pdf/10.1002/qj.270.

[178] H. Salman, L. Kuznetsov, C. K. R. T. Jones, and K. Ide. A method for assimilating lagrangian data into a shallow-water-equation ocean model. *Monthly Weather Review*, 134(4):1081 – 1101, 2006. doi:https://doi.org/10.1175/MWR3104.1. URL https://journals.ametsoc.org/view/journals/mwre/134/4/mwr3104.1.xml.

[179] T. Sapsis and G. Haller. Inertial particle dynamics in a hurricane. *J. of the Atmospheric Sciences*, 66(8):2481–2492, 2009.

[180] Themistoklis P. Sapsis and Pierre F. J. Lermusiaux. Dynamically orthogonal field equations for continuous stochastic dynamical systems. *Physica D: Nonlinear Phenomena*, 238(23–24):2347–2360, December 2009. doi:10.1016/j.physd.2009.09.017.

[181] Themistoklis P. Sapsis and Pierre F. J. Lermusiaux. Dynamical criteria for the evolution of the stochastic dimensionality in flows with uncertainty. *Physica D: Nonlinear Phenomena*, 241(1):60–76, 2012. doi:10.1016/j.physd.2011.10.001.

[182] Simo Särkkä and Arno Solin. *Applied stochastic differential equations*, volume 10. Cambridge University Press, 2019.

[183] Ed Schmerling. hj_reachability - Online, 2022.

[184] Henrik Schmidt, James G Bellingham, Mark Johnson, David Herold, David M Farmer, and Richard Pawlowicz. Real-time frontal mapping with auvs in a coastal environment. In *OCEANS 96 MTS/IEEE Conference Proceedings. The Coastal Ocean-Prospects for the 21st Century*, volume 3, pages 1094–1098. IEEE, 1996.

[185] O. Schofield, S. Glenn, J. Orcutt, M. Arrott, M. Meisinger, A. Gangopadhyay, W. Brown, R. Signell, M. Moline, Y. Chao, S. Chien, D. Thompson, A. Balasuriya, P. F. J. Lermusiaux, and M. Oliver. Automated sensor networks to advance ocean science. *Eos Trans. AGU*, 91(39):345–346, September 2010. doi:10.1029/2010EO390001.

[186] Chi-Wang Shu. High order numerical methods for time dependent hamilton-jacobi equations. In *Mathematics and computation in imaging science and information processing*, pages 47–91. World Sc., 2007.

[187] Boyan Slat. *How the Oceans Can Clean Themselves: A Feasibility Study*. Ocean Cleanup, 2014.

[188] Laura Slivinski, Elaine Spiller, Amit Apte, and Björn Sandstede. A hybrid particle–ensemble Kalman filter for Lagrangian data assimilation. *Monthly Weather Review*, 143(1):195–211, 2015. Publisher: American Meteorological Society.

[189] T. Sondergaard and P. F. J. Lermusiaux. Data assimilation with Gaussian Mixture Models using the Dynamically Orthogonal field equations. Part I: Theory and scheme. *Monthly Weather Review*, 141(6):1737–1760, 2013. doi:10.1175/MWR-D-11-00295.1.

[190] D. N. Subramani and P. F. J. Lermusiaux. Energy-optimal path planning by stochastic dynamically orthogonal level-set optimization. *Ocean Modeling*, 100:57–77, 2016. doi:10.1016/j.ocemod.2016.01.006.

[191] D. N. Subramani, Q. J. Wei, and P. F. J. Lermusiaux. Stochastic time-optimal path-planning in uncertain, strong, and dynamic flows. *Computer Methods in Applied Mechanics and Engineering*, 333:218–237, 2018. doi:10.1016/j.cma.2018.01.004.

[192] Deepak N. Subramani and Pierre F. J. Lermusiaux. Risk-optimal path planning in stochastic dynamic environments. *Computer Methods in Applied Mechanics and Engineering*, 353:391–415, August 2019. doi:10.1016/j.cma.2019.04.033.

[193] Wei Sun, Panagiotis Tsiotras, Tapovan Lolla, Deepak N. Subramani, and Pierre F. J. Lermusiaux. Multiple-pursuer-one-evader pursuit evasion game in dynamic flow fields. *Journal of Guidance, Control and Dynamics*, 40(7), April 2017. doi:10.2514/1.G002125.

[194] The Economist. *https://www.economist.com/technology-quarterly/2018-03-10/ocean-technology*, 2018.

[195] M. K. Tippett, J. L. Anderson, C. H. Bishop, T. M. Hamill, and J. S. Whitaker. Ensemble square root filters. *Monthly Weather Review*, 131:1485–1490, 2003.

[196] E. R. Twomey and R. P. Signell. Construction of a 3-arcsecond digital elevation model for the Gulf of Maine. Open-File Report 2011–1127, U.S. Geological Survey, 2013. URL https://pubs.usgs.gov/of/2011/1127/.

[197] M. P. Ueckermann and P. F. J. Lermusiaux. 2.29 Finite Volume MATLAB Framework Documentation. MSEAS Report 14, Department of Mechanical Engineering, Massachusetts Institute of Technology, Cambridge, MA, 2012. URL http://mseas.mit.edu/?p=2567.

[198] M. P. Ueckermann and P. F. J. Lermusiaux. Hybridizable discontinuous Galerkin projection methods for Navier–Stokes and Boussinesq equations. *Journal of Computational Physics*, 306:390–421, 2016. doi:10.1016/j.jcp.2015.11.028.

[199] M. P. Ueckermann, P. F. J. Lermusiaux, and T. P. Sapsis. Numerical schemes for dynamically orthogonal equations of stochastic fluid and ocean flows. *Journal of Computational Physics*, 233:272–294, January 2013. doi:10.1016/j.jcp.2012.08.041.

[200] Mattheus P. Ueckermann, Chris Mirabito, Patrick J. Haley, Jr., and Pierre F. J. Lermusiaux. High order hybridizable discontinuous Galerkin projection schemes for non-hydrostatic physical-biogeochemical ocean modeling. *Ocean Dynamics*, 2024. In preparation.

[201] Peter Jan Van Leeuwen, Hans R Künsch, Lars Nerger, Roland Potthast, and Sebastian Reich. Particle filters for high-dimensional geoscience applications: A review. *Quarterly Journal of the Royal Meteorological Society*, 145(723):2335–2365, 2019.

[202] Yesubabu Viswanadhapalli, Hari Prasad Dasari, Sabique Langodan, Venkata Srinivas Challa, and Ibrahim Hoteit. Climatic features of the Red Sea from a regional

assimilative model. *International Journal of Climatology*, 2017. ISSN 10970088. doi:10.1002/joc.4865.

[203] Eric A Wan and Rudolph Van Der Merwe. The unscented kalman filter for nonlinear estimation. In *Proceedings of the IEEE 2000 Adaptive Systems for Signal Processing, Communications, and Control Symposium (Cat. No. 00EX373)*, pages 153–158. Ieee, 2000.

[204] Stefanie L. Whitmire and Skip J. Van Bloem. Quantification of microplastics on National Park beaches: 06/01/2015–05/31/2017. Technical report, NOAA, 2017.

[205] Marius Wiggert, Manan Doshi, Pierre F.J. Lermusiaux, and Claire J. Tomlin. Navigating underactuated agents by hitchhiking forecast flows. In *2022 IEEE 61th Annual Conference on Decision and Control (CDC)*. IEEE, 2022.

[206] J. Xu, P. F. J. Lermusiaux, P. J. Haley Jr., W. G. Leslie, and O. G. Logutov. Spatial and Temporal Variations in Acoustic propagation during the PLUSNet-07 Exercise in Dabob Bay. In *Proceedings of Meetings on Acoustics (POMA)*, volume 4, page 11. Acoustical Society of America 155th Meeting, 2008. doi:10.1121/1.2988093.

[207] Fengchao Yao, Ibrahim Hoteit, Larry J Pratt, Amy S Bower, Armin Köhl, Ganesh Gopalakrishnan, and David Rivas. Seasonal overturning circulation in the Red Sea. 2: Winter circulation. *Journal of Geophysical Research: Oceans*, pages 2263–2289, 2014. ISSN 2169-9291. doi:10.1002/2013JC009331. URL https://dx.doi.org/10.1002/2013JC009331.

[208] Fengchao Yao, Ibrahim Hoteit, Larry J Pratt, Amy S Bower, Ping Zhai, Armin Köhl, and Ganesh Gopalakrishnan. Seasonal overturning circulation in the Red Sea: 1. Model validation and summer circulation. *Journal of Geophysical Research: Oceans*, pages 2238–2262, 2014. ISSN 2169-9291. doi:10.1002/2013JC009004. URL http://dx.doi.org/10.1002/2013JC009004.

[209] Peng Zhan, Aneesh C Subramanian, Fengchao Yao, and Ibrahim Hoteit. Eddies in the Red Sea: A statistical and dynamical study. *Journal of Geophysical Research: Oceans*, 119(6):3909–3925, 2014. ISSN 2169-9291. doi:10.1002/2013JC009563. URL http://dx.doi.org/10.1002/2013JC009563.

[210] Peng Zhan, Aneesh C. Subramanian, Fengchao Yao, Aditya R. Kartadikaria, Daquan Guo, and Ibrahim Hoteit. The eddy kinetic energy budget in the Red Sea. *Journal of Geophysical Research: Oceans*, 121(7):4732–4747, 2016. ISSN 21699291. doi:10.1002/2015JC011589.

[211] Peng Zhan, Ganesh Gopalakrishnan, Aneesh C Subramanian, Daquan Guo, and Ibrahim Hoteit. Sensitivity Studies of the Red Sea Eddies Using Adjoint Method. *Journal of Geophysical Research: Oceans*, 0(ja), 2018. doi:10.1029/2018JC014531. URL https://agupubs.onlinelibrary.wiley.com/doi/abs/10.1029/2018JC014531.

[212] Peng Zhan, George Krokos, Daquan Guo, and Ibrahim Hoteit. Three-Dimensional Signature of the Red Sea Eddies and Eddy-Induced Transport. *Geophysical Research Letters*, 46(4):2167–2177, feb 2019. ISSN 0094-8276. doi:10.1029/2018GL081387. URL https://doi.org/10.1029/2018GL081387.

[213] Tamay M. Özgökmen, Anne Molcard, Toshio M. Chin, Leonid I. Piterbarg,

and Annalisa Griffa. Assimilation of drifter observations in primitive equation models of midlatitude ocean circulation. *Journal of Geophysical Research: Oceans*, 108(C7), 2003. ISSN 2156-2202. doi:10.1029/2002JC001719. URL https://onlinelibrary.wiley.com/doi/abs/10.1029/2002JC001719. _eprint: https://onlinelibrary.wiley.com/doi/pdf/10.1029/2002JC001719.